Investigation of coupled line structures in inset dielectric guides

Boskovic, Dragan

Award date:
1991

Awarding institution:
University of Bath

Investigation of Coupled Line Structures in Inset Dielectric Guides

submitted by Dragan Boškovič
for the degree of PhD
of the University of Bath
1991

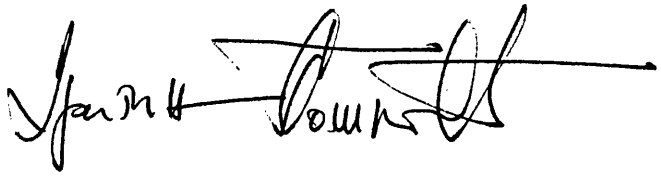

ProQuest LLC
789 East Eisenhower Parkway
P.O. Box 1346
Ann Arbor, MI 48106-1346

To my wife Vesna and our daughters Simonida and Katarina

Summary

The object of this thesis is to analyse coupled Inset Dielectric Guide structure and the application of theory developed to the practical coupler design.
The coupled IDG structure is analysed rigorously for LSE and LSM types of polarization. The problem is formulated through the Transverse Resonance Diffraction approach using integral impedance or admittance operators, accordingly to the polarization used. The operators are discretized in the space domain by the Ritz-Galerkin method employing generalized Laguerre polynomial functions as a basis set capable of dealing with singular boundary conditions. Fast convergence is achieved and the accuracy is demonstrated by comparison with measured results.
The developed method amalgamized with Bethe's theory of waveguide coupling through small holes is then used to synthesize multi-hole IDG coupler. Synthesis is based on an analysis and optimization procedure linked through an error function that measures the agreement between achieved and desired response. Two types of analysis are developed:

- first type considers hole and air coupling as independent coupling mechanisms,
- second type of analysis includes the interaction of mechanisms.

A good agreement between predicated and measured results is achieved. A new method of modeling influence of finite wall thickness on coupler responses is developed and implemented in this work.

Acknowledgements

The author would like to express his gratitude to Dr. S. R. Pennock for his guidance and friendly approach during supervision of this work. Nothingless, the author admirance goes to Prof. T. Rozzi who gave numerous valuable suggestions and whose continuous interest in the matter was source of encouragement for the author.

The many thanks for unforgettable time goes to my office companions Miss Alice Bailey and Dr. Akram Hammoudeh, as well as to fellow Postgraduate students and members of staff for their interest and valuable discussions.

This work was partly funded by a grant from the Science and Engineering Research Council (GR/F66733) and the author is honestly grateful for their support.

Publications

1. T. Rozzi, S. R. Pennock and D. Boscovic
   Dispersion characteristic of coupled inset dielectric guides
   Microwave European Conference, Budapest, September 1990, Paper P1.20

2. S. R. Pennock, D. Boscovic and T. Rozzi
   Analysis of coupled inset dielectric guides under LSE and LSM polarisation
   accepted for publication in IEEE Transaction on Microwave Theory and Techniques

3. S. R. Pennock, D. Boscovic and T. Rozzi
   Broadband Inset Dielectric Guide Coupler
   Microwave European Conference, Stuttgart, September 1991, Paper A8.3

Contents

Chapter 1

Introduction

The communication and information technology has been making giant steps allowing more and more users to benefit from recent developments. However, more users requires more channels, and, in order to avoid spectrum overcrowding, the operating frequency keeps moving up. The requirements for high definition satellite and radar systems and needs for compact system size have been an additional stimulus for the development of high frequency systems due to the small wavelength of such system. Also high speed computation introduce problems of electromagnetic compatibility for printed digital boards and open up needs for transmission media allowing large scale on board integration with low cross-talk level between lines.
MMIC technology opens door for design of integral systems operating in millimetre wave band, which stretches from 30 GHz to 300 GHz. This advanced technology represents major brakethrough and the components such as switches, mixers, oscillators and even amplifiers has become a reality for lower bands of millimetre frequency range. These components are smaller and lighter than their lower frequency counterparts, but tolerance requirements become more tight especially in terms of dimensions and machining finish of metal walls and corners. For these reasons the manufacturing costs of millimetre wave components are high.
The most widely used transmission structure for microwave integrated circuits design has been microstrip and the housing variants such as suspended substrate stripline and finline.

These structures can be fabricated using conventional printed circuit technique which made them very popular. Housing must be smaller or similar in size to the rectangular waveguide at that frequency in order to avoid higher mode excitation. The necessity to fabricate the planar circuits with increasingly high tolerance standards as frequency increases is limited by the etching process and so alternative, and easier to manufacture structures are sought for millimeter wave frequencies.

1.1 Inset Dielectric Guide Structure

The structures that claim to be suitable for applications on millimetre wave range are surface waveguide structure. Such structures support guided waves with a phase velocity less than the characteristic velocity for the particular medium and are thus known as slow wave structure.

Various types of slow wave structure have been proposed for millimetre wave use such as image line, insular line, trapped image line, non-radiative guide, groove guides and etc.. The cross section of the above listed structures consist of two or more regions with different characteristic velocities, so that the effective dielectric constant for each region is different. The interface between the different regions supports a wave that has a phase velocity somewhere between the characteristic velocities of the regions.

The low loss nature of surface waveguides comes from the fact that slow wave propagates in low loss dielectrics and are loosely bounded to the structure. However, a loosely bound wave can detach itself from the guiding structure and radiate into surrounding medium if it comes across even a small discontinuity, or any change in direction of guiding such as bend.

The Inset Dielectric Guide (IDG) shown in Fig.1.1a was mentioned in [1] as a variation of image line that could have a practical use. IDG consists from a metal groove filled with dielectric. It has been shown that this structure possesses several advantages over the image [2], Fig. 1.1b, and insular guide [3], Fig. 1.1c. One major performance advantage that the IDG possesses is its ability to guide energy around relatively sharp bends with low radiation

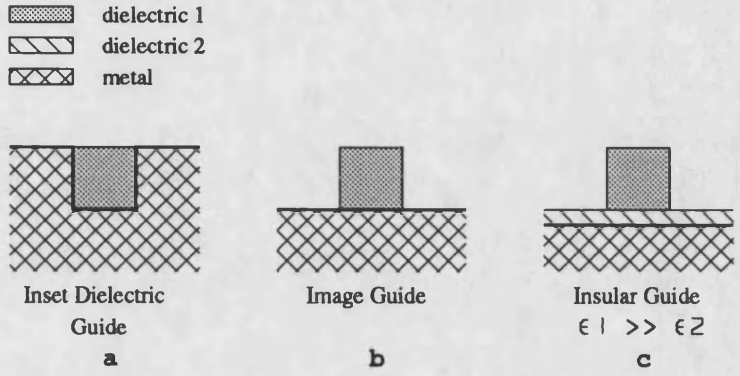

Figure 1.1: Three similar types of slow wave guiding structure

loss [4].

In terms of its manufacture, IDG appears to be quite simple to construct. It is seen as easier to machine a precision slot in a metal ground and then fill that groove with dielectric, than to machine dielectric to same dimensions and bound to metal ground as it should be done in the image guide case. Moreover, through the use of low dielectric loss plastic moulding and spray metalisation techniques, IDG components could be lightweight and cheap to mass production.

The problems encountered in the inclusion of PIN, mixer and source diodes in image or insular guide circuits produces a major limitation in use of such structure for sub-systems or a system design. As it was shown [5] the fundamental HE_{01} mode in deep slot IDG has a constant electric field variation across the slot and a field maximum near the air-dielectric interface. This is a almost ideal situation for diode integration since the device can be placed across the slot to couple strongly with the field without needing to modify the IDG structure. In common with image and insular guide, it has been seen that thin printed dipoles on guide surface produce low reflection radiating elements [6]. These elements are very suitable for constructing arrays which naturally produce little mismatch. Through choice of slot configuration and dipole orientation, both horizontal and vertical polarization antennas may be realized in IDG [7]. The resulting radiating surface has no protruding edges and could be

made either flat or curved by design. The radiation properties of the IDG array antennas have been seen to give very low cross polarization [8].
The three distinct advantages characterize use of the IDG structure rather than image guide:

- simpler manufacture
- resistance to the radiation loss from the bends
- easier inclusion of a diodes for the purpose of control device design.

Coupled line sections can arise in two dimensional arrays where coupling between adjacent sections of the array may be of importance due to the lengths involved. Parallel antenna arrays in IDG have been shown to suffer much less from near field coupling problems than similar arrays in microstrip or image guide, because of the presence of the side metal wall which frustrates lateral TM surface wave propagation.
Parallel coupled line in IDG structure depicted on Fig.1.2 can be constructed almost as easily as single lines, and it was the goal of this thesis to provide a rigorous analysis of coupled lines and to assess its practical application to the design of IDG couplers. Also coupled lines can be employed in various bandpass filter and matching networks design. Consequently, basic filtering and power splitting devices could be fabricated in the same circuit media as the antenna, forming a complete sub-assembly.

1.2 Coupled Dielectric Guide Structures: review

Various researcher have investigate coupling between certain dielectric guides and its application to coupler design [9]-[14]. Most designs presented so far had treated the degenerate mode coupling, i.e. coupling between same modes of dielectric guides with identical cross-section. An approximate analytical method, so called effective dielectric constant (EDC), alongside with empirical data was used to derive coupling coefficients for symmetric and non symmetric coupled slab dielectric guide structures [9]. For the case of non-symmetric coupler it was necessary to make additional measurements in order to determine a correction factor. Authors

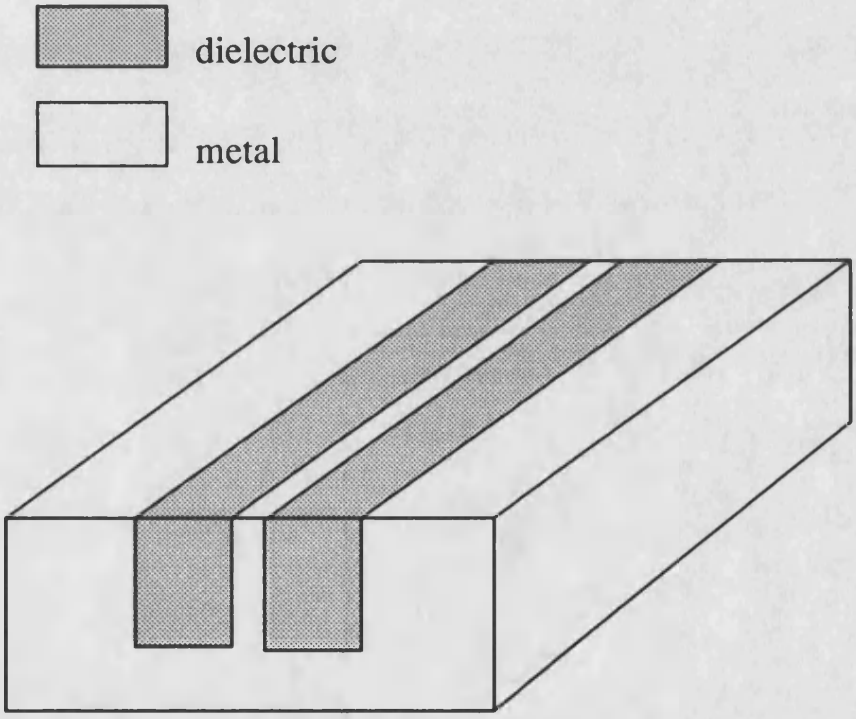

Figure 1.2: Parallel coupled IDG

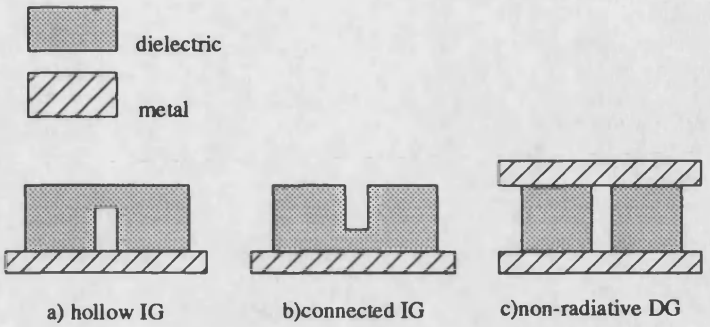

Figure 1.3: Some coupled surface wave guide structures

claim that same method can be applied on guiding structures with rectangular cross-section, or even on coupling between different guiding structures as long as the propagation constants of guides are similar.

In [10], authors analysed hollow image guide structure which also can be considered as two parallel image guides coupled strongly by a dielectric overlay. Again the EDC have been used for dispersion characterization of single and coupled structure. The characteristic of 120mm long coupled section was presented and measured results, corrected for the dielectric and radiation losses, shows satisfactory agreement with predicted results. The coupler has a relatively narrow bandwidth of 10% for 3dB characteristic and coupling decreases with frequency increasing, which is common behavior for all dielectric guide couplers.

The coupling between curved transmission lines has been investigated in [11], and closed-form expressions for the field amplitudes, directivity and reflection are given. An experimental model for a 3dB directional coupler was designed to operate at 94 Ghz using non-radiative dielectric guides. The experimental data were in good agreement with theoretical results though a substantial amount of insertion loss was found, which is largely believed to be dielectric loss. Again measured results were corrected for losses, and shows very narrow-band coupling characteristic.

The design and evaluation of the directly connected image guide directional coupler was

presented in [12]. To analyse dispersion characteristic of directly connected image guides the EDC approach has been used and synthesis is done in terms of even and odd modes. The bandwidth of such coupler with proper dimensions and the optimized value for height of connecting dielectric layer, extends to about 28 percent.

A beam-splitter coupler type was used to design broadband coupler employing thin dielectric film with appropriate dielectric constant for direct connection of two image guide [13]. However, this method can be inconvenient in practice because a layer having a specific dielectric constant which is different from that of the guides is required.

All of the above analyses were performed for degenerate modes, i.e. for symmetric coupled lines with identical phase constants. The asymmetrical coupler design can improve bandwidth and a 3dB coupler with 30 percent bandwidth was realised by taking advantage of the dispersion and the frequency dependence of coupling per unit length between two dielectric guides with asymmetrical cross sections [14]. Asymmetrical couplers are not hybrid by nature and the simple single line compensation of the phase response was used in order to achieve approximate quadrature of signals on coupled and through ports.

Another possible approach to wide-band hybrid design would be the couplers based on tapered velocity principle. However, a serious drawback of the tapered velocity couplers is that they have to be very long, several tens to hundreds of wavelengths, which makes them large and lossy.

1.3 Survey of the Thesis

The material of the thesis tries to follow chronological order in which it was developed. The remainder of the work is divided into six chapters.

Chapter two is used to highlight the theory of coupled lines. The scattering matrix theory gives several useful general theorems on the properties of the four port directional couplers. But scattering matrix can not provide field description inside the four port junctions and this theory appears to be useful in combination with other two theory described in same chapter.

The symmetry of the junction can, however, provide some knowledge about the field in the interior and wave solution of Maxwell's equations under specific boundary conditions becomes simpler. The analysis of symmetric junctions can be split into two trial analysis of the junction under two different sets of boundary conditions. This approach, in terms of even and odd modes is presented in the second section of the second chapter and will be used in this thesis to derive Transverse Resonance Diffraction (TRD) dispersion equation for degenerate modes of the coupled IDGs.

Coupled waveguide theory is presented in the third section, and represents general theory of coupling between two waveguides. This pioneering work is done by Miller [15] and was in later stages extended to include coupling theory of velocity tapered guides [16]-[18]. The mathematical model of the two coupled lines, based on a two first order differential equations, gives physical understanding of power distribution between lines. As it will be shown, this distribution depends on line phase constant, the coupling coefficient and the length of coupled section.

Chapter three is devoted to the evaluation of TRD dispersion equation under LSE and LSM polarization. The complete field description of all three regions is derived from y directed electric and magnetic vector mode functions. As the analysis in terms of even and odd coupled modes is applied, field description for region I should be found for both modes. The impedance and admittance integral operators for LSE and LSM polarization respectively, has been formulated using a variational principle.

Chapter four describes Ritz-Galerkin discretization procedure as applied on TRD dispersion operator equation. The choice of proper basis function, able to take into account singular behavior of field components on metal corners, is presented. The optimal scale factor was introduced through basis function set in order to give the best fit of unknown field on discontinuity planes. The matrix model of TRD dispersion equation gives access to finite network representation of single and coupled IDG lines as well as the possibility of analysing coupled IDG arrays by performing ordinary matrix operations. In the last section of this chapter, expressions for field components are given in terms of discretization coefficients.

Numerical results and their comparison with measured data are presented in Chapter 5. The shallow and deep slot IDG configuration are analysed and dispersion characteristic for various modes of single and coupled IDG lines is given.
Chapter six comprises multihole coupler theory, which is together with results from previous chapter used in broadband IDG coupler design. Two different synthesis procedure has been considered.

- First approach treats discrete hole and continuous wave coupling independently. Overall coupling is obtained by simple addition of these two coupling mechanisms and synthesis of coupler with flat coupling response is done using optimization procedure.

- Second approach is based on the hybrid network representation comprising *Pi* lumped network which models aperture coupling and such circuit is placed between sections of transmission line that has same propagation parameters as IDG. Then, in order to obtain response of overall structure an network analysis in terms of chain matrices is utilized. On this way two coupling mechanisms are considered as interactive and the measured results are in good agreement with analytically predicated data. Again, the synthesis is performed by the help of an optimization procedure.

Finally in chapter seven the results of the preceding chapters are brought together to enable observations and conclusion to be made. The need and scope of further work in IDG technology is also discussed.

References

[1] D. D. King and S. P. Schlesinger

Dielectric Image Guide

IRE Trans. Microwave Theory Tech., vol.MTT-6, July 1958, pp.291-298

[2] D. D. King

Properties of Dielectric Image Lines

IRE Trans. Microwave Theory Tech., vol.MTT-3, March 1955, pp.75-81

[3] R. M. Knox and P. P. Toulios

Integrated Circuits for the Millimetre through Optical Frequency Range

Proc. Sym. Submillimetre Waves, New York 1970

[4] S. Hedges and T.Rozzi

The Loss Analysis of Inset Dielectric Guide Including Bending Loss and a Comparison with Image Line

Paper P4.5 pp.933-938, 17th European Microwave Conference, Rome, Sept 1987

[5] T. Rozzi and S. J. Hedges

Rigorous Analysis and Network Modeling of the Inset Dielectric Guide

IEEE Trans. Microwave Theory Tech., vol.MTT-35, pp.823-834, Sept 1987

[6] T. Rozzi and L. Ma

Mode Completeness, Normalization and Green's Function of the Inset Dielectric Guide

IEEE Trans. Microwave Theory Tech., vol.MTT-36, pp.542-551, March 1988

[7] L. Ma, S. R. Pennock and T. Rozzi

Linear Arrays Realised in IDG

Paper of the IEE colloquium ' Components for Novel Transmission Lines' Digest No. 1990/048, March 1990

[8] T. Rozzi and L. Ma

An Efficient Mode Launcher for Arrays of Longitudinal Dipoles in IDG

MTT-S Digest 1990, Paper MM6 pp1243-1246

[9] T. Trinh and R. Mittra

Coupling Characteristics of Planar Dielectric Waveguides of Rectangular Cross Section

IEEE Trans. Microwave Theory Tech., vol.MTT-29, pp.875-880, Sept 1981

[10] J.-F. Miao and T. Itoh

Hollow Image Guide and Overlayed Image Guide Coupler

IEEE Trans. Microwave Theory Tech., vol.MTT-30, pp.1826-1831, Nov 1982

[11] M. Abouzahra and L. Lewin

Theory and application of coupling between curved transmission lines

IEEE Trans. Microwave Theory Tech., vol.MTT-30, pp.1988-1985, Nov 1982

[12] D. I. Kim, D. Kawabe, K. Araki and Y. Naito

Directly Connected Image Guide 3dB Couplers with Very Flat Couplings

IEEE Trans. Microwave Theory Tech., vol.MTT-32 pp.621-628, June 1984

[13] R. J. Collier and G. Hjipieris

A Broad Band Directional Coupler for Both Dielectric and Image Guides

IEEE Trans. Microwave Theory Tech., vol.MTT-33 pp.161-163, Feb 1985

[14] P. K. Ikalainen and G. L. Matthaei

Design of Broad Band Dielectric Waveguide 3dB Coupler

IEEE Trans. Microwave Theory Tech., vol.MTT-35 pp.621-628 July1987

[15] S. E. Miller

Coupled Wave Theory and Waveguide Application

Bell System Tech. J., vol.-33, pp.661-719, May 1954

[16] J. S. Cook

Tapered velocity couplers

Bell Syst. Tech. J. vol.34 pp.807-822 July 1955

[17] A. G. Fox

Wave Coupling by Warped Normal Modes

Bell Syst. Tech. J. vol.34 pp.823-852 July 1955

[18] W. H. Louisell

Analysis of the Single Tapered Mode Coupler

Bell Syst. Tech. J. vol.34 pp.853-870 July 1955

Chapter 2

Methods of Coupled Lines Analysis

The microwave engineer is often faced with the dilemma of which type of coupler to use in system design in order to meet specification. Sometimes , it is possible to satisfy a specification by the use one of several coupler types, when choice is then made on the ground of other parameters such as cost, manufacturing techniques, the physical layout, weight, etc.. Quite as often, the specification can be met only by one type of coupler, so that knowledge of general coupler theory is desirable and three different approaches for the four port network analysis will be presented in this chapter. The extensive review of different coupler types and basic coupler theory is given by Levy [1] and Altman[2].

2.1 Scattering Matrix of Coupled Four-port

Application of scattering matrix theory can gives us several very useful general theorems on the properties of multi-port junction, and particularly interesting for us, on properties of the four port directional coupler. For the case of linear, passive and reciprocal n-port network, the external behavior of the network can be represented by n linear equations, written in matrix form as:

$$[b] = [S][a] \tag{2.1}$$

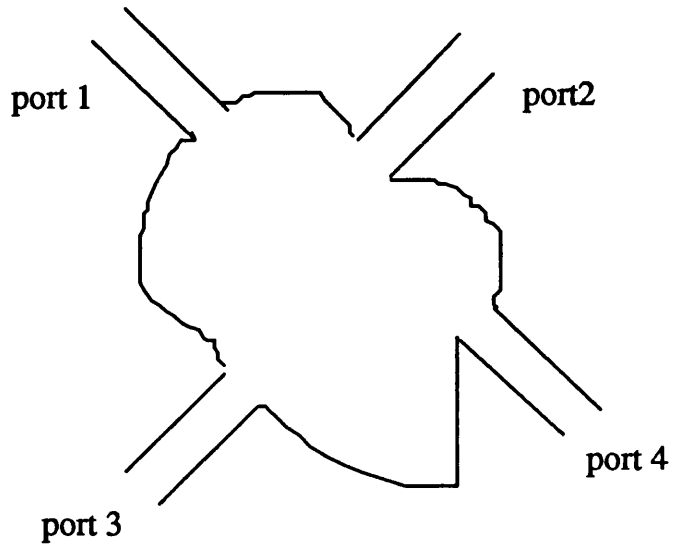

Figure 2.1: Four-port network

The $[b]$ and $[a]$ are a column vectors representing scattered and incident wave amplitudes, respectively. The interpretation of the elements s_{ij} of the $n \times n$ matrix is that if $i \neq j$, s_{ij} represents the transmission coefficient between arms i and j, while s_{ii} represents the reflection coefficient at the port i. The next two properties of S matrix are of prime importance [3].

- For the reciprocal networks the scattering matrix and its transpose are identical

$$s_{ij} = s_{ji} \tag{2.2}$$

- For the lossless networks the scattering matrix satisfy unitary relationship i.e.

$$[S][S]^{\star} = [1] \tag{2.3}$$

where $\star$ indicates complex conjugate transponse values of the matrix $[S]$.

Consider a lossless four port network represented in Fig.2.1 where ports 1&2 and ports 3&4 are mutually isolated ports. Furthermore, if we suppose that one pair of ports is ideally matched

then the unitary relationship suggests that two remaining ports must be ideally matched, too. It also can be easily proved that every four-port junction with perfectly matched ports possesses two sets of mutually isolated ports and therefore, performs as directional coupler [1].

The reference planes in the various ports may be chosen to fix the phases of the scattering waves and set s_{13} to be real and s_{14} purely imaginary. Then the scattering matrix of coupled four-port takes the form

$$|S| = \begin{vmatrix} 0 & 0 & \alpha & \jmath\beta \\ 0 & 0 & \jmath\beta & \alpha \\ \alpha & \jmath\beta & 0 & 0 \\ \jmath\beta & \alpha & 0 & 0 \end{vmatrix} \tag{2.4}$$

One of the most common and useful classes of directional couplers is completely symmetric structure, where ports from Fig.2.1 can not be physically indistinguishable. Again applying the unitary relationship it is possible to work out some useful general properties of the symmetrical coupler, particularly in terms of the phase difference between coupled and through ports. In the case of ideally matched four-port symmetric network with perfect isolation, the phase difference between output ports is 90 degree.

This approach allow us to find the phase deviation in the case when isolation is not perfect and consequently the matching is not ideal. For the $3dB$ symmetric coupler when isolation is better then $30db$, phase differ only for 0.1 degree from 90 degrees, and when isolation is down to $20dB$ then difference raise up to 1.2 degree.

2.2 Analysis in Terms of Even and Odd Modes

The symmetry of network geometry can be used to make analysis of the four-port junction easier and provide the solution of Maxwell's equation for the boundary conditions imposed by electro-magnetic nature of such symmetric junction [4].

Suppose that the directional coupler depicted in Fig.2.2 has a symmetry plane as indicated

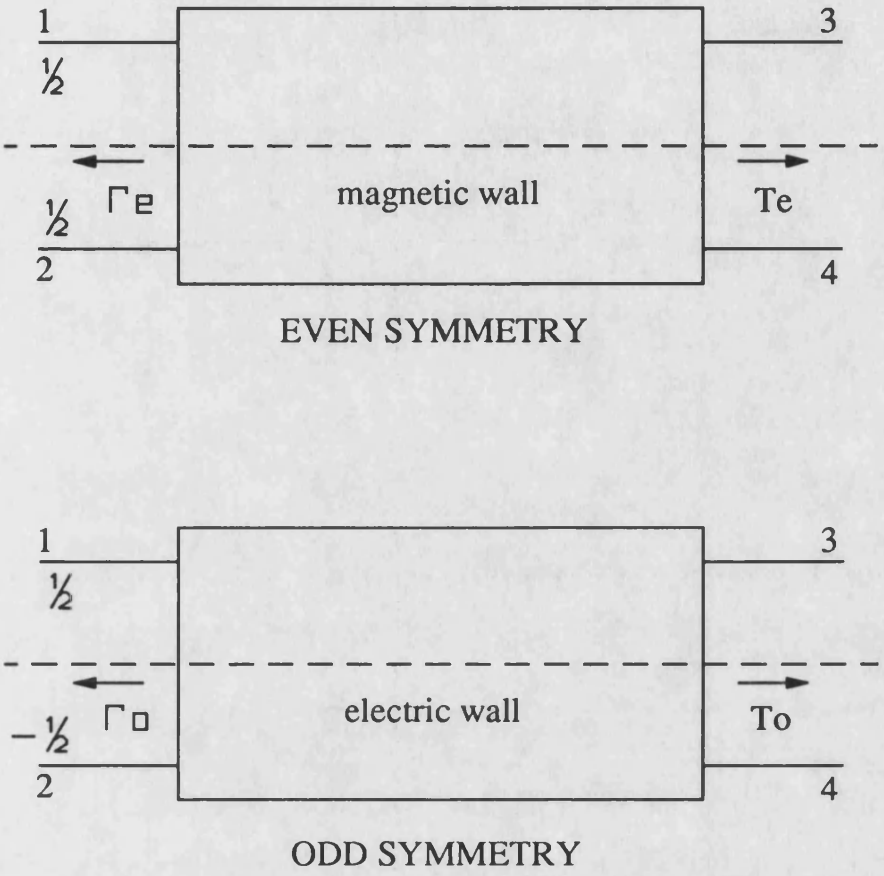

Figure 2.2: Four-port network with (a) even mode excitation and (b) odd mode excitation

by the dotted line. When two in phase signals of half amplitude are applied to ports 1 and 2, by symmetry a voltage maximum occurs at the line of symmetry, what is equivalent to having infinite impedance on the symmetry plane. It means that the junction may be left open and that will not affect the field distribution which is equivalent to raising *magnetic wall* as the symmetry plane. This mode of operation is called **even** mode.

Similarly, an **odd** mode is defined as the mode existing when ports 1 and 2 are excited by two signals with half amplitude but out of phase. Then a short circuit representation of symmetry plane become reality or expressed in field term, *electric wall* placed as symmetry plane would not affect field distribution.

The odd and even modes are **normal** operational modes of symmetric junction and exhibit odd or even symmetry about the electric and magnetic wall raised as symmetry plane. Conducting analysis in this way, the problem of the four-port network analysis reduces to that of a two-port network, for which a solution may be obtained more easily.
The response corresponding to unitary source applied at port 1 is obtained by super-position of even and odd modes, that gives expressions for the signals on the guides:

- For guide one

$$\begin{aligned} E_1 &= \frac{1}{2}\cos(\omega t - \beta_e x) + \frac{1}{2}\cos(\omega t - \beta_o x) \\ &= \cos(\omega t - \beta x)\cos(cx) \end{aligned} \tag{2.5}$$

- For guide two

$$\begin{aligned} E_2 &= \frac{1}{2}\cos(\omega t - \beta_e x) - \frac{1}{2}\cos(\omega t - \beta_o x) \\ &= \sin(\omega t - \beta x)\sin(cx) \end{aligned} \tag{2.6}$$

where

$$\begin{aligned} \beta &= \frac{\beta_e + \beta_o}{2} \\ c &= \frac{\beta_e - \beta_o}{2} \end{aligned}$$

Same expression can be written in phaser notation as

$$\begin{aligned} E_1(x) &= \cos(cx)exp(-\jmath\beta x) \\ E_2(x) &= \jmath\sin(cx)exp(-\jmath\beta x) \end{aligned} \tag{2.7}$$

which will be used later on for the comparison with expressions obtained from the coupled mode theory.

For the case of symmetric junction analysed in terms of even and odd modes, the vector amplitudes of scattered waves emerging out of ports are found as:

$$\begin{aligned} b_1 &= \frac{1}{2}(\Gamma_e + \Gamma_o) \\ b_2 &= \frac{1}{2}(\Gamma_e - \Gamma_o) \\ b_3 &= \frac{1}{2}(T_e - T_o) \\ b_4 &= \frac{1}{2}(T_e + T_o) \end{aligned} \tag{2.8}$$

where Γ_e and Γ_o are reflection coefficients and T_e and T_o are transmission coefficients of two-ports obtained for even and odd mode, respectively. As analysis of two-port network is usually carried out in terms of impedance or chain transfer matrix, the relationship between reflection and transmission coefficients on one side and chain matrix on other side is stated as:

$$\begin{aligned} \Gamma &= \frac{A + B/Z_0 - CZ_0 - D}{A + B/Z_0 + CZ_0 + D} \\ T &= \frac{2}{A + B/Z_0 + CZ_0 + D} \end{aligned} \tag{2.9}$$

Z_0 is the characteristic impedance of the input and output ports, while the input impedance for matched load on output port is given as

$$Z_l = \frac{A + B/Z_0}{C + D/Z_0} \tag{2.10}$$

An approach for analysis of symmetric coupled lines in terms of chain matrix elements is presented in Appendix A. Very interesting conclusions, determining whether the coupler belongs to the families of forward or backward couplers, can be drawn from such analysis. An ideal forward coupler needs even and odd mode impedances to be equal, while phase constants of even and odd mode must not differ for an ideal backward coupler:

- Forward coupler $\qquad Z_e = Z_o \qquad \beta_e \neq \beta_o$
- Backward coupler $\qquad Z_e \neq Z_o \qquad \beta_e = \beta_o$

2.3 Theory of Coupled Waves

Here, we summarize the theory developed by Miller [5] and generalizations and extensions of this work were carried out by other authors [6, 7, 8]. Consider two coupled guides I and II represented in Fig.2.3. The variations of the wave amplitude in guide I and guide II can be represented by first order linear differential equations relating the wave amplitudes in the two guides within the coupling region. This theory takes into account not only unilateral coupling from one to another line, but also back coupling. The theory of coupled modes must be invoked whenever coupling is substantial and non-localized.

$$\begin{aligned} \frac{\partial E_1}{\partial x} &= -(\gamma_1 + k)\, E_1 + k E_2 \\ \frac{\partial E_2}{\partial x} &= k E_1 - (\gamma_2 + k)\, E_2 \end{aligned} \tag{2.11}$$

where E_1 and E_2 are the complex wave amplitudes on guides I and II, γ_1 and γ_2 are the propagation constants of lines I and II and k is the coupling coefficient within the region of coupling.

For the wave of unit amplitude incident at guide I, i.e. for the starting conditions $E = 1$ and $E_2 = 0$ at $x = 0$, system of differential equations (2.11) gets the solution in form

$$\begin{aligned} E_1 &= \left[\frac{1}{2} - \frac{\gamma_1 - \gamma_2}{2\sqrt{(\gamma_1 - \gamma_2)^2 + 4k^2}}\right] e^{r_1 x} + \left[\frac{1}{2} + \frac{\gamma_1 - \gamma_2}{2\sqrt{(\gamma_1 - \gamma_2)^2 + 4k^2}}\right] e^{r_2 x} \\ E_2 &= \frac{k}{\sqrt{(\gamma_1 - \gamma_2)^2 + 4k^2}} e^{r_1 x} - \frac{k}{\sqrt{(\gamma_1 - \gamma_2)^2 + 4k^2}} e^{r_2 x} \end{aligned} \tag{2.12}$$

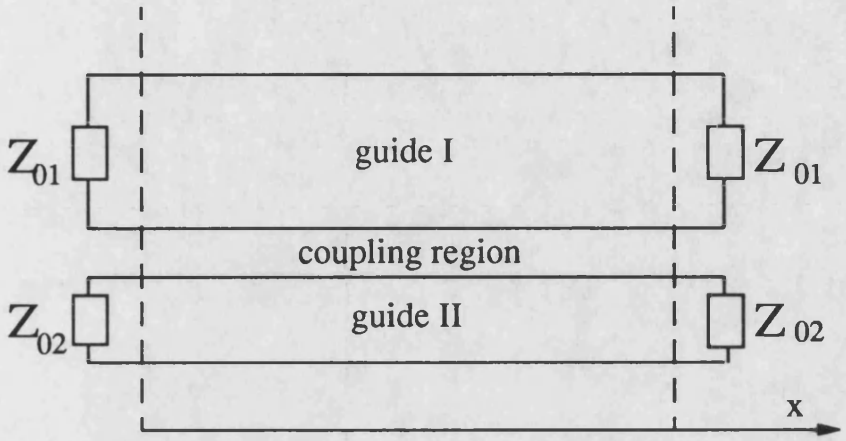

Figure 2.3: Coupled transmission lines

with

$$r_1 = -\frac{1}{2}(2k + \gamma_1 + \gamma_2) + \sqrt{(\gamma_1 - \gamma_2)^2 + 4k^2}$$
$$r_2 = -\frac{1}{2}(2k + \gamma_1 + \gamma_2) - \sqrt{(\gamma_1 - \gamma_2)^2 + 4k^2}$$

For the lossless coupling mechanism, i.e. when k is purely imaginary $k = jc$ and for coupling between identical transmission lines, $\gamma_1 = \gamma_2 = \gamma$, previous equations simplify into forms identical to that one obtained by analysis in terms of even and odd modes.

$$E_1 = \cos cx e^{-(jc+\gamma)x} \qquad (2.13)$$
$$E_2 = j \sin cx e^{-(jc+\gamma)x}$$

The amplitude and phase variations due to the coupling as given by the above equations are shown in Fig.2.4. Complete power transfer occurs cyclically with a period of $cx = \pi/2$, and an arbitrary power distribution between lines can be achieved by suitable choice of coupler length.

Here, we also will give presentation of coupling between two lines with different phase

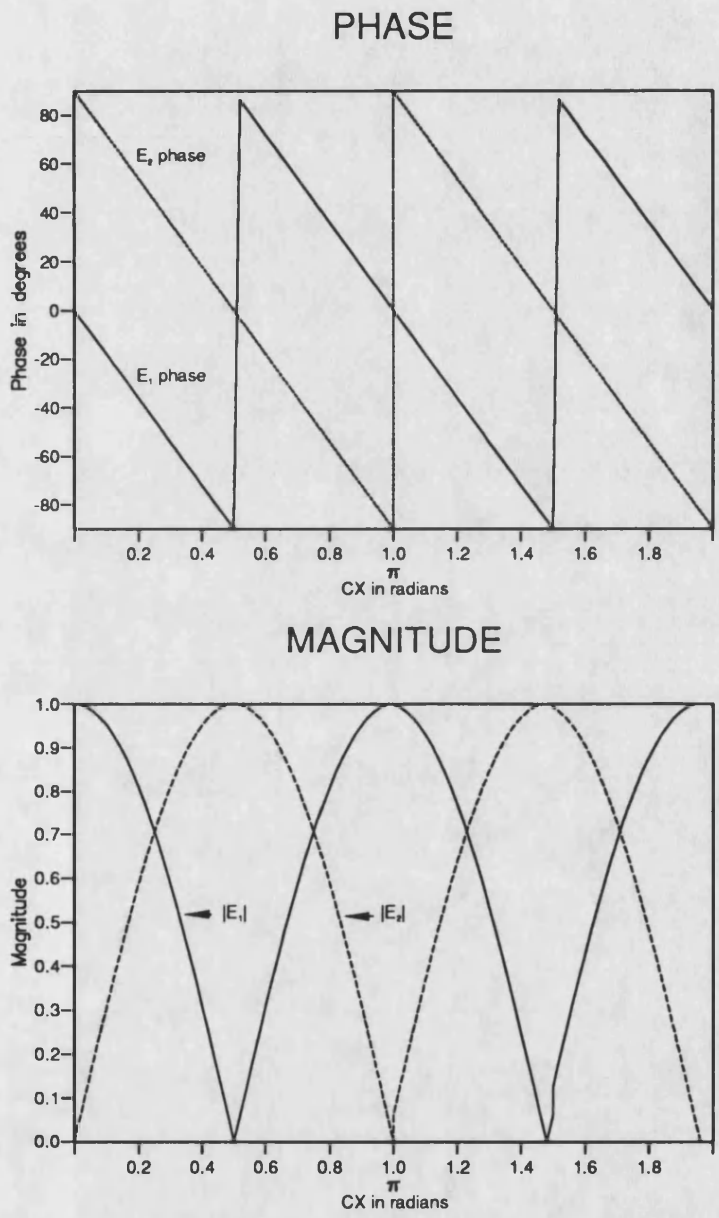

Figure 2.4: Wave amplitude and phase of coupled transmission lines having identical propagation constants

constant, but with same attenuation constant.

$$\alpha_1 = \alpha_2 = \alpha \qquad \gamma_1 = \alpha + j\beta_1 \qquad \gamma_2 = \alpha + j\beta_2 \tag{2.14}$$

when equation (2.12) reduces to

$$\begin{aligned} E_1 = \mathcal{E}_1 e^{-\gamma x} &= (\cos\Phi - jA\sin\Phi)e^{-\gamma x} \\ E_2 = \mathcal{E}_2 e^{-\gamma x} &= jB\sin\Phi e^{-\gamma x} \end{aligned} \tag{2.15}$$

with

$$\begin{aligned} \Phi &= \sqrt{\frac{(\beta_1 - \beta_2)^2}{4c^2} + 1}cx \\ \gamma &= \alpha + j\frac{c + \beta_1 + \beta_2}{2} \end{aligned} \tag{2.16}$$

and

$$\begin{aligned} A &= \frac{\beta_1 - \beta_2}{2c\sqrt{\frac{(\beta_1-\beta_2)^2}{4c^2} + 1}} \\ B &= \frac{1}{\sqrt{\frac{(\beta_1-\beta_2)^2}{4c^2} + 1}} \end{aligned} \tag{2.17}$$

$\mathcal{E}_1$ and $\mathcal{E}_2$ are plotted for the four different values of $(\beta_1 - \beta_2)$, Fig.2.5. It is apparent for bigger differences in phase constant, the maximum coupled power decreases and the period of cyclic variation in coupling is reduced. This can be very useful for application in the broad-band coupler design by deliberately creating difference between the phase constants of the two lines, when there is a region where the coupling is very slightly dependent on cx. The main disadvantage associated with this method of broad-banding is that the directional coupler is not symmetric, so that the phase relationship between the waves are not 90 degree for all frequencies, but varies considerably across the frequency range.

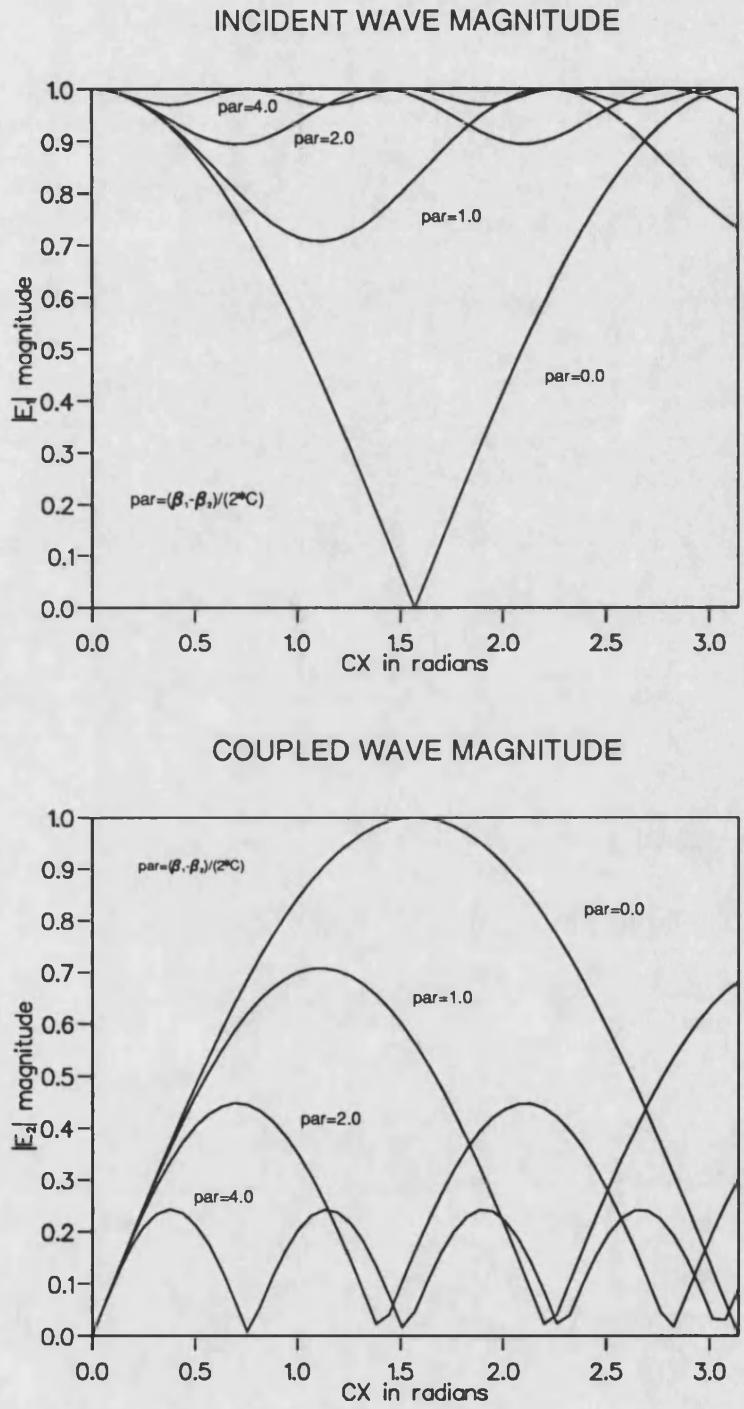

Figure 2.5: Amplitudes of incident and coupled waves on the coupled lines with non-identical phase constants

2.4 Conclusion

The three different approaches to the coupled lines analysis have been presented. The unitary property of the scattering matrix and knowledge about coupler geometry can give us a good deal of information on the general properties of the coupled structure. This theory allows us to predict isolation property and phase deviation for the real coupler case, where matchings of the ports are not ideal and consequently zero return loss could not be assumed.
All symmetrical couplers can be analysed in terms of normal modes, i.e. even and odd modes, when analysis of a four port network is reduced to the two-port network analysis.
The theory of coupled guide developed by Miller, comprises mathematical model based on the system of two first-order differential equations. This theory also gives us understanding how much power is transferred from guide to guide and what is the phase difference between coupled and through port waves for the different geometries of coupled lines. For the case of symmetric coupling structure this theory leads us to the same conclusions obtained by the theory of normal modes.

References

[1] R. Levy

Directional Couplers

Advances in Microwaves, Vol.1, 1966, pp.135-166

[2] J.L. Altman

Microwave Circuits

D. Van Nostrand Company, Princeton, 1964, ch.4

[3] C.G. Montgomery, R.H. Dicke and E.M. Purcell

Principles of Microwave Circuits

MIT Radiation Laboratory Series, Vol.8, McGraw Hill Book Co., New York, 1948,pp.301-303

[4] J. Reed and G.J. Wheeler

A Method of Analysis of Symmetrical Four-Port Networks

IRE Trans. Vol. MTT-4, pp.246-252, October 1956

[5] S.E. Miller

Coupled Wave Theory and Waveguide Applications

Bell System Tech. J., Vol.33, 1954, pp.661-719

[6] J.S. Cook

Tapered Velocity Couplers

Bell System Tech. J., Vol.34, 1955, pp.807-822

[7] A.G. Fox

Wave Coupling by Warped Normal Modes

Bell System Tech. J., Vol.34, 1955, pp.823-852

[8] W.H. Louisell

Analysis of Single Tapered Mode Coupler

Bell System Tech. J., Vol.34, 1955, pp.853-870

Chapter 3

Transverse Resonance Formulation for IDG Coupled Lines

The theory of normal modes is applied to the coupled symmetric IDG lines enabling us to find parameters of interest for a considered IDG structure. The cross section of coupled symmetric IDGs is shown in Fig.3.1, the entire volume is separated into two identical parts by plane of symmetry. Each half can also be divided into three regions by placing two planes along the metal corners of IDG. Due to their nature, these planes will be called discontinuity planes in the following text. For each of the three established regions solution of Maxwell's equation under certain boundary conditions can be evaluated analytically.

Maxwell theory provides general relationships between electric and magnetic field inside macroscopic media. A physical solutions of Maxwell's equations must satisfy the boundary conditions imposed by the media over which the solution is sought. The direct analytical solution of these equation is limited to a few simple cases, and generally speaking some numerical approach has to be adopted in order to get approximate solutions for electric and magnetic fields satisfying boundary conditions determined by the physical nature of a media. Two different numerical approaches for this purpose can be distinguished:

- the first is a pure numerical one, where no prior knowledge of the field is necessarily and a numerical iteration process is used in order to obtain solutions. This approach is very general and consequently has very wide application but in most cases is inefficient giving slow convergence and consuming lot a computing time.

- second approach is combined analytical-numerical, where an analytical solution is sought over the parts of the entire volume and combined with a numerical approach applied to the rest of the volume. With this approach computation time can be considerably reduced.

The later approach has been used in this thesis. The transverse resonance technique used here, employs a transmission line model of the transverse cross section, shown in Fig.3.1, and transforms field theory into circuit and transmission line theory. This method belongs to a space domain approach, where the integral operators are obtained in the terms of a equivalent transmission lines parameters characterizing the IDG cross-section geometry.

3.1 TRD Formulation as Applied on Coupled IDGs

The entire cross section is separated into three different regions and the metal edges will be treated as discontinuity separating the different homogeneous regions. In each of the three regions the propagation constants are linked by the relationship

$$\epsilon_r k_0^2 = k_x^2 + k_y^2 + \beta^2 \tag{3.1}$$

where β is the z directed propagation constant common for each region that has to be determined. The expressions for field components for each of the three regions created by two boundary planes, as shown on Fig.3.1, will be evaluated analytically under y directed LSE and LSM polarizations.

The first region is considered as a quarter open space, the second as a grounded slab dielectric guide and the third one as a half open space. Two discontinuity planes exist and on each

of them continuous modes are excited. Moreover, multiple reflection occurs between two discontinuity planes and thus region II can not be represented by a few discrete transmission lines, as it is done in [1], in any rigorous network representation used by TRD approach. Indeed this region will be represented by two port T or II networks consisting of impedance or admittance integral operators defined for the LSE and LSM polarizations respectively.
In fact, in order to analyze such a region, electric and magnetic walls are placed at $x = d/2$ and $x = a + d/2$, in a manner analogous to the determination of the impedance or admittance parameters of a 2N-port network by open and short circuit ports. Integral operators are then found relating the total E and H field at the various ports under these open and short circuit condition, and these are used to relate the total fields at each port to one another. Such an analysis follows closely the method described in [2].
From such an analysis, the transverse electric and magnetic fields on the first step can be expressed as functions of the transverse electric and magnetic fields on the second step and vice-versa. Choosing a y directed field component as an independent variable the above dependence can be expressed by means of a two-port Green's open-circuit impedance operator for the case of LSE polarization, or an admittance operator for the case of LSM polarization. Such two port circuit representation of region II is terminated with impedance or admittance operators representing the driving point impedances of region I and III, thus completing the circuit representation of the entire structure.

3.2 TRD Formulation under LSE polarization

In the case of deep slot IDG, it has been seen that for HE_{mn} modes the E_y component is small except for the immediate vicinity of the metal corners [3]. This then suggests that rather than using a full six-field component description, the problem can be approximated to good effect by using the five field $LSE^{(y)}$ description. In this case, the H_y field is used as the unknown variable in operator formulation, and corresponding a circuit representation is given in Fig.3.2. referring to the directions notified at the circuit schematic, the operator

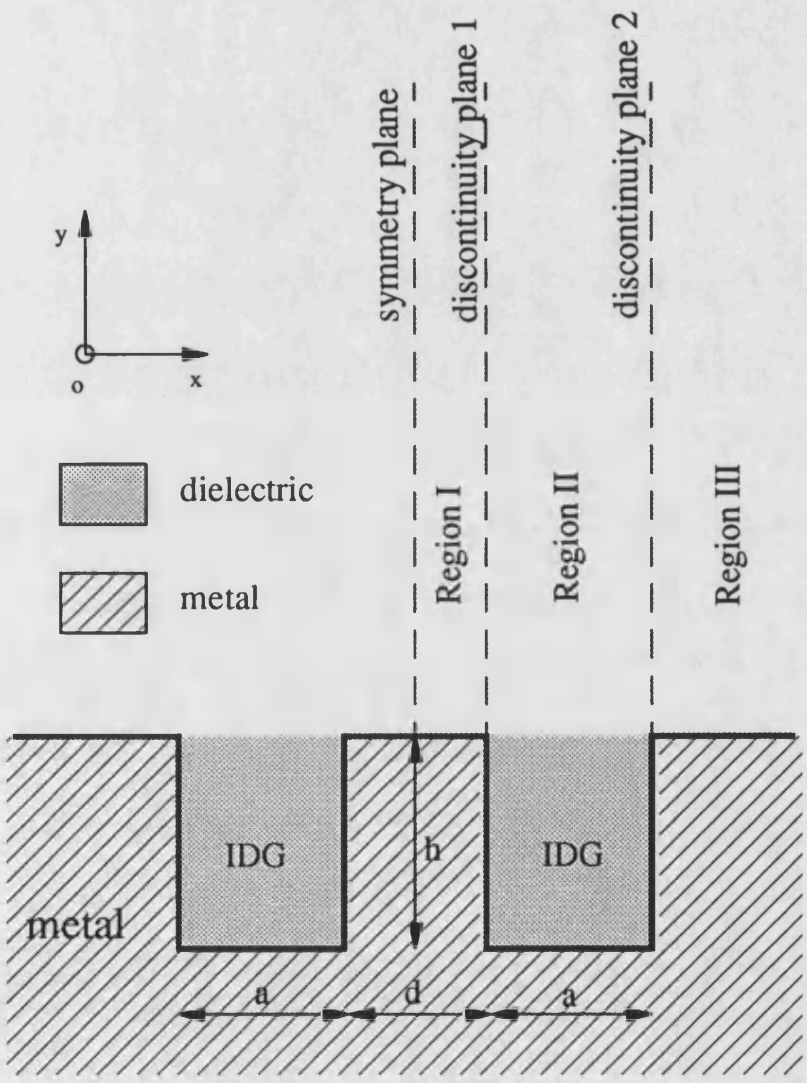

Figure 3.1: Cross section of symmetric coupled IDGs

equations that link E_z and H_y at the two interface planes x+d/2 and x=a+d/2 can be written in matrix form

- For region I & III

$$\begin{vmatrix} -E_1 \\ -E_2 \end{vmatrix} = \begin{vmatrix} -\mathcal{Z}_{1e,o} & 0 \\ 0 & \mathcal{Z}_3 \end{vmatrix} \cdot \begin{vmatrix} H_1 \\ H_2 \end{vmatrix} \tag{3.2}$$

- and for region II

$$\begin{vmatrix} E_1 \\ E_2 \end{vmatrix} = \begin{vmatrix} \mathcal{Z}_{11} & \mathcal{Z}_{12} \\ \mathcal{Z}_{12} & \mathcal{Z}_{11} \end{vmatrix} \cdot \begin{vmatrix} H_1 \\ H_2 \end{vmatrix} \tag{3.3}$$

where the dot product should be understood in the sense of operator multiplication defined as

$$\begin{aligned} E_z(y) &= \int_0^\infty \mathcal{Z}(y,y')\, H_y(y')\, dy' \\ E_z &= \mathcal{Z} \cdot H_y \end{aligned} \tag{3.4}$$

Boundary conditions regarding transverse electric and magnetic fields at the discontinuity planes [5] are found as:

$$\begin{aligned} E_{11} &= E_1 \qquad y \geq 0 \\ E_{22} &= E_3 \qquad y \geq 0 \\ H_{11} &= H_1 \qquad y \geq 0 \\ H_{22} &= H_3 \qquad y \geq 0 \end{aligned} \tag{3.5}$$

Implementation of these conditions into (3.2) and (3.3) and simple addition of those two equations gives matrix form of TRD operators dispersion equation under LSE polarization.

$$\begin{vmatrix} 0 \\ 0 \end{vmatrix} = \begin{vmatrix} \mathcal{Z}_{11} - \mathcal{Z}_{1e,o} & \mathcal{Z}_{12} \\ \mathcal{Z}_{12} & \mathcal{Z}_{11} + \mathcal{Z}_3 \end{vmatrix} \cdot \begin{vmatrix} H_1 \\ H_2 \end{vmatrix} \tag{3.6}$$

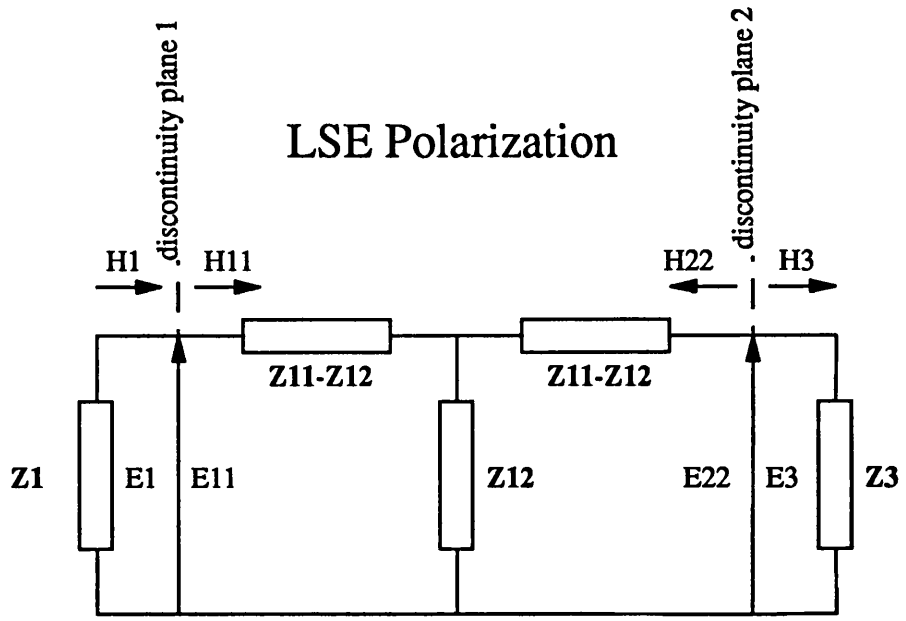

Figure 3.2: Network representation of TRD operator equation under LSE polarization

This operator equation must be solved in order to get solutions for a phase constant of even and odd modes, normal modes of the symmetric coupled IDG structure.

3.3 TRD Formulation for LSM Polarization

LSM polarization is applicable on shallow IDG guide or rather to those modes of the shallow guide where the y directed electric field is a non-negligible field component. The use of E_y as the independent variable determines a formulation of admittance integral operators linking that electric field and H_z, this being another transverse component at the discontinuity planes. The equivalent circuit representation for the LSM polarization is shown in Fig.3.3. The integral operator under LSM polarization is defined as

$$\begin{aligned} H_y(y) &= \int_0^\infty \mathcal{Y}(y,y')\, E_z(y')\, dy' \\ H_y &= \mathcal{Y} \cdot E_z \end{aligned} \tag{3.7}$$

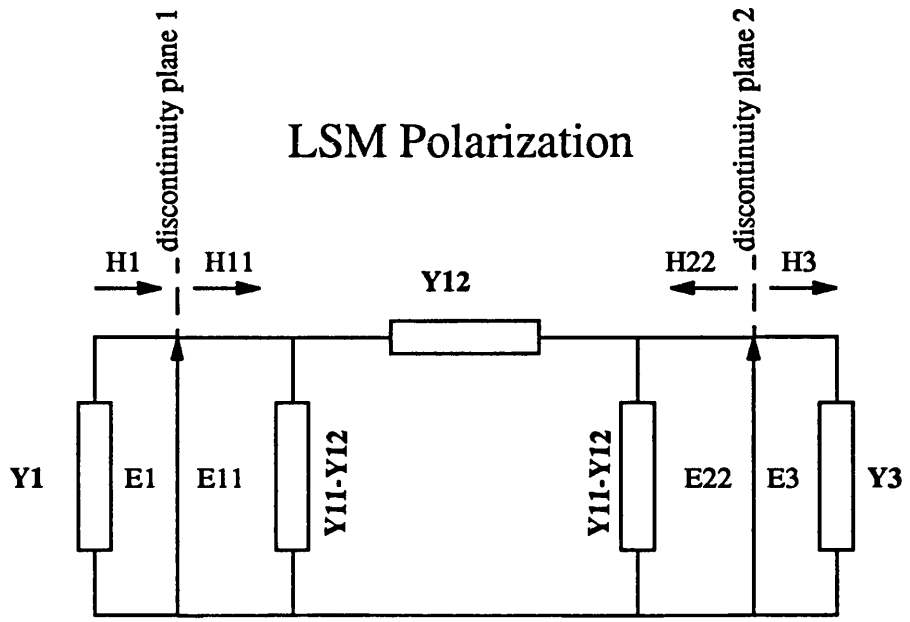

Figure 3.3: Network representation of TRD operator equation under LSM polarization

The operator equations represented in matrix form, accordingly to the directions from Fig.3.3 can be written as

- Regions I & III

$$\begin{vmatrix} -H_1 \\ -H_2 \end{vmatrix} = \begin{vmatrix} -\mathcal{Y}_{1e,o} & 0 \\ 0 & \mathcal{Y}_3 \end{vmatrix} \cdot \begin{vmatrix} E_1 \\ E_2 \end{vmatrix} \tag{3.8}$$

- Region II

$$\begin{vmatrix} H_1 \\ H_2 \end{vmatrix} = \begin{vmatrix} \mathcal{Y}_{11} & \mathcal{Y}_{12} \\ \mathcal{Y}_{12} & \mathcal{Y}_{11} \end{vmatrix} \cdot \begin{vmatrix} E_1 \\ E_2 \end{vmatrix} \tag{3.9}$$

With implementation of same boundary conditions as in LSE case (3.5), TRD dispersion equation for symmetric coupled IDGs under LSM polarization appears as

$$\begin{vmatrix} 0 \\ 0 \end{vmatrix} = \begin{vmatrix} \mathcal{Y}_{11} - \mathcal{Y}_{1e,o} & \mathcal{Y}_{12} \\ \mathcal{Y}_{12} & \mathcal{Y}_{11} + \mathcal{Y}_3 \end{vmatrix} \cdot \begin{vmatrix} E_1 \\ E_2 \end{vmatrix} \tag{3.10}$$

The solutions of this matrix operator equation will give the even and odd mode phase constants that allow calculation of coupling coefficient between two IDGs.

The replacement of $\mathcal{Z}_{1e,o}$ and $\mathcal{Y}_{1e,o}$ with $\mathcal{Z}_3$ and $\mathcal{Y}_3$ in (3.6) and (3.10) respectively, leads to TRD formulation of dispersion equation for single IDG under LSE and LSM types of polarization.

3.4 Field Components

The aim of this section is to determine a electromagnetic field components description for each of the three regions from Fig.3.1.

The functions that can correctly model the electric and magnetic field volume distribution are limited to those solutions of Maxwell's equations which satisfy the relevant boundary conditions. As direct solutions of Maxwell's equations for coupled IDG structure with associated boundary conditions is extremely difficult, the entire volume is separated into three homogeneous regions which are related to each other through the previously established TRD dispersion equation. For each homogeneous region direct solutions of Maxwell's equation is possible and expressions for five field description will be determined.

As all three regions are assumed to be linear, superposition of solutions under different polarization, represent solution of Maxwell's equation itself for the hybrid field description.

The IDG structure has two 90^o metal edges which introduce a singularity to the x and y directed field components. This discontinuity translated in terms of boundary conditions means that such fields go to infinity at the edge. However, the order of singularity must be such to gives finite energy stored in the vicinity of the edge. In [6] it was shown that for a

90^o metal edge the minimum allowable singularity to satisfy this conditions is $r^{-\frac{1}{3}}$, where r stands for the radial distance from the edge.

The field in each region will have a different form, although for a guided mode the phase constant β will be the same for all regions, and the continuity of the transverse fields will apply at the boundary between the two regions. Bearing in mind that the field variation in the z direction is common for all three regions, the coupled IDG structure will be described in terms of field components derived from y directed potential functions.

The method using vector mode functions for purpose of the field evaluation was adopted here [7]. The notification used is

- e'_v and h'_v are the electric and magnetic mode functions for LSM polarization, respectively.
- e''_v and h''_v are vector mode functions for LSE polarization.

The scalar mode functions Φ_v and Ψ_v determine the vector mode functions. Here, the relationship between vector and scalar mode functions is redefined comparing to that given by [8] in order to introduce y directed LSE and LSM polarization.

- LSM polarization:

$$\begin{aligned} e'_\nu(x,z) &= -\frac{1}{k_{t\nu}}\nabla_t \Phi_\nu(x,z) \\ h'_\nu(x,z) &= \vec{y}_0 \times e'_\nu \end{aligned} \tag{3.11}$$

- LSE polarization:

$$\begin{aligned} e''_\nu(x,z) &= \vec{y}_0 \times \frac{1}{k'_{t\nu}}\nabla_t \Psi_\nu(x,z) \\ h''_\nu(x,z) &= \vec{y}_0 \times e''_\nu \end{aligned} \tag{3.12}$$

where $k'_{t\nu}$ and $k''_{t\nu}$ denote the transverse wave numbers and the nabla operator is defined as:

$$\nabla_t = \frac{\partial}{\partial x}\vec{x}_0 + \frac{\partial}{\partial z}\vec{z}_0$$

The scalar mode functions Φ_ν and Ψ_ν are normalized, i.e.

$$\begin{aligned} \int_\Sigma \Phi_\nu \overline{\Phi}_\mu \, \partial S &= \delta_{\nu\mu} \\ \int_\Sigma \Psi_\nu \overline{\Psi}_\mu \, \partial S &= \delta_{\nu\mu} \end{aligned} \tag{3.13}$$

and the vector mode functions satisfy the following orthogonality relationships:

- The electric vector mode functions

$$\begin{aligned} \int_\Sigma e'_\nu \overline{e'}_\mu \, \partial S &= \delta_{\nu\mu} \\ \int_\Sigma e''_\nu \overline{e''}_\mu \, \partial S &= \delta_{\nu\mu} \\ \int_\Sigma e'_\nu \overline{e''}_\mu \, \partial S &= 0 \end{aligned} \tag{3.14}$$

- The magnetic vector mode functions

$$\begin{aligned} \int_\Sigma h'_\nu \overline{h'}_\mu \partial \, S &= \delta_{\nu\mu} \\ \int_\Sigma h''_\nu \overline{h''}_\mu \partial \, S &= \delta_{\nu\mu} \\ \int_\Sigma h'_\nu \overline{h''}_\mu \partial \, S &= 0 \end{aligned} \tag{3.15}$$

The total transverse fields E_t and H_t expressed through transmission line notation, which is adopted here, gives the form [13]

$$
\begin{aligned}
E_t &= \sum_{\nu} V'_{\nu}(y,\omega)\, e'_{\nu} + V''_{\nu}(y,\omega)\, e''_{\nu} \\
H_t &= \sum_{\nu} I'_{\nu}(y,\omega)\, h'_{\nu} + I''_{\nu}(y,\omega)\, h''_{\nu}
\end{aligned}
\tag{3.16}
$$

and conversely, voltage and current amplitudes can be expressed in terms of the vectors H_t and E_t and the vector mode functions e_ν and h_ν.

- Voltage amplitude

$$
\begin{aligned}
V'_{\nu} &= \int_{\Sigma} E_t(x,y,z)\, \overline{e'}_t(x,z)\, \partial S \\
V''_{\nu} &= \int_{\Sigma} E_t(x,y,z)\, \overline{e''}_t(x,z)\, \partial S
\end{aligned}
\tag{3.17}
$$

- Current amplitude

$$
\begin{aligned}
I'_{\nu} &= \int_{\Sigma} H_t(x,y,z) \overline{h'}_t(x,z)\, \partial S \\
I''_{\nu} &= \int_{\Sigma} H_t(x,y,z) \overline{h''}_t(x,z)\, \partial S
\end{aligned}
\tag{3.18}
$$

Then, by separating modes the expressions for the field components are established as:

- LSM polarization:

$$
\begin{aligned}
E'_t(x,y,z,\omega) &= \sum_{\nu} V'_{\nu}(y,\omega)\, e'_{\nu}(x,z) \\
-\jmath\omega\epsilon E'_y(x,y,z,\omega) &= \sum_{\nu} I'_{\nu}(y,\omega)\, \nabla_t \cdot e'_{\nu}(x,z) \\
H'_t(x,y,z,\omega) \times \vec{y}_0 &= \sum_{\nu} I'_{\nu}(y,\omega)\, e'_{\nu}(x,z) \\
H'_y(x,y,z,\omega) &= 0
\end{aligned}
\tag{3.19}
$$

- LSE polarization:

$$
\begin{aligned}
E_t''(x,y,z,\omega) &= \sum_\nu V_\nu''(y,\omega)\, e_\nu''(x,z) \\
E_y''(x,y,z,\omega) &= 0 \\
H_t''(x,y,z,\omega)\times \vec{y}_0 &= \sum_\nu I_\nu''(y,\omega)\, e_\nu''(x,z) \\
-j\omega\mu H_y''(x,y,z,\omega) &= \sum_\nu I_\nu''(y,\omega)\, \nabla_t\cdot \vec{y}_0 \times e_\nu''(x,z)
\end{aligned}
\tag{3.20}
$$

Having the tools necessary for the derivation of the field components, now we proceed with the field evaluation for each region separately under LSE polarization. At the same time, the impedance operator equations will be established using a variational principle. The field expressions and admittance operator equation for LSM polarization are given in Appendix B. Previous equations are valid for discrete eigen-modes. Each of the three regions support continuous modes and for these modes the summation should be replaced by integration over the y directed wave number for the semi-infinite region.

$$
\sum_\nu V_\nu \ldots \Rightarrow \int_0^\infty d\rho V_\rho \ldots \tag{3.21}
$$

3.4.1 Region I: a quarter open space

Boundary conditions valid for region I, which is represented in Fig.3.4, differ for two considered types of normal modes. Hence, two different scalar mode functions had to be introduced, each relating to the appropriate odd or even symmetry of normal modes.

Even mode

When an even mode magnetic wall is placed at the $x = 0$ symmetry plane, boundary conditions corresponding to this case are given as:

- $H_y = 0$ $\qquad x = 0;\ 0 \le y < \infty \quad \& \quad 0 \le x \le d/2;\ y = 0$
- $H_z = \partial E_z/\partial x = 0$ $\qquad x = 0;\ 0 \le y < \infty$

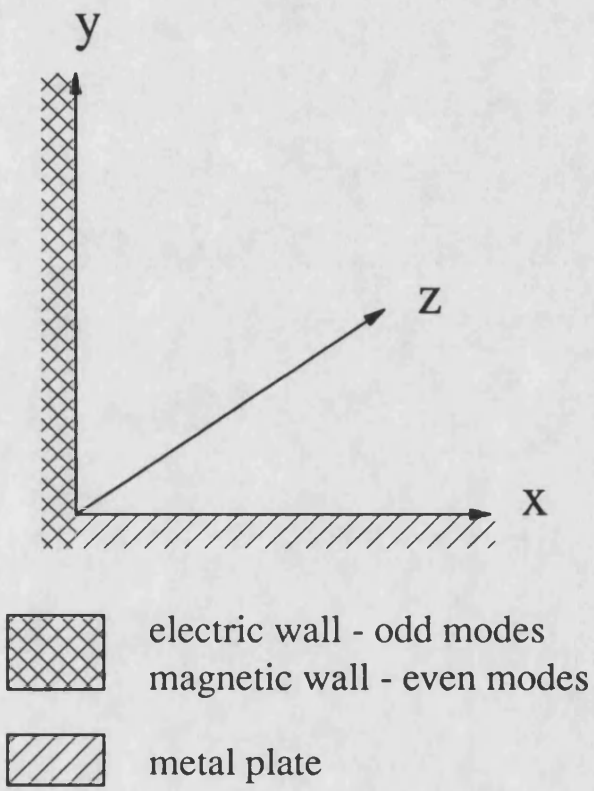

Figure 3.4: Region I understood as a quarter open space

- $E_z = \partial H_z/\partial y = 0$ $\quad 0 \leq x \leq d/2; y = 0$
- $E_x = \partial H_x/\partial x = 0$ $\quad x = 0;\ 0 \leq y < \infty \quad \& \quad 0 \leq x \leq d/2;\ y = 0$
- E_z, H_z, H_y $\quad$ are continuous across the interface plane I
- H_y, E_x, H_x $\quad$ possess a weak $r^{-1/3}$ type singularity at $x = d/2;\ y = 0$

The scalar mode function is found to be

$$\Psi_\rho(x,z) = \sqrt{\frac{2}{\pi}} \sin k_{x\rho} x \frac{1}{\sqrt{2\pi}} \exp(-\jmath\beta_e z) \tag{3.22}$$

Combining this mode function together with the expressions

$$\begin{aligned} V_\rho(\rho, y) &= V_\rho(\rho)\sqrt{\frac{2}{\pi}} \sin k_{y\rho} y \\ I_\rho(\rho, y) &= I_\rho(\rho)\sqrt{\frac{2}{\pi}} \cos k_{y\rho} y \end{aligned} \tag{3.23}$$

and substituting them into (3.12) next expressions for the five component field description under LSE polarization for a quadrant open space is obtained:

$$\begin{aligned} E_x &= -\int_0^\infty d\rho V_\rho(\rho) \frac{\jmath\beta_e}{\sqrt{\beta_e^2 + k_{x\rho}^2}} \sqrt{\frac{2}{\pi}} \sin k_{x\rho} x \sqrt{\frac{2}{\pi}} \sin \rho y \\ E_z &= -\int_0^\infty d\rho V_\rho(\rho) \frac{k_{x\rho}}{\sqrt{\beta_e^2 + k_{x\rho}^2}} \sqrt{\frac{2}{\pi}} \cos k_{x\rho} x \sqrt{\frac{2}{\pi}} \sin \rho y \\ E_y &= 0 \\ H_x &= -\int_0^\infty d\rho I_\rho(\rho) \frac{k_{x\rho}}{\sqrt{\beta_e^2 + k_{x\rho}^2}} \sqrt{\frac{2}{\pi}} \cos k_{x\rho} x \sqrt{\frac{2}{\pi}} \cos \rho y \\ H_z &= -\int_0^\infty d\rho I_\rho(\rho) \frac{\jmath\beta_e}{\sqrt{\beta_e^2 + k_{x\rho}^2}} \sqrt{\frac{2}{\pi}} \sin k_{x\rho} x \sqrt{\frac{2}{\pi}} \cos \rho y \\ H_y &= -\frac{1}{\jmath\omega\mu_0} \int_0^\infty d\rho V_\rho(\rho) \sqrt{\beta_e^2 + k_{x\rho}^2} \sqrt{\frac{2}{\pi}} \sin k_{x\rho} x \sqrt{\frac{2}{\pi}} \sin \rho y \end{aligned} \tag{3.24}$$

Having evaluated expressions for the field components, and by taking advantage of integral operator equation (3.18) the link between the electric field E_z and magnetic field H_y at the discontinuity plane $x = d/2$ is derived as:

$$\begin{aligned} E_z(x = d/2, y) &= \int_0^\infty dy' \int_0^\infty d\rho \, z_{1,e}(\rho) \sqrt{\frac{2}{\pi}} \sin \rho y \sqrt{\frac{2}{\pi}} \sin \rho y' \, H_y(x = d/2, y') \\ E_1 &= \mathcal{Z}_{1,e}(y, y') \cdot H_1 \end{aligned} \tag{3.25}$$

where the kernel $\mathcal{Z}_{1,e}(y, y')$ is symmetrical in variables y and y', and often is called a Green's function, although strictly speaking it is not a true Green's function in the normal sense [12]. This operator equation is given as:

$$\begin{aligned} \mathcal{Z}_{1,e} &= \int_0^\infty d\rho \, z_{1,e}(\rho) \sqrt{\frac{2}{\pi}} \sin \rho y \sqrt{\frac{2}{\pi}} \sin \rho y' \\ z_{1,e}(\rho) &= j\omega\mu_0 \frac{k_{x\rho}}{k_{x\rho}^2 + \beta_e^2} \cot(k_{x\rho} \frac{d}{2}) \end{aligned} \tag{3.26}$$

This impedance represents the driving point impedance of a quarter open space region of length $d/2$ in length when an ideal magnetic wall is placed at the $x = 0$ plane, as shown in Fig.3.4.

Odd mode

For the case of odd mode, electric wall is placed as $x = 0$ plane and boundary conditions imposed by such geometry can be written as:

- $H_x = \partial E_x / \partial x = 0$ $\quad x = 0;\ 0 \leq y < \infty$
- $\partial H_y / \partial x = 0$ $\quad x = 0;\ 0 \leq y < \infty$
- $H_y = 0$ $\quad 0 \leq x \leq d/2;\ y = 0$
- $E_z = \partial H_z / \partial x = 0$ $\quad x = 0;\ 0 \leq y < \infty 5\text{mm}\&\quad 0 \leq x \leq d/2;\ y = 0$
- $E_z = \partial H_z / \partial y = 0$ $\quad 0 \leq x \leq x/2; y = 0$
- E_z, H_z, H_y $\quad$ are continuous across the interface plane

- H_y, E_x, H_x possess a weak $r^{-1/3}$ type singularity at $x = d/2;\ y = 0$

The scalar mode function, complying with the above boundary conditions used to evaluate field components for odd modes of region I is assumed to be:

$$\Psi_\rho(x,z) = \sqrt{\frac{2}{\pi}}\cos(k_{x\rho}x)\,\frac{1}{\sqrt{2\pi}}\exp(-\jmath\beta_o z) \tag{3.27}$$

The equations (3.23) are also valid for odd modes, and using the same procedure as for even modes the expressions for field components for odd mode of region I under LSE polarization are obtained:

$$\begin{aligned}
E_x &= \int_0^\infty d\rho\, V_\rho(\rho)\,\frac{\jmath\beta_o}{\sqrt{\beta_o^2 + k_{x\rho}^2}}\sqrt{\frac{2}{\pi}}\cos(k_{x\rho}x)\sqrt{\frac{2}{\pi}}\sin(\rho y) \qquad (3.28)\\
E_z &= \int_0^\infty d\rho\, V_\rho(\rho)\,\frac{k_{x\rho}}{\sqrt{\beta_o^2 + k_{x\rho}^2}}\sqrt{\frac{2}{\pi}}\sin(k_{x\rho}x)\sqrt{\frac{2}{\pi}}\sin(\rho y)\\
E_y &= 0\\
H_x &= \int_0^\infty d\rho\, I_\rho(\rho)\frac{k_{x\rho}}{\sqrt{\beta_o^2 + k_{x\rho}^2}}\sqrt{\frac{2}{\pi}}\sin(k_{x\rho}x)\sqrt{\frac{2}{\pi}}\cos(\rho y)\\
H_z &= \int_0^\infty d\rho\, I_\rho(\rho)\,\frac{\jmath\beta_o}{\sqrt{\beta_o^2 + k_{x\rho}^2}}\sqrt{\frac{2}{\pi}}\cos(k_{x\rho}x)\sqrt{\frac{2}{\pi}}\cos(\rho y)\\
H_y &= -\frac{1}{\jmath\omega\mu_0}\int_0^\infty d\rho\, V_\rho(\rho)\sqrt{\beta_e^2 + k_{x\rho}^2}\sqrt{\frac{2}{\pi}}\cos(k_{x\rho}x)\sqrt{\frac{2}{\pi}}\sin(\rho y)
\end{aligned}$$

Again applying the same procedure as in the even case, the integral operator equation is established as

$$\begin{aligned}
E_z(x = \frac{d}{2}, y) &= -\int_0^\infty dy' \int_0^\infty d\rho\, z_{1,o}(\rho)\sqrt{\frac{2}{\pi}}\sin(\rho y)\sqrt{\frac{2}{\pi}}\sin(\rho y')\, H_y(x = \frac{d}{2}, y')\\
E_1 &= \mathcal{Z}_{1,o}(y,y')\cdot H_1 \qquad (3.29)
\end{aligned}$$

giving the impedance operator for odd case as:

$$\mathcal{Z}_{1,o} = \int_0^\infty d\rho\, z_{1,o}(\rho) \sqrt{\frac{2}{\pi}} \sin(\rho y) \sqrt{\frac{2}{\pi}} \sin(\rho y') \tag{3.30}$$

$$z_{1,o}(\rho) = j\omega\mu_0 \frac{k_{x\rho}}{k_{x\rho}^2 + \beta_o^2} \tan(k_{x\rho}\frac{d}{2})$$

3.4.2 Region II: a grounded slab waveguide

Region II is understood as a grounded dielectric slab waveguide energized in the x directions. Grounded slab guide supports two type of waves, discrete and continuous. Bound modes surface waves are typified by a field that decays exponentially away from dielectric surface, with most of field contained in or near the dielectric. At higher frequencies the field generally becomes more tightly bound to the dielectric. Due to the presence of the dielectric, the phase velocity of a surface wave is less then the velocity of light in a vacuum. The grounded slab waveguide is shown in Fig.3.5. Two distinct regions appear in this structure, the dielectric and air regions. Modes of both polarization, TE and TM, can be supported by this dielectric slab structure.

In order to maintain field continuity between the different regions, the TE modes of grounded dielectric slab guide must be chosen when LSE polarization of the IDG is considered.

As continuity of field should be imposed in the air region only, the field components for this region will be derived. The scalar mode function for TE modes of dielectric slab waveguide are

- discrete modes

$$\Psi_\nu(y) = A''_\nu \exp(-\gamma''_\nu y) \qquad y \geq 0 \tag{3.31}$$

$$A''_\nu = \sqrt{\frac{2}{h + \frac{1}{\gamma''_\nu}}} \sin(q''_\nu h)$$

$$0 = \gamma''_\nu + q''_\nu \cot(q''_\nu h) \tag{3.32}$$

γ''_ν - y directed decay constant for bounded modes in air region of a grounded dielectric slab guide

q''_ν - y directed the bounded mode phase constant in dielectric region of a grounded slab guide

- continuous modes

$$\Psi_\rho(y,\rho) = \sqrt{\frac{2}{\pi}}\sin(q''_\rho + \alpha'') \qquad y \geq 0 \tag{3.33}$$
$$\cot\alpha'' = \frac{q''_\rho}{\rho}\cot q''_\rho h$$

q''_ρ - y directed the continuous mode phase constant in dielectric region of a grounded slab guide

ρ - the air region wave number for continuous modes in the y direction of a grounded dielectric slab guide

The angle α'' above represents the phase shift of a planar wave with propagation constants (q''_ρ, β) undergoes upon impinging on the slab and reemerging from it.

The slab guide is a planar structure and assumes two dimensional dependence of field components. As IDG is a three dimensional structure, field components and mode impedances are modified in order to include z dependence of the field components.

Applying again the procedure described by equations (3.12) to (3.20), the air region field components for the TE modes of a grounded dielectric slab waveguide with three-dimensional field distribution are derived as:

$$E_z(x,y) = \sum_\nu V''_\nu(\omega)\frac{jk_{x\nu}}{\sqrt{k_{x\nu}^2+\beta_{e,o}^2}}A''_\nu\exp(-\gamma''_\nu y) + \\ + \int_0^\infty d\rho\, V''_\rho(\rho)\frac{jk_{x\rho}}{\sqrt{k_{x\rho}^2+\beta_{e,o}^2}}\sqrt{\frac{2}{\pi}}\sin(\rho y+\alpha'') \tag{3.34}$$
$$H_x(x,y) = \sum_\nu I''_\nu(\omega)\frac{jk_{x\nu}}{\sqrt{k_{x\nu}^2+\beta_{e,o}^2}}A''_\nu\exp(-\gamma''_\nu y) +$$

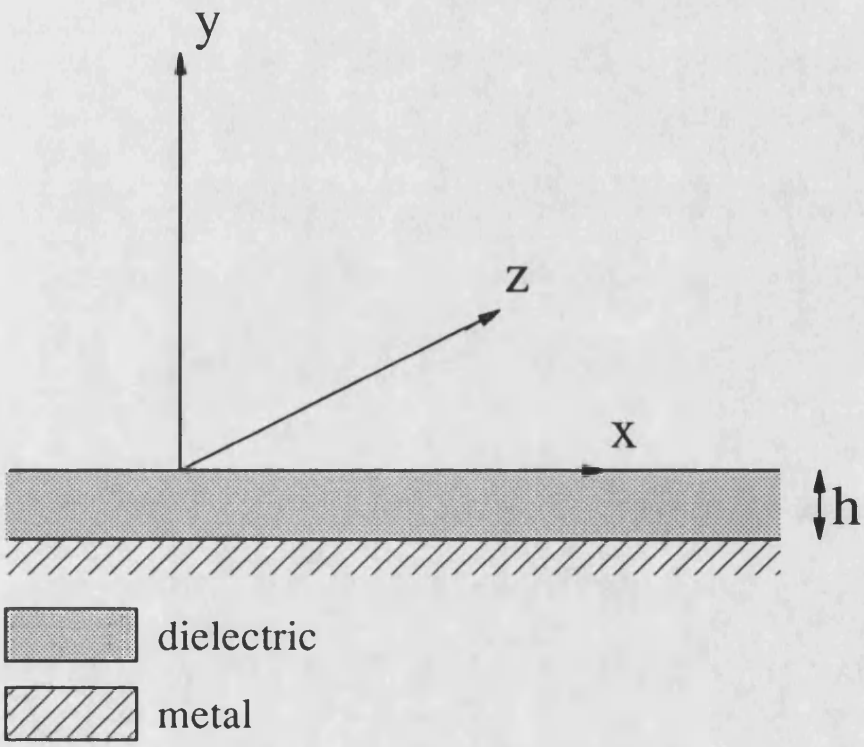

Figure 3.5: Region II understood as grounded slab dielectric guide.

$$+ \int_0^\infty d\rho\, I''_\rho(\rho)\, \frac{jk_{x\rho}}{\sqrt{k_{x\rho}^2+\beta_{e,o}^2}} \sqrt{\frac{2}{\pi}} \sin(\rho y+\alpha'')$$

$$H_y(x,y) = -\frac{1}{j\omega\mu_0} \sum_\nu V''_\nu(\omega) \sqrt{k_{x\nu}^2+\beta_{e,o}^2}\, A''_\nu \exp(-\gamma''_\nu y) +$$

$$+ \int_0^\infty d\rho\, V''_\rho(\rho)\, \frac{jk_{x\rho}}{\sqrt{k_{x\rho}^2+\beta_{e,o}^2}} \sqrt{\frac{2}{\pi}} \sin(\rho y+\alpha'')$$

The impedance operator linking E_z and H_y field components is found to by replacing the voltage amplitudes in (3.34) by

$$V''_\nu(\omega) = -j\omega\mu_0 \int_0^\infty dy'\, \frac{1}{\sqrt{k_{x\nu}^2+\beta_{e,o}^2}}\, A''_\nu \exp(-\gamma''_\nu y')\, H_y(y') \tag{3.35}$$

$$V'_\rho(\omega) = -j\omega\mu_0 \int_0^\infty dy'\, \frac{1}{\sqrt{k_{x\rho}^2+\beta_{e,o}^2}} \sqrt{\frac{2}{\pi}} \sin(\rho y+\alpha'')\, H_y(y')$$

which yields to the impedance operator equation

$$Z_{sg} = \sum_{\nu=1}^{N_{sw}} z_\nu\, A''_\nu \exp(-\gamma''_\nu y)\, A''_\nu \exp(-\gamma''_\nu y') \tag{3.36}$$

$$+ \int_0^\infty d\rho\, z_\rho \sqrt{\frac{2}{\pi}} \sin(\rho y+\alpha'') \sqrt{\frac{2}{\pi}} \sin(\rho y'+\alpha'')$$

where mode impedances are found to be

$$z_\nu = \omega\mu_0 \frac{k_{x\nu}}{k_{x\nu}^2+\beta_{e,o}^2} \qquad z_\rho = \omega\mu_0 \frac{k_{x\rho}}{k_{x\rho}^2+\beta_{e,o}^2} \tag{3.37}$$

N_{sw} stands for the total number of surface modes which can be supported by the slab guide structure. This number depends on slab geometry, dielectric constant and working frequency. As described earlier, for the purpose of including the mutual interaction of two discontinuity steps on the finite length of dielectric guide, region II was modeled as two port network Fig.3.2 [13]. In order to make the model correct, the integral operator (3.36) should be modified with proper expressions to give the correct sense to the operators $\mathcal{Z}_{11}$ and $\mathcal{Z}_{12}$.

The operator Z_{11} was defined as driving point impedance of a ground slab dielectric guide of length $L = a$ when the other port is short-circuited, or equivalently, an electric wall placed at the other end of the waveguide. With correspondence to the transmission line representation, and modeling electric field as voltage and magnetic as current on the line, the driving point impedance of short-circuited line is

$$z_{11} = Z_0 \coth(\jmath k_x a) = -\jmath Z_0 \cot(k_x a) \tag{3.38}$$

The impedance relating input voltage and output current on the open-ended transmission line is established as:

$$z_{12} = Z_0 \frac{1}{\sin(\jmath k_x a)} = -\jmath Z_0 \csc(k_x a) \tag{3.39}$$

Modifying the mode impedances given in (3.37) according to equations (3.38) and (3.39) the operators take the form:

$$\begin{aligned}
\mathcal{Z}_{11} &= -\sum_{\nu=1}^{N_{sw}} \jmath\omega\mu_0 \frac{k_{x\nu}}{k_{x\nu}^2 + \beta_{e,o}^2} \cot(k_{x\nu}a)\, A_\nu'' \exp(-\gamma_\nu'' y)\, A_\nu'' \exp(-\gamma_\nu'' y') - \\
&- \int_0^\infty d\rho\, \jmath\omega\mu_0 \frac{k_{x\rho}}{k_{x\rho}^2 + \beta_{e,o}^2} \csc(k_{x\rho}a) \sqrt{\frac{2}{\pi}} \sin(\rho y + \alpha'') \sqrt{\frac{2}{\pi}} \sin(\rho y' + \alpha'') \qquad (3.40) \\
\mathcal{Z}_{12} &= -\sum_{\nu=1}^{N_{sw}} \jmath\omega\mu_0 \frac{k_{x\nu}}{k_{x\nu}^2 + \beta_{e,o}^2} \csc(k_{x\nu}a)\, A_\nu'' \exp(-\gamma_\nu'' y)\, A_\nu'' \exp(-\gamma_\nu'' y') - \\
&- \int_0^\infty d\rho\, \jmath\omega\mu_0 \frac{k_{x\rho}}{k_{x\rho}^2 + \beta_{e,o}^2} \csc(k_{x\rho}a) \sqrt{\frac{2}{\pi}} \sin(\rho y + \alpha'') \sqrt{\frac{2}{\pi}} \sin(\rho y' + \alpha'')
\end{aligned}$$

These equations are applicable to a slab grounded dielectric guide section where the properties of the discontinuity planes on both sides of the section are identical.

However, non-symmetrical case is also very interesting for consideration. Such case may occur when metal wall separating dielectric fillings of two coupled IDGs are lowered on purpose to control the coupling between the guides. In that case the impedance operator matrix describing region II is not symmetric any more. If $\Psi_{1\nu}$ and $\Psi_{1\rho}$ represent scalar mode function describing the field distribution on the first discontinuity plane and accordingly $\Psi_{2\nu}$

and $\Psi_{2\rho}$ describe the second discontinuity plane, then impedance integral operators of the two port network representation are given by:

$$\begin{aligned}
\mathcal{Z}_{11} &= \sum_{\nu} z_{11\nu}\Psi_1(y)\Psi_1'(y') + \int_0^{\infty} d\rho z_{11\rho}\Psi_{1\rho}(y)\Psi_{1\rho}'(y') \qquad (3.41)\\
\mathcal{Z}_{12} &= \sum_{\nu} z_{12\nu}\Psi_1(y)\Psi_2'(y') + \int_0^{\infty} d\rho z_{12\rho}\Psi_{1\rho}(y)\Psi_{2\rho}'(y')\\
\mathcal{Z}_{21} &= \sum_{\nu} z_{12\nu}\Psi_2(y)\Psi_1'(y') + \int_0^{\infty} d\rho z_{12\rho}\Psi_{2\rho}(y)\Psi_{1\rho}'(y')\\
\mathcal{Z}_{22} &= \sum_{\nu} z_{11\nu}\Psi_2(y)\Psi_2'(y') + \int_0^{\infty} d\rho z_{11\rho}\Psi_{2\rho}(y)\Psi_{2\rho}'(y')
\end{aligned}$$

In order to determine wave numbers of slab region we eliminate $k_{x\nu}$ from:

$$\begin{aligned}
q_\nu''^2 + k_{x\nu}^2 &= \epsilon_r k_0^2 \qquad (3.42)\\
-\gamma_\nu''^2 + k_{x\nu}^2 &= k_0^2
\end{aligned}$$

leading to

$$q_\nu''^2 + \gamma_\nu''^2 = (\epsilon_r - 1)k_0^2 \qquad (3.43)$$

This equation together with (3.32) forms a system of two non-linear equations and their graphical solutions is represented on Fig.3.6. Solutions with negative γ_ν'' are called improper modes. Such modes are discarded in the physical ground that they do not decay in y direction and therefore carry infinite power.

The number of valid solutions determines the value for N_{sw}.

Combination of (3.43) and (3.32) yields to the alternative transcendental equation:

$$\frac{q_\nu''^2}{\sin^2(q_\nu'' h)} = (\epsilon_r - 1)k_0^2 \qquad (3.44)$$

The solutions of this equation in graphical form are shown in Fig.3.7. Function on LHS of (3.44) is plotted with solid line and RHS of same equation is represented by a straight doted line.

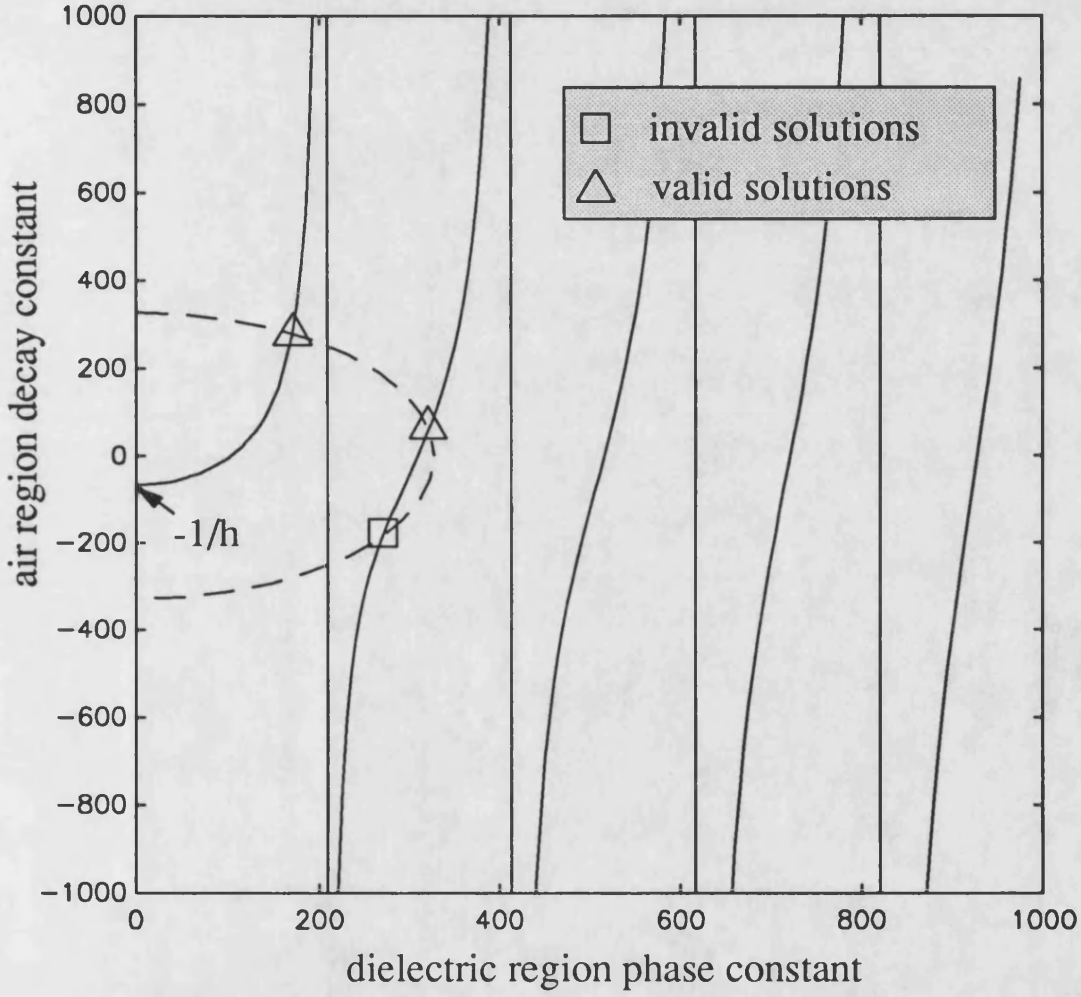

Figure 3.6: The graphical representation of solutions for system of two nonlinear equations determining air decay and dielectric phase constant for grounded slab guide under LSE polarization. The shown results are for the d=15.24mm thick guide with $\epsilon_r = 2.08$ at 15 GHz.

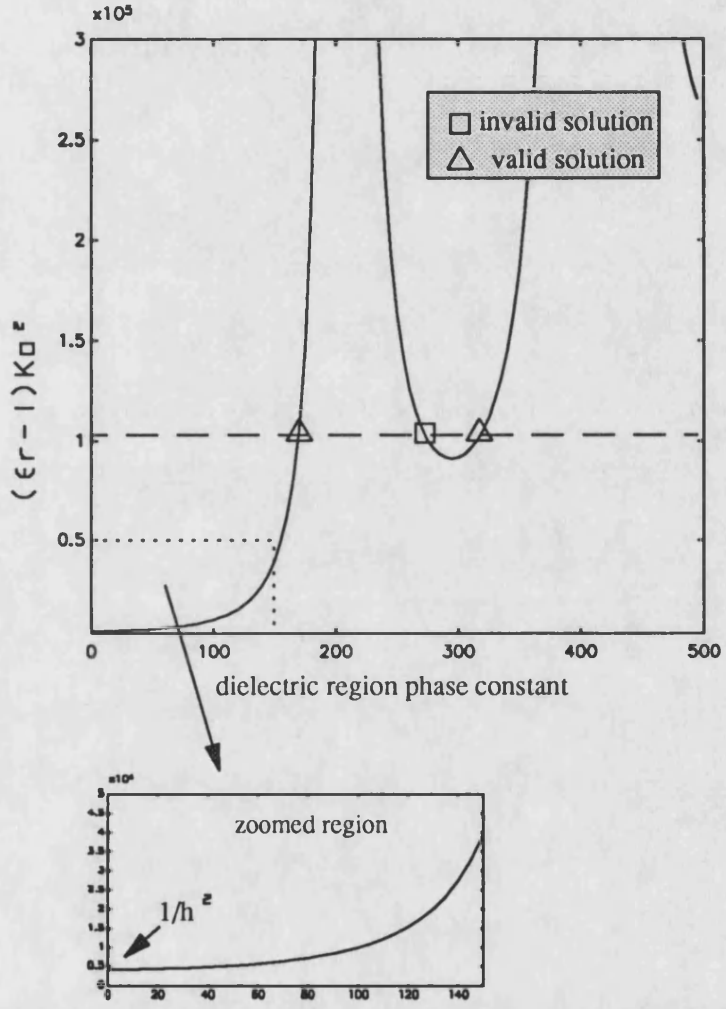

Figure 3.7: Graphical representation and phase constant solutions obtained from transcendental equation (3.44). The air decay constant is then determined from (3.32). The shown results are for the $h = 15.24mm$ thick dielectric slab guide with $\epsilon_r = 2.08$ at $15GHz$ under TE polarization. The zoomed region shows that there are a values of $\epsilon_r K_0^2$ for which no solutions of (3.44) exist. This occurs at the frequencies bellow TE mode cut-off.

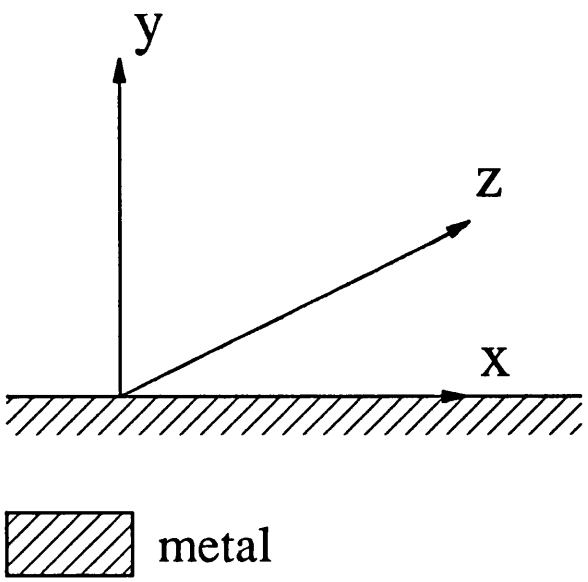

Figure 3.8: Region III understood as a half open space

3.4.3 Region III: a half open space

Region III is treated as a half open space in Fig.3.8 and as such it supports continuous modes. The same procedure as in two previous cases, for field components evaluation has been involved again.

Boundary conditions for region III are

- $E_x = \partial H_x/\partial x = 0$ $\quad 0 \leq x \leq \infty; y = 0$
- $E_z = \partial H_z/\partial y = 0$ $\quad 0 \leq x \leq \infty; y = 0$
- $H_y = 0$ $\quad 0 \leq x \leq \infty; y = 0$
- E_z, H_z, H_y $\quad$ are continuous across the interface plane II
- H_y, E_x, H_x $\quad$ have a weak $r^{-1/3}$ type singularity at $x = d/2 + a;\ y = 0$

The scalar mode functions satisfying the above boundary conditions under LSE^y polarization is found as

$$\Psi_\rho = \frac{1}{\sqrt{2\pi}} \exp(-\jmath k_x x) \frac{1}{\sqrt{2\pi}} \exp(-\jmath \beta_{e,o} z) \tag{3.45}$$

Substitution of these expression into equations (3.12)-(3.20) and taking into account relations for the y dependence of voltage and current magnitude given by (3.23) and (3.24) yields the field component expressions:

$$\begin{aligned}
E_x &= -\int_0^\infty d\rho\, V_\rho(\rho) \frac{\jmath \beta_{e,o}}{\sqrt{k_{x\rho}^2 + \beta_{e,o}^2}} \frac{1}{\sqrt{2\pi}} \exp(-\jmath k_x x) \sqrt{\frac{2}{\pi}} \sin(\rho y) \qquad (3.46)\\
E_y &= 0\\
E_z &= \int_0^\infty d\rho\, V_\rho(\rho) \frac{\jmath k_{x\rho}}{\sqrt{k_{x\rho}^2 + \beta_{e,o}^2}} \frac{1}{\sqrt{2\pi}} \exp(-\jmath k_x x) \sqrt{\frac{2}{\pi}} \sin(\rho y)\\
H_x &= \int_0^\infty d\rho\, I_\rho(\rho) \frac{\jmath k_{x\rho}}{\sqrt{k_{x\rho}^2 + \beta_{e,o}^2}} \frac{1}{\sqrt{2\pi}} \exp(-\jmath k_x x) \sqrt{\frac{2}{\pi}} \cos(\rho y)\\
H_y &= -\frac{1}{\jmath \omega \mu_0} \int_0^\infty d\rho\, V_\rho(\rho) \sqrt{k_{x\rho}^2 + \beta_{e,o}^2} \frac{1}{\sqrt{2\pi}} \exp(-\jmath k_x x) \sqrt{\frac{2}{\pi}} \sin(\rho y)\\
H_z &= \int_0^\infty d\rho\, I_\rho(\rho) \frac{\jmath \beta_{e,o}}{\sqrt{k_{x\rho}^2 + \beta_{e,o}^2}} \frac{1}{\sqrt{2\pi}} \exp(-\jmath k_x x) \sqrt{\frac{2}{\pi}} \cos(\rho y)
\end{aligned}$$

The Green's function representing the impedance operator on the second discontinuity plane, giving the driving point impedance for a half open space is

$$\begin{aligned}
Z_3 &= \int_0^\infty d\rho\, z_3(\rho) \sqrt{\frac{2}{\pi}} \sin(\rho y) \sqrt{\frac{2}{\pi}} \sin(\rho y') \qquad (3.47)\\
z_3(\rho) &= \omega \mu_0 \frac{k_{x\rho}}{k_{x\rho}^2 + \beta_{e,o}^2}
\end{aligned}$$

3.5 TRD Formulation for IDG Array

Consider the IDG structure represented on Fig.3.10 consisting of from three identical guides. Applying the same approach as has been done for the case of two coupled IDG, four homo-

geneous regions can be distinguished in halved structure by placing three separation walls as indicated in Fig.3.10. On each of these planes continuity of transverse field should be satisfied. The two regions bounded with discontinuity planes will be modeled with two port operator networks in order to take into account multiple reflection between discontinuities. Two outer regions are represented with driving point impedance operators. Referring to the network representation from Fig.3.10, the next identities can be written

$$\begin{aligned} E_1 &= Z_1 \cdot H_1 \\ E_1' &= Z_{11}' \cdot H_1' + Z_{12}' \cdot H_2' \\ E_2' &= Z_{12}' \cdot H_1' + Z_{11}' \cdot H_2' \\ E_2'' &= -Z_{11}'' \cdot H_2'' + Z_{12} \cdot H_3'' \\ E_3'' &= -Z_{12}'' \cdot H_2'' + Z_{22} \cdot H_3'' \\ E_3 &= -Z_3 \cdot H_3 \end{aligned} \tag{3.48}$$

where dot product should be understood in the sense of operator multiplication.
Applying boundary conditions:

$$\begin{aligned} E_1 = E_1' \qquad E_2' = E_2'' \qquad E_3'' = E_3 \\ H_1 = H_1' \qquad H_2' = H_2'' \qquad H_3'' = H_3 \end{aligned}$$

yields the TRD operator equation for three mutually coupled IDGs.

$$\begin{vmatrix} 0 \\ 0 \\ 0 \end{vmatrix} = \begin{vmatrix} Z_{11}' - Z_1 & Z_{12}' & 0 \\ Z_{21}' & Z_{22}' + Z_{11}'' & -Z_{12}'' \\ 0 & -Z_{21}'' & Z_{22}'' + Z_3 \end{vmatrix} \cdot \begin{vmatrix} H_1 \\ H_2 \\ H_3 \end{vmatrix} \tag{3.49}$$

The same approach can be applied on TRD formulation of non-symmetric multi-line coupled IDG structure.

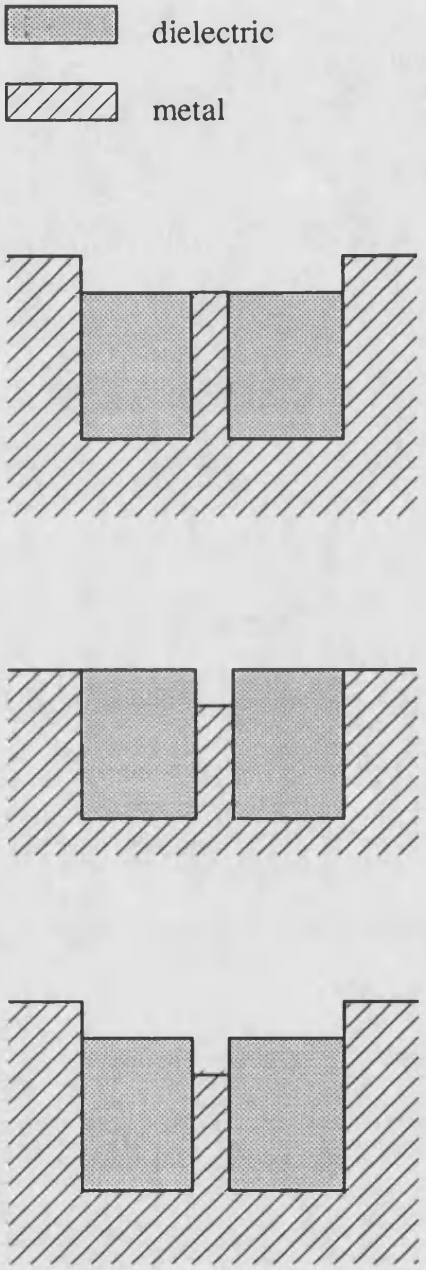

Figure 3.9: Some proposed and modified IDG structure for tighter coupling

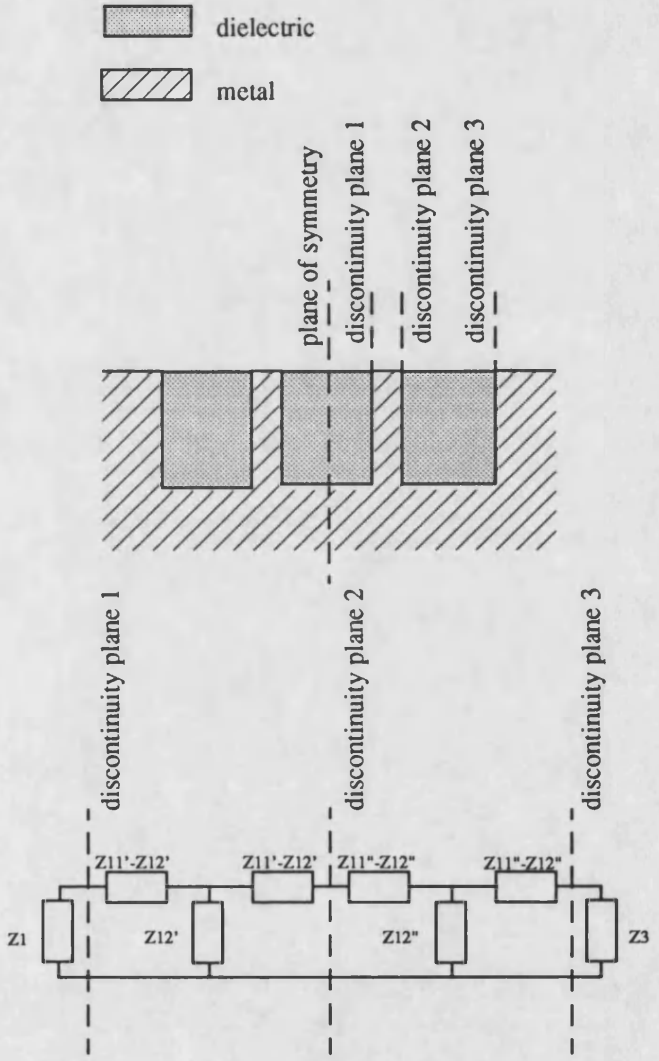

Figure 3.10: Cross section of symmetric coupled IDG array consists from three identical guides and network representation for TRD analysis.

3.6 Conclusion

The half geometry of symmetric coupled IDGs is divided into three homogeneous sections, and complete five components field description under LSE^y polarization is provided for each of them. Definition of the operator equations linking the transverse components on the separation planes and application of field continuity on each of these discontinuity planes yields a TRD dispersion equation formulation.

This approach allows treatment of any IDG configuration exhibiting a discontinuity across the x direction. Some possible modifications of the classical coupled IDG structure having purpose to increase the coupling are depicted in Fig.3.9. This structures are amenable for analysis using the described approach.

Moreover, the concept of TRD formulation for IDG array structure was introduced in this chapter, too.

References

[1] T. E. Rozzi and G. N. In't Veld

Field and Network Analysis of Interacting Step Discontinuities in Planar Dielectric Waveguides

IEEE Trans. Microwave Theory Tech., vol. MTT-27, pp303-309, April 1978

[2] T. E. Rozzi

Rigorous Analysis of the Step Discontinuity in a Planar Dielectric Waveguide

IEEE Trans. Microwave Theory Tech., vol. MTT-26, pp738-746, October 1979

[3] T. Rozzi and S. J. Hedges

Rigorous Analysis and Network Modeling of the Inset Dielectric Guide

IEEE Trans. Microwave Theory Tech., vol. MTT-35, pp823-833, Sept. 1979

[4] V. Royansky

Electromagnetic Fields and Waves

Prentice Hall, 1971, ch.6

[5] J. A. Kong

Theory of Electromagnetic Waves

John Wiley & sons, , ch.1

[6] R. E. Collin

Field Theory of Guided Waves

McGraw-Hill, 1960, ch.1

[7] L. Felsen and N. Markuvitz
Radiation and Scattering of Waves
Englewood Cliffs, Prentice Hall,1973, ch.3

[8] E. Argence and T. Kahan
Theory of Waveguides and Cavity Resonators
Blackie & Son Limited, 1967, ch.18 and 20

[9] T. Rozzi and L. Ma
Mode Completeness, Normalization and Green's Function of the Inset Dielectric Guide
IEEE Trans. Microwave Theory Tech., vol.MTT-36, March 1988 pp.542-551

[10] T. Rozzi and J. S. Kot
The Complete Spectrum of Image Line
IEEE Trans. Microwave Theory Tech., vol.MTT-37, May 1989 pp.868-876

[11] J. A. Kong
Electromagnetic Wave Theory
John Wiley & Sons Inc. 1986

[12] G. F. Roach
Green's Functions: Introductory Theory with Applications
Van Nostrand 1970

[13] N. Markuvitz
Waveguide Handbook
McGraw-Hill Book Company, 1951, ch.3

Chapter 4

Numerical Approach and Network Modeling

A mathematical model in an integral form has been established in the previous chapter. The integral formulation is characterised by use of a Green's function and its feature is that it reduces a three dimensional problem to a two dimensional one and two dimensional problem to one dimensional. One adventage of the integral equation over approaches not using a Green's function, is that integration is more stable process than differentiation from a numerical point of view.

Exact solutions of Maxwell's equations are found for each of three homogeneous regions which comprise the coupled IDGs transverse cross-section shown in Fig.3.1. The field components must satisfy boundary conditions on each of two discontinuity planes. Implementation of these conditions on field components allow us to formulate a TRD model for coupled IDGs. Projections of this mathematical model into suitable numerical form is needed in order to obtain solutions for the complete geometry.

The discretisation of the operator equation can be done in either a space or frequency domain by using proper set of basis functions. The basis function used in the spectral domain approach must be Fourier transformable. This necessity can inforce the use of a non-optimum

basis set for expansion. Moreover, when the transverse cross-section is divided into homogeneous subsections, as is done in our case, the Fourier tansform in each section must be same. This requirement can make implementation of the spectral domain approach very difficult or even impossible for some applications.

In contrast to the spectral domain approach, the space domain approach is more difficult to formulate, but fast convergence set of basis functions can alway be used.

Taking these facts into consideration, the space domain approach is choosen for use on the coupled IDGs problem.

4.1 Ritz-Galerkin's Method

Generaly speaking, an infinite amount of data is required to exactly describe an electric or magnetic field behaviour over some region of space and time. As we can deal only with a finite amount of data, some sensible approximation has to be made. For problems with linear media this approximation invariably gets a matrix form. To the mathematician this is a matter of taking a projection from an infinite dimensional Hilbert space onto a finite Euclidean space.

In order to define a Ritz-Galerkin's method for discretization of an operator equation, we start with deterministic problem.

$$\Omega\, u = v \tag{4.1}$$

where v represents the known excitation and u is the unknown and wanted field. Ω is a linear operator involving integration or differentiation or possibly both.

Adopting some known function, $b_i(s)$, usually forming a complete set, the known variable u can be approximated by expansion as

$$u = \sum_{i=1}^{N} u_i\, b_i(s) \tag{4.2}$$

In general, approximation could not exactly satisfy (4.2), but to what extent the approximation is good depends on the coefficients u_i. The exact solution of equation (4.1) is not avaliable and it is reason to introduce an error function as

$$R(s) = \Omega u - v = \Omega \sum_{i=1}^{N} u_i b_i(s) - v(s) \tag{4.3}$$

This *residual error* function [7] is equal to zero only for exact solution of equation (4.2). For good approximation residual error function should be kept as low as possible. Choosing, like b_i, another set of functions complete over the range s, an inner product $\langle x(s), y(s) \rangle$ is introduced. Rather than asking for the impossible, $R(s) = 0$ for all s, $R(s)$ is set to be orthogonal to the trial function set, w. This transforms eqn.(4.3) into N equations with N unknown u_i coeficcients

$$\left\langle \Omega \sum_{i=1}^{N} u_i b_i(s) - v(s), w_j(s) \right\rangle = 0 \tag{4.4}$$

and can be written in matrix form as

$$[\Omega]\,[u] = [v] \tag{4.5}$$

$[u]$ – column vector of elements $u_1, u_2 \ldots u_N$

$[v]$ – column vector of elements $< v(s), w_j(s) >$

$[\Omega]$ – square matrix $< \Omega b_i(s), w_j(s) >$

When the same complete set of functions is used as both the basis and the trial function set, the previosly described discretization method is known as the Ritz-Galerkin's approach, which very often results in an identical formulation to a variational approach [3].

4.2 Discretization of Operators

As same numerical approach will be applied to discretise both operator equation (3.6) and (3.10), the procedure used will be described using a unified notation. In order to do so, the

operator equation is represented as

$$\begin{vmatrix} \Lambda_{11} - \Lambda_{1e,o} & \Lambda_{12} \\ \Lambda_{12} & \Lambda_{11} + \Lambda_3 \end{vmatrix} \begin{vmatrix} X_1 \\ X_2 \end{vmatrix} = \begin{vmatrix} 0 \\ 0 \end{vmatrix} \tag{4.6}$$

where $\Lambda = \mathcal{Z}$ for LSE polarization and $\Lambda = \mathcal{Y}$ for LSM case. The operator equations derived in chapter 3 can be represented in generalized form as

- Region I

$$\Lambda_{1e,o} = \int_0^\infty d\rho \lambda_{\rho 1e,o} \Upsilon_1(y,\rho) \Upsilon_1(y',\rho) \tag{4.7}$$

- Region II

$$\Lambda_{11,12} = \sum_{\nu=1}^{N_{sw}} \lambda_{\nu\, 11,12} \Upsilon_{2\nu}(y)\, \Upsilon_{2\nu}(y) + \int_0^\infty d\rho \lambda_{\rho 11,12} \Upsilon_2(y,\rho) \Upsilon_2(y',\rho) \tag{4.8}$$

- Region III

$$\Lambda_3 = \int_0^\infty d\rho \lambda_{\rho 3} \Upsilon_1(y,\rho) \Upsilon_1(y',\rho) \tag{4.9}$$

where Υ notation stands for scalar mode function describing field distribution along the y axis. As this scalar function is the same for regions I and III, the same transformer coefficients are valid for operator discretization at these two regions. The mode function can be expanded in terms of transformer coefficients and basis set as

$$\begin{aligned} \Upsilon_1(y,\rho) &= \sum_{m=1}^{N} P_{m\rho} \mathcal{L}_m(y) \\ \Upsilon_2(y) &= \sum_{m=1}^{N} R_{m\nu} \mathcal{L}_m(y) \\ \Upsilon_2(y,\rho) &= \sum_{m=1}^{N} R_{m\rho} \mathcal{L}_m(y) \end{aligned} \tag{4.10}$$

Applying the Ritz-Galerkin's procedure on integral operators (4.7)-(4.9), discretized matrix form is reached as

$$\Lambda_{1,3} = \int_0^\infty d\rho P_\rho(\rho)^\tau \lambda_{\rho 1,3} P_\rho(\rho) \tag{4.11}$$

$$\Lambda_{11,12} = \sum_{\nu=1}^{N_{sw}} R_\nu^\tau \lambda_{\nu 11,12} R_\nu + \int_0^\infty d\rho R_\rho^\tau(\rho) \lambda_{\rho 11,12} R_\rho(\rho) \tag{4.12}$$

The resulting matrix Λ is $N \times N$ matrix where N stands for number of basis function used in the expansion. P_ρ and R_ρ are vectors of length N and R_ν is rectangular transformer matrix with dimensions of $N_{sw} \times N$. The elements of these matrix are determined accordingly to (4.5) as

$$\begin{aligned} P_{m\rho} &= <\Upsilon_1, \mathcal{L}_m> = \int_0^\infty dy \Upsilon_1(y,\rho) \mathcal{L}_m(y) \\ R_{m\nu} &= <\Upsilon_{2\nu}, \mathcal{L}> = \int_0^\infty dy \Upsilon_{2\nu}(y) \mathcal{L}_m(y) \\ R_{m\rho} &= <\Upsilon_2, \mathcal{L}_m> = \int_0^\infty dy \Upsilon_2(y,\rho) \mathcal{L}_m(y) \end{aligned} \tag{4.13}$$

By this discretization process an eigen-value problem represented by equation (4.6) is transformed into a general eigenvalue matrix equation, or what is often called the determinental equation:

$$det \begin{vmatrix} \Lambda_{11} - \Lambda_{1e,o} & \Lambda_{12} \\ \Lambda_{12} & \Lambda_{11} + \Lambda_3 \end{vmatrix} = 0 \tag{4.14}$$

Although the solution of above equation is often straightforward, it is not automatic or direct, and has to be searched for solutions in a way that cannot be infalliable. This represents the major disadvantage of problem formulated in the above described manner.

4.3 Choice of Basis Function

At the heart of the discretisation process lies the choice of basis function. The set of basis functions forms a multidimensional space in which the unknown field is defined by coordinates corresponding to the projection of that point onto each axis. These projections are mathematicaly formulated by equations (4.13). By discretising, operator equation is transformed into the function space [4].

The accuracy and extent of numerical labour involved in discretisation depends on how closely the expansion set $\mathcal{L}_m(y)$ approximates the expected field distribution across the observed volume. It means that the choice of basis set is crucial for the accurecy and efficiency of the numerical process.

The unknown field, $H_y(y)$ for LSM or $E_y(y)$ for LSM case, has to be modeled accurately on two discontinuity planes to achieve fast convergence by using a just few terms from the expansion set. The bound modes, which are considered in this thesis, decay exponentially in the y direction. The basis function should be able to model such kind of behavior. Moreover, the expansion function should also model the field to good extent for $y = 0$, where the 90^o metal edge is present. As known [1] such a metal edge will concentrate the field in the immediate vicinity and introduce singularity to the field components transverse to such an edge. The order of singularity is determined from the condition that the energy in the vicinity of edge must be finite for phisicaly relizable systems. Finite amount of energy close to the 90^o metal wedge is secured by a $r^{-1/3}$ type of singularity, where r is the radial distance from the wedge. Taking into account influence of both if the metal edges occuring in the IDG geometry, the function modeling correctly the singularity is given by

$$w_s(y) = r_1^{-1/3} r_2^{-1/3} \tag{4.15}$$

where r_1 is the distance from the edge at $x = d/2, y = 0$ and r_2 is the distance from the edge placed at $x = d/2 + a, y = 0$. The function(4.15), when transformed into a form valid at the

discontinuity planes, is written:

$$w_s = y^{-1/3}\left(\sqrt{y^2+a^2}\right)^{-1/3} = C\left(\frac{y}{a}\right)^{-1/3}\left(\sqrt{1+\left(\frac{y}{a}\right)^2}\right)^{-1/3} \tag{4.16}$$

where only first term shows singular behavior.

Now we seek for a polynomial function which has the same weight factor to that given by the above equation. The orthogonal relationship valid for the generalized Laguerre polynomial functions is

$$\int_0^\infty w_0 L_n^\alpha(y) L_m^\alpha(y) dy = \begin{cases} N_m^2 & n = m \\ 0 & n \neq m \end{cases} \qquad \Re\,\alpha > -1 \tag{4.17}$$

where the weight function and normalization coefficient are given by

$$\begin{aligned} w_0 &= y^\alpha e^{-y} \\ N_m^2 &= \frac{\Gamma(\alpha+n+1)}{n!} \end{aligned}$$

The weight function is not quite identical to the function describing singular behavior due to presence of metal wedge (4.16), but for $\alpha = -1/3$ they have same value at $y = 0$. Also both functions tends to zero when y goes to infinity.

Thus an appropriate complete set of basis functions is provided by the generalized Lagguere polynomial. The first five functions from the basis set are depicted in Fig.4.1 and expressed mathematically as

$$\mathcal{L}_m\left(\frac{y}{y_o a}\right) = \frac{1}{N_{m-1}}(y_o a)^{1/2}\left(\frac{y}{y_o a}\right)^{-1/3}\exp\left(-\frac{y}{y_o a}\right)L_{m-1}^{-1/3}\left(\frac{y}{y_o a}\right) \tag{4.18}$$

with the orthogonality relationship

$$\int_0^\infty \mathcal{L}_m\left(\frac{y}{y_o a}\right) L_n\left(\frac{y}{y_o a}\right) d\left(\frac{y}{y_o a}\right) = \sqrt{y_o a}\, N_{m-1}\delta_{mn} \tag{4.19}$$

The scale parameter y_o is introduced in order to improve convergence and its definition and

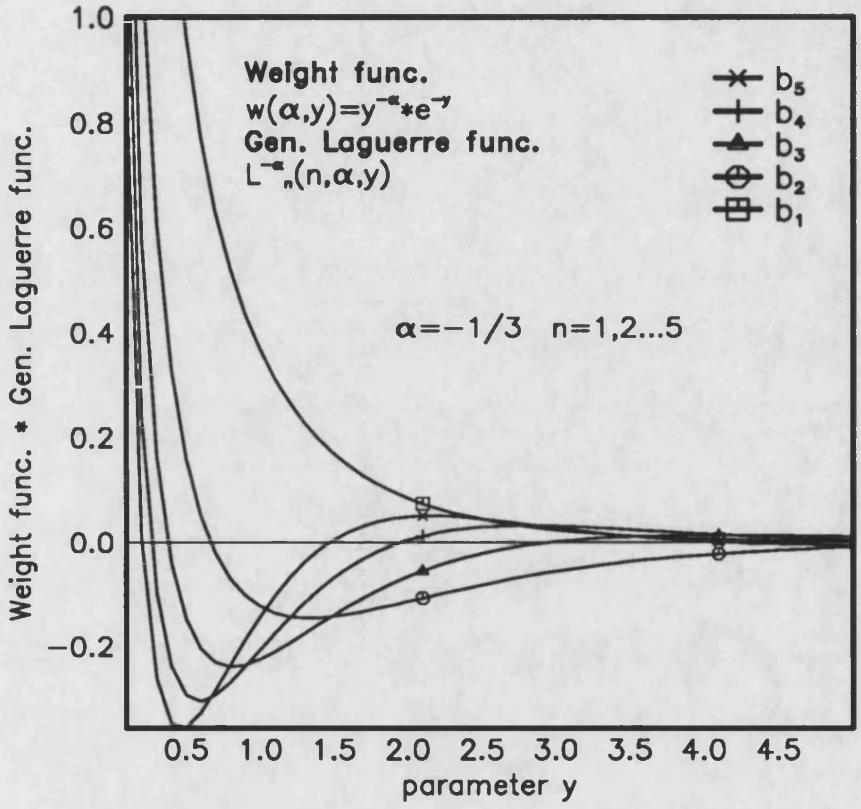

Figure 4.1: First five terms from the expansion function set

procedure for evaluation is given in the next section.

Having defined the expansion set (4.18) and subsistuting it back into (4.13), the evaluation of the transformer coefficients becomes possible. The mathemaical steps involved in the transformer coefficients derivation are presented in Appendix C.

4.4 Formulation of Scale Parameters

The scale parameter was introduced to improve convergence, or in other words, to make the expansion in terms of the basis functions a better fit to the unknown field. Although the idea is clear, the scale parameter evaluation remains undefined, and the aim of this section is to find a way of determining its value.

We start from the problem that an arbitrary vector X needs to be approximated in terms of linear combination of the independent set $\{e_1, e_2 \ldots e_n\}$. We understand by the best approximation to mean the linear combination $\sum_{i=1}^{k} b_i e_i$ that is closest to X. In other words, for the best approximation the error function, $\left|X - \sum_{i=1}^{k} b_i e_i\right|$, is smallest. An orthonormal set $\{\phi_1, \phi_2, \ldots \phi_n\}$ can be constructed from $\{b_1, b_2, \ldots, b_n\}$ by the use of the Gram-Schmidt procedure. Since both expansion sets generate the same linear manifold, the approximation of X will be done in terms of ϕ functions , $X = \sum_{i=1}^{k} a_i \phi_i$. The reason for this approach is that the coefficients $\{a_i\}$ are more easily calculated than coefficients $\{b_i\}$.

Now we should find coefficients $\{a_i\}$ which give the best approximation, or what mathematicaly can be formulated through an error function

$$f_{error} = \|X - \sum_{i=1}^{k} a_i \phi_i\|^2 \tag{4.20}$$

From [2] it has be found that the error function can be expanded as

$$f_{error} = \|X\|^2 + \sum_{i=1}^{k} |< X, \phi_i > - a_i|^2 - \sum_{i=1}^{k} |< X, \phi_i >|^2 \tag{4.21}$$

from where it is clear that minimum of error function is obtained by choosing $a_i =< X, \phi_i >$. These optimal values for the coefficients are known as the Fourier coefficients of X with respect to the orthonormal set $\{\phi_i\}$.
The error function has been reduced to

$$f_{error} = \|X\|^2 - \sum_{i=1}^{k} |< X, \phi_i >|^2 \tag{4.22}$$

The notification $\|X\|^2$ stands for the norm induced by the scalar product defined as

$$\|X\|^2 =< X, X^* > \tag{4.23}$$

In order to determine optimal scale factor, the scalar mode function $\Upsilon_{2\nu}$ will be expanded in terms of the basis function $\mathcal{L}_m(y)$ and the error function will be minimized through some optimisation procedure, giving optimal values for y_o.
The error function, given by (4.22) is reformulated in terms of the IDG's parameters as:

$$f_{error}(y_o, N, freq, \epsilon_r, h) = \sum_{\nu=1}^{N_{sw}} \left(\|\Upsilon_{2\nu}(y)\|^2 - \sum_{m=1}^{N} |< \Upsilon_{2\nu}(y), \mathcal{L}_m(y) >|^2 \right) \tag{4.24}$$

This error function represents a measure of completeness of the basis function set for the discrete modes of a grounded slab dielectric waveguide. Beside the parameters listed in the above equation, scale parameters are dependant upon type of polarization since mode function $\Upsilon_{2\nu}$ is different for the two types of polarization considered in this thesis.

4.5 Finite Network Representation

The discretized dispersion equation (4.14) is amenable for network representation. The discrete and continuous waves are transformed into a fictional N-port network which is eligible for ordinary network analysis. The network representation for coupled symmetric IDGs is depicted in Fig.4.2.

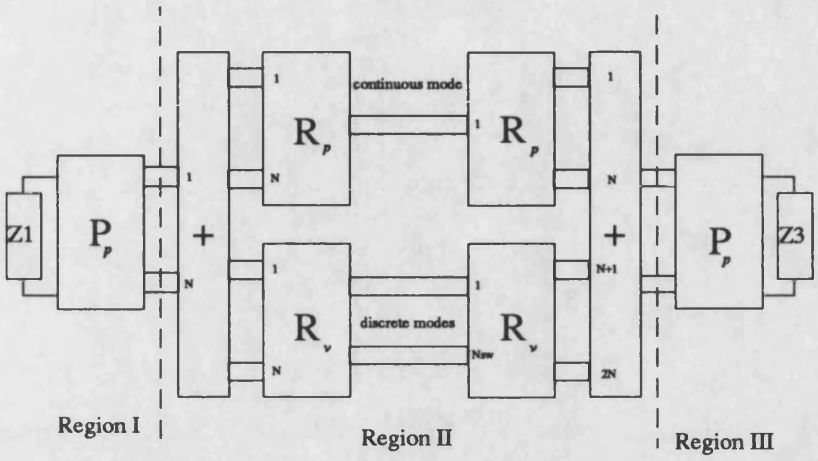

Figure 4.2: Equivalent network representation of discretized operator equations

Transformers P_ρ, R_ρ and R_ν project continuous and discrete modes for each of three regions into the N-port network. Application of standard network theory makes solution for much more complicated IDG geometries easily obtainable.

For the analysis of non-symmetric the coupled IDGs same approach as for the symmetric case can be applied by extending the analysis to include some parameters of network analysis performed in terms of chain matrix. The non-symmetric coupled IDG structure is shown in Fig.4.3. The TRD formulation is represented through an impedance operator equivalent circuit and depicted on same figure. Instead of using a determinantal equation approach to analyse the overall structure, which has already been described for the case of a symmetric triple coupled IDG array in chapter 2, the analysis of this structure will be carried out by the cascade multiplication of the chain matrices of the individual discrete networks.

If we denote by

$$Z_i = \begin{vmatrix} Z_{11i} & Z_{12i} \\ Z_{12i}^T & Z_{11i} \end{vmatrix} \tag{4.25}$$

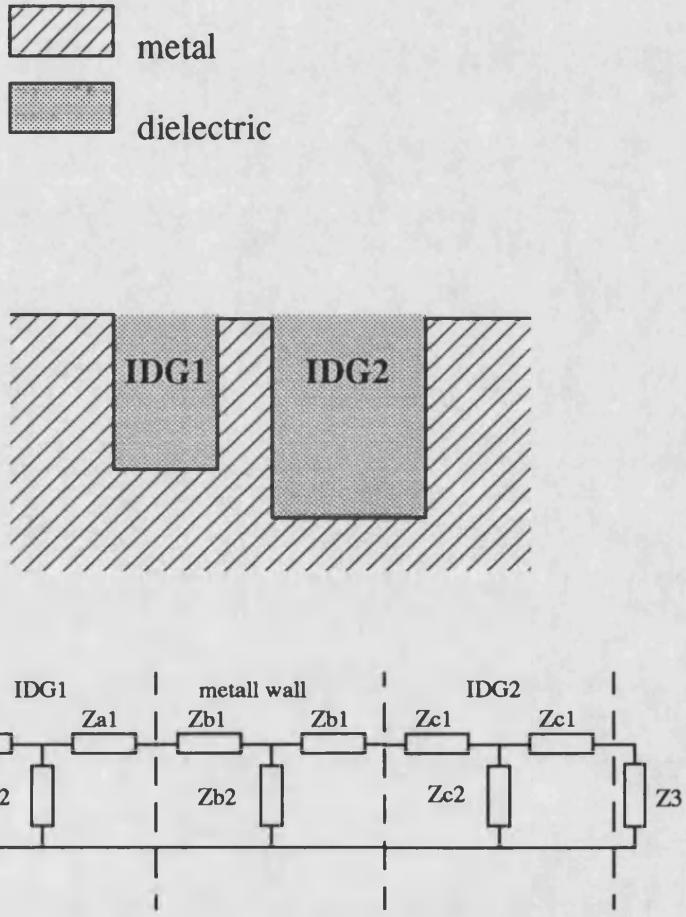

Figure 4.3: Non-symmetric coupled IDGs and equivalent circuit representation

impedance matrix of discretised operators, then the corresponding chain matrix is formulated as

$$C_i = \begin{vmatrix} Z_{11i}Z_{21i}^{-1} & Z_{11i}Z_{21i}^{-1}Z_{22i} - Z_{12i} \\ Z_{21i}^{-1} & Z_{21i}^{-1}Z_{22i} \end{vmatrix} \tag{4.26}$$

The chain matrix of overal structure is obtained by simple multiplication of three chain matrices each one coresponding to one of the three regions shown in Fig4.3.

$$C_t = C_{idg1} \cdot C_{metalwall} \cdot C_{idg2} \tag{4.27}$$

The chain matrix is transfered back into impedance form by:

$$Z_t = \begin{vmatrix} C_{11t}C_{21t}^{-1} & -C_{11t}C_{21t}^{-1}C_{22t} + C_{12t} \\ C_{21t}^{-1} & -C_{21t}^{-1}C_{22t} \end{vmatrix} = \begin{vmatrix} Z_{11t} & Z_{12t} \\ Z_{21t} & Z_{22t} \end{vmatrix} \tag{4.28}$$

Bearing in mind that the network is terminated on both sides by the driving point impedance of a half open space, the determinantal equation for non-symmetric coupled IDGs has the form

$$det \begin{vmatrix} Z_{11t} - Z_3 & Z_{12t} \\ Z_{21t} & Z_{22t} + Z_3 \end{vmatrix} = 0 \tag{4.29}$$

The above equation has to be searched for eigen-values of phase constant, which then enable calculation of coupling coefficient between two IDGs having different geometries.

4.6 Formulation of Field Components

Once having solved dispersion equation (4.14), the amplitude coefficients of unknown field can be evaluated. These coefficients can not be obtained by direct substitution of $\beta_{e,o}$ into the dispersion equation, because such a solution represent singular values for the inverse matrix. The new matrix form is nedded in order to solve (4.6) for the vectors X_1 and X_2. In order to avoid singulararity of the inverse matrix, the discrete modes of region II are pulled out and the impedance operator for this region comprises only the Green's function for continuous

waves of the dielectric slab region. The determinental equation is then reformulated as

$$\begin{vmatrix} < E_{z1}^d, \mathcal{L} > \\ < E_{z2}^d, \mathcal{L} > \end{vmatrix} = \begin{vmatrix} Z_{11}^c - Z_1 & Z_{12}^c \\ Z_{12}^c & Z_{11}^c + Z_3 \end{vmatrix} \begin{vmatrix} X_1 \\ X_2 \end{vmatrix} \tag{4.30}$$

where superscript d stands for discrete and c for continuous modes. From the above equations the amplitude coeficients in vector form are found as

$$\begin{aligned} [X_1] &= \left([Z_{11}^c - Z_1] + [Z_{12}^c][Z_{11}^c + Z_3 - Z_{12}^c]^{-1}[Z_{11}^c - Z_1 - Z_{12}^c]\right)^{-1} \left[< E_z^d, \mathcal{L}(y) >\right] \\ [X_2] &= [Z_{11}^c + Z_3 - Z_{12}^c]^{-1}[Z_{11}^c - Z_1 - Z_{12}^c][X_1] \end{aligned} \tag{4.31}$$

Having these two sets of amplitude coefficients, the unknown field H_y on both discontinuity planes is calculated from

$$\begin{aligned} H_y(x = d/2, y) &= \sum_{i=1}^{N} X_{1i}\mathcal{L}_i = [X_1]^T[\mathcal{L}] \\ H_y(x = d/2 + a, y) &= \sum_{i=1}^{N} X_{2i}\mathcal{L}_i = [X_2]^T[\mathcal{L}] \end{aligned} \tag{4.32}$$

Knowing the H_y field and puting it back into (4.6), evaluation of E_z becomes an easy task. Other field components are obtainable by application of Maxwell's equation over the volume of each of the three regions.

- Region I The unknown field on the first discontinuity plane is

$$\begin{aligned} H_y(x = d/2, y) &= \frac{1}{j\omega\mu_0}\int_0^\infty d\rho V_\rho(\rho)\sqrt{k_{x\rho}^2 + \beta^2}\sqrt{\frac{2}{\pi}}\sin(k_{x\rho}\frac{d}{2})\sqrt{\frac{2}{\pi}}\sin(\rho y) \\ &= X_1^T\mathcal{L} \end{aligned} \tag{4.33}$$

By multiplying both sides with $\sqrt{\frac{2}{\pi}}\sin(\rho y)$ and taking inner product over the seminfinite y range, the field component expressions take the form

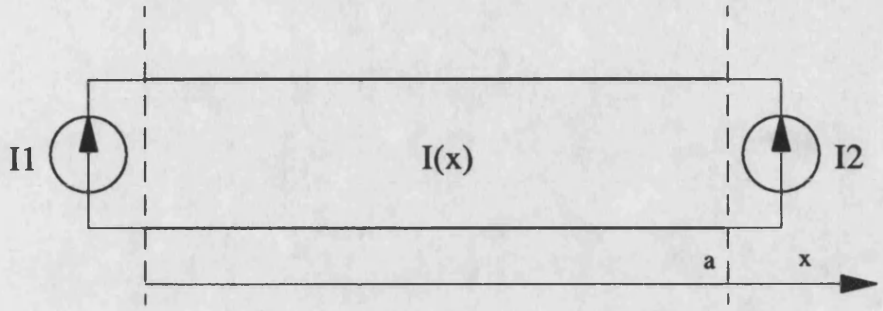

Figure 4.4: Transmission line modeling x dependance of H_y under LSE polarisation

Even mode

$$H_y(x,y) = \int_0^\infty d\rho \frac{X_1^\tau P_\rho(\rho)}{\sin(k_{x\rho}d/2)} \sqrt{\frac{2}{\pi}} \sin(k_{x\rho}x) \sqrt{\frac{2}{\pi}} \sin(\rho y) \tag{4.34}$$

$$E_z(x,y) = -\int_0^\infty d\rho \jmath\omega\mu_0 \frac{k_{x\rho}}{k_{x\rho}^2 + \beta_e} \frac{X_1^\tau P_\rho(\rho)}{\sin(k_{x\rho}d/2)} \sqrt{\frac{2}{\pi}} \sin(k_{x\rho}x) \sqrt{\frac{2}{\pi}} \sin(\rho y)$$

Odd modes

$$H_y(x,y) = \int_0^\infty d\rho \frac{X_1^\tau P_\rho(\rho)}{\cos(k_{x\rho}d/2)} \sqrt{\frac{2}{\pi}} \cos(k_{x\rho}x) \sqrt{\frac{2}{\pi}} \sin(\rho y) \tag{4.35}$$

$$E_z(x,y) = \int_0^\infty d\rho \jmath\omega\mu_0 \frac{k_{x\rho}}{k_{x\rho}^2 + \beta_e} \frac{X_1^\tau P_\rho(\rho)}{\cos(k_{x\rho}d/2)} \sqrt{\frac{2}{\pi}} \cos(k_{x\rho}x) \sqrt{\frac{2}{\pi}} \sin(\rho y)$$

- Region II First of all the x dependance of the field components in the second region should be determined. This dependance is modeled by a transmission line having excitation on both ends, as represented in Fig.4.4. The expression for the total current on the line is found to be

$$I(x) = I_1 \frac{\sin k_x(a-x)}{\sin k_x a} + I_2 \frac{\sin k_x x}{\sin k_x a} = I_1 \varphi(a-x) + I_2 \varphi(x) \tag{4.36}$$

Magnetic field is modeled as current, and thus the transverse field components are

represented as

$$
\begin{aligned}
H_y(x,y) &= -\sum_{\nu} \frac{2\gamma_\nu}{A_\nu} \left\{ X_1^\tau R_\nu \frac{\sin k_{x\nu}(a-x)}{\sin k_{x\nu} a} + X_2^\tau R_\nu \frac{\sin k_{x\nu} x}{\sin k_{x\nu} a} \right\} e^{-\gamma_\nu y} \\
&- \int_0^\infty \left\{ X_1^\tau R_\rho \frac{\sin k_{x\rho}(a-x)}{\sin k_{x\rho} a} + X_2^\tau R_\rho \frac{\sin k_{x\rho} x}{\sin k_{x\rho} a} \right\} \sqrt{\frac{2}{\pi}} \sin(\alpha + \rho y) \\
&= \sum_{\nu} \{ I_{1\nu} \varphi_\nu(a-x) + I_{2\nu} \varphi_\nu(x) \} e^{\gamma_\nu y} \\
&+ \int_0^\infty d\rho \{ I_{1\rho} \varphi_\rho(a-x) + I_{2\rho} \varphi_\rho(x) \} \sqrt{\frac{2}{\pi}} \sin(\alpha + \rho y) \qquad (4.37) \\
E_z(x,y) &= \left\{ \sum_{\nu} (I_{1\nu} z_{\nu 11} - I_{2\nu} z_{\nu 12}) \varphi_\nu(a-x) \right. \\
&+ \left. \sum_{\nu} (I_{1\nu} z_{\nu 12} - I_{2\nu} z_{\nu 12}) \varphi_\nu(x) \right\} e^{\gamma_\nu y} \\
&+ \left\{ \int_0^\infty (I_{1\rho} z_{\rho 11} - I_{2\rho} z_{\rho 12}) \varphi_\rho(a-x) \right. \\
&+ \left. \int_\rho (I_{1\rho} z_{\rho 12} - I_{2\rho} z_{\rho 12}) \varphi_\rho(x) \right\} \sqrt{\frac{2}{\pi}} \sin(\alpha + \rho y)
\end{aligned}
$$

with $\left\{ \begin{array}{c} z_{11} \\ z_{12} \end{array} \right\} = j\omega\mu_0 \frac{k_x}{k_x^2+\beta^2} \left\{ \begin{array}{c} \cot k_x a \\ \frac{1}{\sin k_x a} \end{array} \right\}$.

- Region III The transverse field components in this region were calculated as

$$
\begin{aligned}
H_y(x,y) &= \int_0^\infty X_2^\tau P_\rho(\rho) \sqrt{\frac{2}{\pi}} \sin \rho y e^{-jk_{x\rho} x} \qquad (4.38) \\
E_z(x,y) &= \int_0^\infty z_{3\rho}(\rho) X_2^\tau P_\rho(\rho) \sqrt{\frac{2}{\pi}} \sin \rho y e^{-jk_{x\rho} x}
\end{aligned}
$$

4.7 Conclusion

In this chapter Ritz-Galerkin's procedure for discretization of operator equation has been described. The choice of basis set governs both, the rate of convergence and the final accuracy of the solutions. In order to make convergence faster, the scale parameter,y_o, is introduced

into the basis function. By finding optimal value of this parameter, the basis function fits the unknown field better and less terms are needed in the expansions. This is very benefitial for the accuracy and efficency of the chosen approach.

The formulation of the problem in terms of a transverse equivalent circuit enables application of the same approach to other similar structures. Finite network representation for discretised impedance operators makes solutions for non-symmetrical coupled structure easy avaliable. The chain matrix multiplication is only needed to extend the analysis to coupled arrays of IDG lines and similar structures.

References

[1] R. Mittra and S. W. Lee

Analytical Techniques in the Theory of Guided Waves

The McMillan Company, New York 1971 ch.1

[2] B.Friedman

Lectures on application-oriented mathematics

Holden-Day Inc., San Francisko 1969,pp41-65 and 138-170

[3] I. Stakgold

Boundary Value Problems of Mathematical Physics

Vol.I, McMillan, New York pp.191-258

[4] K. Rektorys

Variational Method in Mathematics, Science and Engineering

D. Reidel Publishing Company, Praque, 1980 pp.21-178

[5] J. B. Davies

Numerical Approach to Electromagnetic Problem

from "Modern Topics in Electromagnetics and Antennas" based on lectures deliverd at the 1976 Summer Institute at the Technical University, Eindhoven, Peter Peregrinus, London 1977

[6] R. F. Harrington

Field Computation by Moment Methods

R.E. Kriger Publishing Company 1982

[7] M. Becker

The Principles and Applications of Variational Methods

M.I.T. Press, 1964

Chapter 7

Conclusion

The objective of this concluding chapter is to bring together the results of the precidings chapters and to address the major achievements of this work. This should help us to assess significance of the results and their implication on the other areas of prospective work.

7.1 Review of the Presented Work

This thesis presents work concerning the analysis of the coupled Inset Dielectric Guides (IDGs) and application of the developed analytical tools to the all passive circuits which comprise coupled IDG structures. Generally speaking, dielectric guides are intended for use in integrated circuit operating at the frequencies above 100 GHz.

Chapter I addresses the importance of milimetre waves and gives a brief comparison of IDG with other similar dielectric guiding structures such as image guide and insular guide. A brief survey of previous work on the coupled dielectric guides is presented on the basis of numerical methods used and results achieved.

The theory of coupled lines were developed a long time ago, and in Chapter 2 a brief introduction to two different types of analysis are given. For the case when symmetric lines are considered, the coupled structure can be divided by plane of symmetry and analysis is then performed in terms of even and odd mode depending on the symmetry plane nature. Odd

mode is enforced by placing metall wall as symmetry plane while magnetic wall corresponds to the even mode. In this way the analysis of a four port networks is reduced to the analysis of two two-port networks under odd and even symmetry. The general Miller's theory concerning coupling between two non-identical lines is outlined in Chapter 2, as well.
The formulation of problem, based upon the Transverse Resonance Diffraction (TRD) method is introduced in Chapter 3. The entire structure of the coupled IDG is divided into two halves by a symmetry plane, and such half structure is separated further into three homogeneous regions listed as:

- Region I : a quarter open space
- Region II : a grounded slab dielectric guide
- Region III : a half open space

These three regions are linked through the TRD formulation giving a set of coupled integral equations. This procedure requires different formulation of integral operators for the coupling of deep slot IDG from that one performed for shallow slot IDG. The derivation of field components of all three regions under LSE polarization and formulation of impedance integral operators is given in the same chapter. The same procedure but covering the case of coupling between shallow guides under LSM polarization is presented in Appendix B. The formulated matrix operator equations had to be solved by numerical means. In order to do so Galerkin's method for integral operator discretisation is used, transforming the integral operators into matrices. The order of matrix is determined by number of basis function involved in the discretisation procedure,but it also governs the computing time and convergence behavior of the numerical method. So if the basis functions closely fit unknown field, fewer of them should be used in the expansion, thereby achieving fast convergence and reduced computing time. The detailed description of the procedure, as well as choice of basis function capable of simulating singular behavior of field close to the metal edges of a IDG slot, is presented in Chapter 4.
The results obtained from a dispersion equation solutions are presented in Chapter 5. As a

result of good basis function selection, the convergence is fast. Indeed, on comparison with measured results, only four or five terms are needed in the expansion set to get an accuracy better than 0.5%. The fundamental hybrid field for a deep slot IDG is, to good approximation, LSE_{01} with constant electric field variation across the deep slot, while fundamental mode of shallow IDG structure is LSM_{11}. The results obtained for a single line are verified against both with measured and computed data obtained by other authors [1] utilizing a similar approach.

An approximate way of calculating propagation constant for deep and shallow single IDGs is established and shows rather good agreement with measured data. The coupling between coupled lines is characterized in terms of β_e and β_o, the propagation constants for even and odd modes. The difference between the two propagation constants is less pronounced at higher frequency and consequently the coupling between two guides decreases as frequency increases.

The measured characteristic of coupled IDG lines shows that such a structure gives forward coupling with very good isolation and return loss characteristics. Coupling characteristic versus frequency is represented by smooth curve having negative slope and the explanation for such behavior is found in the fact that field is more strongly confined to the dielectric insets at higher frequency, so giving less coupling. The coupling dependance on permittivity of dielectric filling was investigated as well. In order to maintain the same monomode bandwidth, the two IDGs having dielectric fillings of different permittivity must possess different slot cross-sections too. It was found that IDG with high permittivity dielectric filling does not suffer from strong coupling even for very small separation between two adjacent guides. Consequently, such structure is amenable for application in technologies where circuit integration on large scale is needed. Another good feature of the high permittivity IDG is that it has smaller dimensions of slot cross-section than the low permittivity counterparts, aimed for the same frequency range of monomode operation.

Once the solutions for β are found, the field components can be computed and plots for several modes of single and coupled guides are avaliable for deep and shallow IDG structures.

The singularity in the field pattern due to the presence of the edge discontinuity was clearly seen.

Chapter 6 is concerned with design of multihole IDG couplers. An additional mechanism, coupling through holes, was introduced in order to compensate the inherent frequency dependance of the IDG coupling characteristic. The similarity between the field distribution of the TE_{01} mode of metal wave guide and the LSE_{01} IDG mode allows use of Bethe's theory for calculating the coupling through the holes.

The synthesis of couplers presented is based on an approach utilizing analysis and optimization procedures. Two types of analysis were developed:

- first, coupling mechanisms are treated as independent and total coupling is found as sum of *discrete* coupling through holes and *continuous* wave coupling through air region of the coupled IDG section.

- second, coupling mechanisms are considered in their interaction. Hole coupling is modeled by means of a lumped circuit which is placed in the middle of a transmission line section having the same propagation parameters as the IDG line. Analysis is again performed in terms of even and odd modes. Correction due to finite thickness of the separation wall is modeled by the means of a reactive susceptance and included in the lumped circuit model.

Two couplers are synthesized, for -3dB and -10dB coupling levels. The maximal obtainable flat coupling is presented in graphic form and can be used for the purpose of guide spacing and coupler length assessment.

The theory developed is compared with measurements done on the $-3dB$ and $-10dB$ coupler test pieces. The responses measured do not obey power conservation rule and the application of unitary principle on coupler scattering parameters yields conclusion that $10 - 20\%$ of power missing. Knowing that line loss of single IDG is very small [2], the extra power loss is associated with radiation loss. Bearing this in mind, the agreement between predicated and measured data is rather very good.

The approach where the coupling mechanisms are considered as interacting, tends to better fit experimentally obtained data, especially for the higher levels of the coupled power. The measured isolation and return loss are of much higher level than analytically predicated. The real coupled IDG isolation is masked by direct energy coupling between two aperture of adjacent transition sections. In order to produce IDG couplers of very high directivity, the metal wave guide to IDG transition of better characteristics is needed.

7.2 Suggested Further Work

The work on coupled IDG lines presented here opens up possibility of coupled line application in the design of a passive components such couplers and filters. Approach developed and initially aimed for the analysis of single layer IDGs can be easily applied on the multilayer IDG structure. Knowing that multilayered structure has wider monomode range [3], the design of IDG circuits with monomode operation over very wide frequency range becomes reality.

The design procedures for the multi-hole IDG coupler was developed in this thesis, but other coupler types also need investigation. There may be no strong need for non-symmetrical IDG coupler design because of the broadness that can be achieved by other means. Brunch line couplers are desirable for both broad-band and narrow-band applications and for the sake of simplicity. For accurate branch line coupler design the characterization of step and T junction discontinuity is needed.

The filter design utilizing coupled IDG lines is simply an extension of work being done on the coupler design side. The characterization for short circuit termination of IDG line section is desired for the parallel line filter design. The investigation of IDG type resonators will give the necessary base for development of IDG cavity filters.

The metal waveguide to IDG transition analysis ought to provide a good knowledge database which then can be used in the design of an efficient launcher. A good performance metal wave guide-IDG launcher is highly desirable in order to help IDG finds its way for practical

applications.

Integration of active elements, such as diodes into the IDG line allows devices as switches, mixers and oscillator to be made in IDG technology.

Multi-hole IDG coupling theory lends itself for design of IDG launchers, antenna feeders and by controlling hole aperture status with diode placed in the hole, various kinds of electrically adjustable passive and active IDG devices could be produced.

Summarized list of possible IDG development:

- extension of the developed approach to include analysis of multilayer coupled IDGs and probably metal strip loaded IDG structures
- development of effective metal waveguide-to-IDG launcher and antenna feeders utilizing multihole coupled IDG structures
- characterization of IDG resonator and its application to the design of cavity filters and parallel resonator filters.
- characterization of step and T junction type discontinuity for application to the branch line couplers and development of ladder type matching networks and filters.
- integration of diodes into IDG and its use for the purpose of mixer, switch and oscillator design or controlling coupling level or antenna radiation pattern.

7.3 Concluding Remarks

After a recent reduction in defense spending the research into dielectric guides suffers a lack of funding. The present microwave systems use frequency range well under 100GHz where conventional transmission structures based on metal strips such as micro-strip, strip-line and fin-line have undoubtable advantages over dielectric guides.

Dielectric guide structures when loaded with metal strips give new dimension to the microwave circuit design and their system application. In order to make efficient use of such

structures, good knowledge of dielectric guides on their own is needed. The IDG is a more practical variant of image guide, and might have a leading role in this development. The excellency of this approach already has been proven on the antenna designs [4, 5, 6].

The work concerning coupled IDG lines and presented in this thesis, will find its way to the practical applications quite easily. The broadband multihole IDG couplers exhibit easily obtained broadness which exceeds that one of any other previously reported dielectric guide based coupler. This just proves the need for continuous research into possible IDG applications.

References

[1] T. Rozzi and S. Hedges

Rigorous Analysis and Network Modeling of the Inset Dielectric Guide

IEEE Trans. Microwave Theory Tech., Vol. MTT-35 pp823-833, Sept.1987

[2] S. Hedges and T. Rozzi

The Loss Analysis of Inset Dielectric Guide Including Bending Loss and a Comparison with Image Line

Paper P4.5, 17th European Microwave Conference, Rome, Sept. 1987

[3] T. Rozzi, S. R. Pennock and N. Izzat

Bandwidth Control in Multilayer Inset Dielectric Guide

Paper P1.19, 20th European Microwave Conference, Budapest, Sept. 1990

[4] T. Rozzi and L. Ma

Mode Completeness, Normalization and Green's Function of the Inset Dielectric Guide

IEEE Trans. Microwave Theory Tech., Vol.MTT-36, pp.542-551, March 1988

[5] T. Rozzi and L. Ma

An Efficient Mode Launcher for Arrays of Longitudinal Dipoles in IDG

MTT-S Digest 1990, Paper MM6 pp.1243-1246

[6] L. Ma, S. Pennock and T. Rozzi

Design of Multiple Array Flat Millimetric Antennas in IDG

Paper B5,5, 21st European Microwave Conference, Stuttgart, Sept. 1991

Appendix A

Forward and Backward Coupling

Two coupled symmetric lines are shown in Fig.A.1. If such structure is analysed in terms of even and odd modes than chain matrix equation can be written as

$$\begin{vmatrix} V_{1e,o} \\ I_{1e,o} \end{vmatrix} = \begin{vmatrix} \cos\theta_{e,o} & jZ_{e,o}\sin\theta_{e,o} \\ \frac{j}{Z_{e,o}}\sin\theta_{e,o} & \cos\theta_{e,o} \end{vmatrix} \cdot \begin{vmatrix} V_{4e,o} \\ I_{4e,o} \end{vmatrix} \tag{A.1}$$

The corresponding reflection and transmission coefficients for even and odd mode are defined

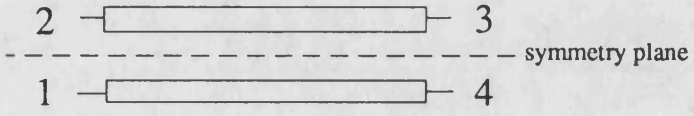

Figure A.1: Symmetric Coupled Lines

as

$$\begin{aligned} \Gamma_{e,o} &= \jmath \frac{\left[\frac{Z_{e,o}}{Z_c} - \frac{Z_c}{Z_{e,o}}\right] \sin\theta_{e,o}}{\Sigma_{e,o}} \\ T_{e,o} &= \frac{2}{\Sigma_{e,o}} \end{aligned} \tag{A.2}$$

where

$$\Sigma_{e,o} = 2\cos\theta_{e,o} + \jmath\left[\frac{Z_{e,o}}{Z_c} + \frac{Z_c}{Z_{e,o}}\right]\sin\theta_{e,o} \tag{A.3}$$

For the unit incident wave at port 1, the amplitudes of scattered waves coming out of ports are given as

$$\begin{aligned} b_1 &= \frac{1}{2}(\Gamma_e + \Gamma_o) \\ b_2 &= \frac{1}{2}(\Gamma_e - \Gamma_o) \\ b_3 &= \frac{1}{2}(T_e - T_o) \\ b_4 &= \frac{1}{2}(T_e + T_o) \end{aligned} \tag{A.4}$$

- If we assume that characteristic impedances of even and odd modes are identical and equal to the characteristic impedance, then above equations get the simple form:

$$\begin{aligned} b_1 &= 0 \qquad\qquad b_2 = 0 \\ b_3 &= \jmath \sin\frac{\theta_e - \theta_o}{2} = \jmath \sin c\theta \\ b_4 &= \cos\frac{\theta_e - \theta_o}{2} = \cos c\theta \end{aligned} \tag{A.5}$$

A coupler having the parameters that meets previously stated assumption, is ideally matched and has perfect isolation. At the same time such a coupler belongs to the family of forward couplers. The above model fits an ideal IDG coupler behavior too.

- For the case when phase constants for even and odd mode are equal, i.e. $\theta_e = \theta_o = \theta$ and in addition $Z_c = \sqrt{Z_e Z_o}$ is satisfied, the expressions for scattered waves get a form:

$$\begin{aligned} b_1 &= 0 \\ b_2 &= \frac{\jmath\left[\sqrt{Z_e/Z_o} - \sqrt{Z_o/Z_e}\right]\sin\theta}{2\cos\theta + \jmath\left[\sqrt{Z_e/Z_o} + \sqrt{Z_o/Z_e}\right]} \\ b_3 &= 0 \\ b_4 &= \frac{2}{2\cos\theta + \jmath\left[\sqrt{Z_e/Z_o} + \sqrt{Z_o/Z_e}\right]} \end{aligned} \tag{A.6}$$

  The coupled port is number 2 in Fig.A.1 which puts this coupler in the family of backward couplers. The backward coupling behavior is common for TEM line couplers.

Both couplers are perfectly matched and isolated and phases of through and coupled port are in quadrature.

Appendix B

LSM Polarisation

B.1 Field Description

When IDG geometry is one of shallow type, then the hybrid modes EH_{mn} become predominant and the field distribution of these modes can be successfully approximated by the LSM polarization. This polarization gives five components field description rather than full six field representation, omitting the H_y component from the six field component model. Analysis of shallow IDG structures under LSM polarization is performed on same manner as it was done for the LSE polarization case, and here only the field components and admittance operator expressions are given for each of the three regions.

B.1.1 Region: quarter open space

Odd mode

The scalar mode function is

$$\Phi_\rho(x,z) = \sqrt{\frac{2}{\pi}}\sin(k_{x\rho}x)\,\frac{1}{\sqrt{2\pi}}\exp(-\jmath\beta z) \tag{B.1}$$

when replaced in (3.11)-(3.19) together with

$$\begin{aligned} V(y,\rho) &= V_\rho \sqrt{\frac{2}{\pi}} \sin(\rho y) \\ I(y,\rho) &= I_\rho \sqrt{\frac{2}{\pi}} \cos(\rho y) \end{aligned} \tag{B.2}$$

gives the field components

$$E_x = -\int_0^\infty d\rho\, V_\rho(\rho) \frac{k_{x\rho}}{\sqrt{\beta_o^2 + k_{x\rho}^2}} \sqrt{\frac{2}{\pi}} \cos(k_{x\rho} x) \sqrt{\frac{2}{\pi}} \cos(\rho y) \tag{B.3}$$

$$E_z = \int_0^\infty d\rho\, V_\rho(\rho) \frac{\jmath\beta_o}{\sqrt{\beta_o^2 + k_{x\rho}^2}} \sqrt{\frac{2}{\pi}} \sin(k_{x\rho} x) \sqrt{\frac{2}{\pi}} \sin(\rho y)$$

$$E_y = \frac{1}{\jmath\omega\epsilon} \int_0^\infty d\rho\, I_\rho \sqrt{k_{x\rho}^2 + \beta_o^2} \sqrt{\frac{2}{\pi}} \sin(k_{x\rho} x) \sqrt{\frac{2}{\pi}} \cos(\rho y)$$

$$H_x = \int_0^\infty d\rho\, I_\rho(\rho) \frac{\jmath\beta_o}{\sqrt{\beta_o^2 + k_{x\rho}^2}} \sqrt{\frac{2}{\pi}} \sin(k_{x\rho} x) \sqrt{\frac{2}{\pi}} \cos(\rho y)$$

$$H_z = \int_0^\infty d\rho\, I_\rho(\rho) \frac{k_{x\rho}}{\sqrt{\beta_o^2 + k_{x\rho}^2}} \sqrt{\frac{2}{\pi}} \cos(k_{x\rho} x) \sqrt{\frac{2}{\pi}} \cos(\rho y) \tag{B.4}$$

$$H_y = 0$$

utilizing the same boundary conditions as given for the LSE case, see page 41. The integral admittance operator linking transverse E_y and H_z components is defined as

$$E_y(y) = \int_0^\infty dy'\, Y(y,y')\, H_z(y') \tag{B.5}$$

Using orthogonality property of mode functions (3.18) an expression for current amplitude I_ρ is found as

$$I_\rho(\rho) = \jmath\omega\epsilon \int_0^\infty dy' \frac{1}{\sqrt{k_{x\rho}^2 + \beta_o^2}} \sqrt{\frac{\pi}{2}} \frac{1}{\sin(k_{x\rho}\frac{d}{2})} \sqrt{\frac{2}{\pi}} \cos(\rho y')\, E_y(y') \tag{B.6}$$

Subsistuting this into (B.4) gives

$$H_z(x = d/2, y) = \int_0^\infty dy' \int_0^\infty d\rho \, y_{1,o} \sqrt{\frac{2}{\pi}} \cos(\rho y) \sqrt{\frac{2}{\pi}} \cos(\rho y') \, E_y(x = d/2, y') \qquad \text{(B.7)}$$

from where the kernel is separated as the admittance operator

$$\begin{aligned} \mathcal{Y}_{1,o} &= j\omega\epsilon \int_0^\rho y_{1,o} \sqrt{\frac{2}{\pi}} \cos(\rho y) \sqrt{\frac{2}{\pi}} \cos(\rho y') \qquad \text{(B.8)} \\ y_{1,o} &= j\omega\epsilon \frac{k_{x\rho}}{k_{x\rho}^2 + \beta_o^2} \cot(k_{x\rho} \frac{d}{2}) \end{aligned}$$

Even mode

Without repeating derivation for even symmetry field components of a quarter open space region, only the expression for the admittance operator is given as:

$$\begin{aligned} \mathcal{Y}_{1,e} &= j\omega\epsilon \int_0^\rho y_{1,e} \sqrt{\frac{2}{\pi}} \cos(\rho y) \sqrt{\frac{2}{\pi}} \cos(\rho y') \qquad \text{(B.9)} \\ y_{1,e} &= -j\omega\epsilon \frac{k_{x\rho}}{k_{x\rho}^2 + \beta_e^2} \tan(k_{x\rho} \frac{d}{2}) \end{aligned}$$

In order to check validity of this expression, the fact that Y_e must be equal to Y_o when d goes to infinity, i.e.

$$\lim_{d \to \infty} \mathcal{Y}_e = \lim_{d \to \infty} \mathcal{Y}_o \qquad \text{(B.10)}$$

has been used to prove validity of admittance operators.

The equation for wavenumber conservation, in the case of a bounded modes in a lossless media $\beta \geq k_0$ gives always purely imaginary values for $k_{x\rho}$. The trigonometric functions are transformed to hyperbolic form making both operator equations (B.8) and (B.9) to be of the same sign. As tanh and coth get unity value when their argument tends to infinity, Y_o and Y_e become equal, and the identity (B.10) is satisfied.

B.1.2 Region II: a grounded slab guide

The admittance operator for TM modes of grounded slab guide, by analogy with (3.36) can be described as

$$Y_{sg} = \sum_{\nu=1}^{N_{sw}} y_\nu \, \Phi_\nu(y) \, \Phi_\nu(y') + \int_0^\infty d\rho \, y_\rho \, \Phi_\rho(\rho, y) \, \Phi_\rho(\rho, y') \tag{B.11}$$

with

$$y_\nu = \omega\epsilon \frac{k_{x\nu}}{k_{x\nu}^2 + \beta^2} \qquad\qquad y_\rho = \omega\epsilon \frac{k_{x\rho}}{k_{x\rho}^2 + \beta^2}$$

The scalar functions for TM modes of grounded dielectric slab in air region are formulated as [4]:

- discrete mode:

$$\begin{aligned} \Phi_\nu(y) &= A'_\nu e^{-\gamma'_\nu y} \qquad y \geq 0 \\ \text{with} \qquad A'_\nu &= \sqrt{\frac{2\epsilon_r}{h + \epsilon_r/\gamma'_k \left[1 + \gamma'^2_k/q'^2 \left(1 + \epsilon_r \gamma'_k h\right)\right]}} \\ \text{and} \qquad 0 &= \gamma'_\nu - \frac{q'_\nu}{\epsilon_r} \tan(q'_\nu h) \end{aligned} \tag{B.12}$$

- continuous mode:

$$\begin{aligned} \Phi_\rho(y, \rho) &= \sqrt{\frac{2}{\pi}} \cos(\rho y + \alpha') \qquad y \geq 0 \\ \tan\alpha' &= \frac{k_\rho}{\rho\epsilon_r} \tan(k_\rho h) \end{aligned} \tag{B.13}$$

To take into account of multiple reflection occurring between the two discontinuity steps, region II was modeled as a Π two-port network. The network representation of the model based on integral admittance operators is presented in Fig.3.3. According to eqn(B.11) complete

expressions for integral operators are given by:

$$Y_{11} = -\sum_{\nu=1}^{N_{sw}} y_\nu \tan(k_{x\nu}a)\,\Phi_\nu(y)\,\Phi_\nu(y') - \int_0^\infty d\rho\, y_\rho \tan(k_{x\rho}a)\,\Phi_\rho(\rho,y)\,\Phi_\rho(\rho,y')$$

$$Y_{12} = -\sum_{\nu=1}^{N_{sw}} y_\nu \csc(k_{x\nu}a)\,\Phi_\nu(y)\,\Phi_\nu(y') - \int_0^\infty d\rho\, y_\rho \csc(k_{x\rho}a)\,\Phi_\rho(\rho,y)\,\Phi_\rho(\rho,y')$$

with $y_\nu = \jmath\omega\epsilon\frac{k_{x\nu}}{k_{x\nu}^2+\beta^2}$ $y_\rho = \jmath\omega\epsilon\frac{k_{x\rho}}{k_{x\rho}^2+\beta^2}$ The values for attenuation constant γ'_ν are obtainable as solutions of transcendental equation

$$q_\nu'^2\left[\frac{\epsilon_r-1}{\epsilon_r}+\frac{1}{\epsilon_r\cos^2(q'_\nu h)}\right] = (\epsilon_r-1)\,k_0^2 \tag{B.14}$$

As the cut-off frequency for TM waves in grounded slab dielectric guide is equal to zero, at least one valid solution of above equation will be avaliable above zero frequency. The graphic representation of eqn.(B.14) is depicted in Fig.B.1.

B.1.3 Region III: a half open space

The scalar mode function used for the evaluation of half open space field components under LSM polarization is given by:

$$\Phi(x,z) = \frac{1}{\sqrt{2\pi}}\exp\jmath k_x x \frac{1}{\sqrt{2\pi}}\exp\jmath\beta z \tag{B.15}$$

Subsistution of the above equation into (3.11) and (3.19) together with

$$V(y,\rho) = V_\rho \sin(\rho y)$$

$$I(y,\rho) = I_\rho \cos(\rho y)$$

gives the field description consisting of five components:

$$
\begin{aligned}
E_x &= -\int_0^\infty d\rho\, V_\rho(\rho)\, \frac{\jmath k_{x\rho}}{\sqrt{k_{x\rho}^2+\beta_{e,o}^2}}\, \frac{1}{\sqrt{2\pi}} \exp(-\jmath k_x x)\, \sqrt{\frac{2}{\pi}} \sin(\rho y) \qquad \text{(B.16)}\\
E_y &= \frac{1}{\jmath\omega\epsilon} \int_0^\infty d\rho\, I_\rho(\rho)\, \sqrt{k_{x\rho}^2+\beta_{e,o}^2}\, \frac{1}{\sqrt{2\pi}} \exp(-\jmath k_x x)\, \sqrt{\frac{2}{\pi}} \cos(\rho y)\\
E_z &= \int_0^\infty d\rho\, V_\rho(\rho)\, \frac{\jmath \beta_{e,o}}{\sqrt{k_{x\rho}^2+\beta_{e,o}^2}}\, \frac{1}{\sqrt{2\pi}} \exp(-\jmath k_x x)\, \sqrt{\frac{2}{\pi}} \sin(\rho y)\\
H_x &= \int_0^\infty d\rho\, I_\rho(\rho)\, \frac{\jmath \beta_{e,o}}{\sqrt{k_{x\rho}^2+\beta_{e,o}^2}}\, \frac{1}{\sqrt{2\pi}} \exp(-\jmath k_x x)\, \sqrt{\frac{2}{\pi}} \cos(\rho y)\\
H_y &= 0\\
H_z &= -\int_0^\infty d\rho\, I_\rho(\rho)\, \frac{\jmath k_{x\rho}}{\sqrt{k_{x\rho}^2+\beta_{e,o}^2}}\, \frac{1}{\sqrt{2\pi}} \exp(-\jmath k_x x)\, \sqrt{\frac{2}{\pi}} \cos(\rho y)
\end{aligned}
$$

The admittance operator relating transverse electric field E_y to transverse magnetic field H_z at the second discontinuity plane $x = 0$, is found as:

$$
\begin{aligned}
\mathcal{Y}_3 &= \int_0^\infty d\rho\, y_{3\rho} \sqrt{\frac{2}{\pi}} \cos(\rho y) \sqrt{\frac{2}{\pi}} \cos(\rho y') \qquad \text{(B.17)}\\
\text{with} \qquad y_{3\rho} &= \omega\epsilon \frac{k_{x\rho}}{k_{x\rho}^2+\beta_{e,o}^2}
\end{aligned}
$$

This operator equation tends to be equal to the $\mathcal{Y}_{1,e}$ and $\mathcal{Y}_{1,o}$ given by (B.9) and (B.8), when $d \to \infty$. And indeed

$$
\lim_{d\to\infty} \mathcal{Y}_{1,e} = \lim_{d\to\infty} \mathcal{Y}_{1,o} = \mathcal{Y}_3 \qquad \text{(B.18)}
$$

All admittance operators appearing in TRD dispersion equation (3.10) have been evaluated and make the solution possible for the case of LSM^y polarization applied on symmetrically coupled IDG structure.

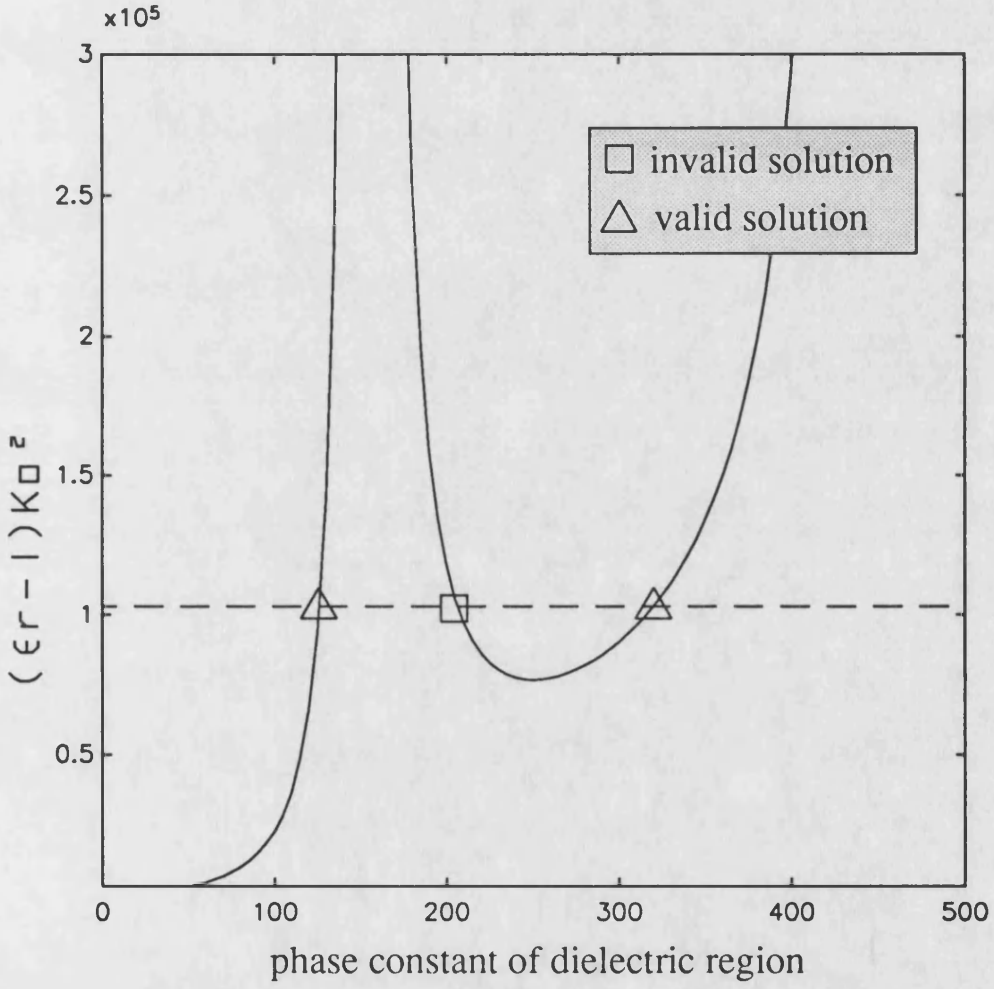

Figure B.1: Graphical representation for solutions of transcendental equation (B.14). The solutions are for LSM modes of d=10.16mm thick grounded guide with $\epsilon_r = 2.08$ at f=15 GHz.

Appendix C

Transformer Coefficients

The coefficient $P_{m\rho}$ has been defined as

$$P_{m\rho} = \int_0^\infty \frac{1}{N_{m-1}} \frac{1}{\sqrt{y_o a}} \left(\frac{y}{y_o a}\right)^{-1/3} e^{-y/(y_o a)} L_{m-1}^{-1/3} \sqrt{\frac{2}{\pi}} \left\{ \begin{array}{l} \sin(\rho y) \\ \cos(\rho y) \end{array} \right\} dy \qquad \text{(C.1)}$$

$$= \int_0^\infty \frac{1}{N_{m-1}} \sqrt{\frac{a}{y_o}} \left(\frac{y}{y_o a}\right)^{-1/3} e^{-y/(y_o a)} L_{m-1}^{-1/3} \sqrt{\frac{2}{\pi}} \left\{ \begin{array}{l} \sin(\rho a y/a) \\ \cos(\rho a y/a) \end{array} \right\} d(y/a)$$

where upper terms in brackets reefer to LSE and lower for LSM polarisation.

From [3] the integrals are found to be:

$$\int_0^\infty x^\lambda e^{-cx} \left\{ \begin{array}{l} \sin bx \\ \cos bx \end{array} \right\} L_n^\lambda(cx) dx = \qquad \text{(C.2)}$$

$$e^{\pi \jmath (n+\delta)/2} \frac{\Gamma(\lambda+n+1)}{2(n!)} b^n \left[(c-\jmath b)^{-\lambda-n-1} + (-1)^{n+\delta}(c+\jmath b)^{-\lambda-n-1}\right]$$

$$\delta = \left\{ \begin{array}{l} 1 \\ 0 \end{array} \right\} \qquad [b, \Re c > 0; \Re\lambda > -1-\delta] \qquad \text{(C.3)}$$

which give, after applying some complex number identities:

$$P_{m\rho} = \frac{1}{N_{m-1}}\sqrt{\frac{2a}{\pi y_o}}\frac{\Gamma(m-1/3)}{(m-1)!}\frac{(\rho y_o a)^{m-1}}{[1+(\rho y_o a)^2]^{(2m-1)/2}} \times \left\{ \begin{array}{c} \sin \\ \cos \end{array} \right\} [(m-1)\pi/2 + (m-1/3)arctg(\rho y_o a)] \quad \text{(C.4)}$$

Same procedure as above is employed in order to get expressions for transformer coefficients of continuum mode of region II.

$$R_{m\rho} = \frac{1}{N_{m-1}}\sqrt{\frac{2a}{\pi y_o}}\frac{\Gamma(m-1/3)}{(m-1)!}\frac{(\rho y_o a)^{m-1}}{[1+(\rho y_o a)^2]^{(2m-1)/2}} \times \left\{ \begin{array}{l} \sin[\alpha'' + (m-1)\pi/2 + (m-1/3)arctg(\rho y_o a)] \\ \cos[\alpha' + (m-1)\pi/2 + (m-1/3)arctg(\rho y_o a)] \end{array} \right\} \quad \text{(C.5)}$$

In order to get the transformer coefficients for the discrete mode of region II, integral given by equations (4.13) had to be solved. From [2] the solution is found as

$$\int_0^\infty x^\lambda e^{-px} L_n^\lambda(cx)dx = \frac{\Gamma(\lambda+n+1)(p-c)^n}{n!p^{\lambda+n+1}} \quad \text{(C.6)}$$

with conditions $[\Re p > 0; \Re\lambda > -1]$ which are satisfied in our case and give us the expression:

$$R_{mk} = \frac{1}{N_{m-1}}\sqrt{\frac{a}{y_o}} \left\{ \begin{array}{c} A_s'' \\ A_s' \end{array} \right\} \frac{\Gamma(m-1/3)}{(m-1)!} \frac{\left(\left\{ \begin{array}{c} \gamma_k'' \\ \gamma_k' \end{array} \right\} y_o a \right)^{m-1}}{(1+\left\{ \begin{array}{c} \gamma_k'' \\ \gamma_k' \end{array} \right\} y_o a)^{m-1/3}} \quad \text{(C.7)}$$

References

[1] M. Abramovitz and I. Stegun

Handbook of Mathematical Functions

National Bureau of Standards, 1968, pp.771-803

[2] A. Apelblat

Table of Definite and Infinite Integrals

Elsevier Scientific Publishing Company, Amsterdam 1983

[3] I. S. Gradshteyn and I. M. Ryshik

Table of Integrals, Series and Products

Academic Press, New York 1965

[4] T. Rozzi and J. S. Kot

The Complete Spectrum of Image Line

IEEE Trans. Microwave Theory Tech., Vol MTT-37 pp868-876 May 1989

Chapter 5

Numerical and Measured Results

This chapter presents results obtained from the numerically solved dispersion equation and their comparison with available measured data. The results are gathered for both deep and shallow slot IDG geometry, and also for single and coupled IDG structures.
The dispersion equation capable of modeling deep or shallow IDG in coupled or in single configuration is derived in chapter 4 and given with (4.6). The solutions of this equation are found by searching for such values of $\beta_{e,o}$ that give zero value for determinantal function. The function is calculated for successive values of $\beta_{e,o}$ and when the change of sign occurs an iterative procedure is applied to find root of this non-linear equation. Since the dispersion equation is transcendental equation, same method has to be repeated for every sign change in order to cover all possible solutions.

5.1 Computational Method and Numerical Algorithms

The programs which determine the solutions for the dispersion equation were written in Fortran77 and run on HP9000 series 825 computer under UNIX operating system. The presentation of computational method follows the same chronological order in which it was developed.
First of all, the solutions of transcendental equation (3.44) are needed in order to determine

decay and phase constants for TE modes of grounded slab dielectric guide. The iteration method used to find solutions of this non-linear equation is based on Muller's method of successive bisections and inverse parabolic interpolation, which starts with initial bounds. It is assumed that values of the non-linear function at the initial bounds are of different sign. The graphic representation of the transcendental equation giving solutions for phase constant in dielectric slab under LSE polarization was depicted in Fig. 3.7, and that one representing solutions under LSM polarization was shown in Fig. B.1. The number of valid solutions determines number of propagating bound modes. Beside valid there are invalid solutions too, but these have negative decay constant in the y-direction which is characteristic of physically non-realizable solutions. Such invalid solutions of (3.44) should be ignored. Also, for the case of LSE polarization, a valid solution may not exist for frequencies below the cut-off frequency of TE waves in grounded dielectric slab guide. On other hand at least one solution of (B.14) is always available for LSM polarization since the cut-off frequency for TM modes is equal to zero.

Having solutions for decay and propagation constant of slab guide in air and dielectric region respectively, the scale factors used to improve convergence in the basis function, (4.18), can be found. The optimal values for y_o are obtained through an optimization procedure searching for minimum of the error function defined in chapter 4 and given by (4.24). The optimization routine used is capable of finding a quasi-global function minimum within a defined and constrained volume. A certain number of starting points over such a volume are specified and about 4 iterations are done from each point. The five points which result in the lowest values of the error function are allowed to continue to convergence. The local minimum with the lowest function value is taken to be the global minimum. As the number of starting points is increased, the probability that the minimum found is really the global minimum is increased [1].

After determining scale factors for certain IDG geometry, frequency and type of polarization, transformer coefficients P_ρ, R_ν and R_ρ are due to be evaluated. Beside the evaluation of the Gamma function, the calculation of these coefficients is straightforward, and values for P_ρ,

R_ν and R_ρ are easy numerically obtainable.

Moving further forward, the terms of the discretized impedance matrix have to be evaluated. Real difficulties start with the evaluation of impedance matrix terms for the continuous modes, where good numerical integration procedure becomes necessary. The integrations have to be performed on integrand functions having a singular value at $\rho = k_0$ and therefore only the principal value of the integrals given by (4.7-4.9) can be determined [2]. As the integration space stretches over a semi-infinite range, a procedure transforming semi-infinite integration into two integrals over bounded range is applied [3]. The impedance matrix is often very badly balanced. Many elements of the matrix are large and particular care must be taken in the evaluation of these elements. Numerical integration is based on a routine where the integral is computed as the sum of estimates over suitably chosen subintervals of the given interval of integration. Starting with the interval of integration itself as the first such subinterval, cautious Romberg extrapolation is used to find an acceptable estimate on a given subinterval. If this attempt fails, the subinterval is divided into two subintervals of equal length, and each of them is considered separately [4].

When all terms in the matrix equation are evaluated, the calculation of determinantal function is the next step. For a given frequency the determinant value is scanned over the range of interest ($k_0 \leq \beta_{e,o} \leq \sqrt{\epsilon_r} k_o$). The determinant calculation is based on an algorithm which computes LU decomposition of row wise permutation of the complex matrix. Row equilibration and partial pivoting are used [5]. When a change of sign occurs in the returned value for the determinant then the zero (or pole) lay between two successive values of β, and an iteration procedure is applied to find solution and determine whether the successive values found a zero or pole of the function. The used iteration algorithm is a combination of linear interpolation, inverse quadratic interpolation and bisection. Convergence is usually superlinear [6]. Since the dispersion equation is transcendental, the method of search has to be repeated for all possible solutions.

This computational method is applied for the calculation of both even and odd mode phase constants, enabling dispersion characterization of coupled IDGs.

5.2 Scale Factor

The scale factor y_o was introduced in (4.18) in order to make basis set better fit the unknown field and consequently to improve convergence. An optimization procedure is used to determine optimal values of y_o and the relevant error function was defined in chapter 4.
The parameters that influence the value of the scale factors are permittivity and thickness of dielectric filling, slot height, working frequency, type of polarization and number of basis function used in the field expansion. Tables Tab.5.1 and Tab.5.2 contain optimal values of the scale factor for deep slot IDG under LSE polarization with two types of dielectric filling. The deep slot IDG with specified dimensions and physical parameters is monomode over frequency range exceeding X band. The dimensions of the slot filled with dielectric of higher permittivity are scaled down in order to maintain monomode operation over the same frequency range.
The scale coefficients for shallow slot IDG configuration are given in Tab.5.3 for two type of polarization. The shallow guide with the dimensions given is over moded, and can support both LSE and LSM modes over the specified frequency range. Therefore coefficients for both types of polarization have been evaluated for this type of slot configuration.
As previously stated the scale factor depends on number of function used in the expansion. From the tables it is apparent that dependence on number of functions is significant when only a few functions are used. When four or more basis functions are used the same scale factor can be used regardless of expansion order. From the above observation the conclusion can be drawn that sufficiently good approximation is achieved with at least four basis functions incorporated into the expansion set.

5.3 Mode Classification

The field supported by the IDG structure is hybrid in nature due to presence of the 90° metal edge discontinuity. Such field needs six components for a complete description. The modes in the hybrid representation are designated HE_{mn} or EH_{mn} according to which component

freq GHz	7	8	9	10	11	12	13
N=1	1.12670	.805714	.632422	.523287	.447903	.392486	.349969
N=2	.897430	.641780	.503748	.416816	.356771	.312629	.278763
N=3	.879810	.629179	.493857	.408633	.349766	.306491	.273290
N=4	.877593	.627594	.492613	.407603	.348885	.305719	.272601
N=5	.877287	.627376	.492441	.407462	.348765	.305613	.272507

Table 5.1: Computed values for optimal scale constants under LSE_{01} polarization for deep slot ($10.16 \times 15.24mm$) IDG geometry with PTFE dielectric filling, $\epsilon_r = 2.08$

freq GHz	7	8	9	10	11	12	13
N=1	1.27030	.883860	.683987	.561101	.477504	.416725	.370406
N=2	1.01180	.704028	.544822	.446937	.380349	.331936	.295042
N=3	.991979	.690205	.534125	.438162	.372881	.325420	.289242
N=4	.989479	.688466	.532780	.437058	.371942	.324599	.288520
N=5	.989135	.688227	.532594	.437058	.371813	.324486	.288420

Table 5.2: Computed values for optimal scale constants under LSE_{01} polarization for deep slot ($3.24 \times 4.86mm$) IDG geometry with ceramic dielectric filling, $\epsilon_r = 10.8$

freq GHz	7	8	9	10	11	12	13
			LSM_{11} mode				
N=1	.336340	.273391	.230311	.199149	.175614	.157193	.142420
N=2	.267907	.217766	.183451	.158629	.139883	.125210	.113443
N=3	.262647	.213490	.179849	.155515	.137137	.122752	.111215
N=4	.261985	.212953	.179396	.155123	.136791	.122442	.110935
N=5	.261894	.212878	.179334	.155069	.136744	.122400	.110896
			LSE_{01} mode				
N=1		1.16380	.574296	.386857	.294182	.238730	.201680
N=2		.926990	.457448	.308145	.234326	.190157	.160646
N=3		.908790	.448467	.302095	.229726	.185423	.157491
N=4		.906501	.447337	.301334	.229147	.185953	.157095
N=5		.906186	.447181	.301229	.229067	.185889	.157040

Table 5.3: Computed values for scale constants under LSM and LSE polarization for shallow slot ($22.86 \times 10.16mm$) IDG geometry with PTFE dielectric filling, $\epsilon_r = 2.08$. First column for LSE_{01} mode is empty because cut-off frequency of that mode is above 7 GHz.

	E_x	H_x	E_y	H_y	E_z	H_z	
HE_{mn}	yes	yes	yes	yes	yes	yes	H_y dominates over E_y
LSE_{mn}	yes	yes	no	yes	yes	yes	E_y does not exist
EH_{mn}	yes	yes	yes	yes	yes	yes	E_y dominates over H_y
LSM_{mn}	yes	yes	yes	no	yes	yes	H_y does not exist

Table 5.4: Tabular comparison between hybrid, LSE and LSM modes in terms of the field components existence.

is dominant with respect to y, [7].

As the analysis in this thesis is performed in terms of LSE and LSM polarization having five components field description, the modes will be denoted as LSE_{mn} and LSM_{mn}. It will be shown that hybrid modes are approximated to an excellent extent by the LSE and LSM modes.

For LSE_{mn} modes, the E_y component does not exist and these modes corresponds to HE_{mn} hybrid modes where H_y is the dominant field wrt. y. By analogy LSM_{mn} approximate the EH_{mn} hybrid modes. The pair of indices nm designates the order of functional dependence of a particular mode in the x and y direction respectively.

The similarity between hybrid and approximate modes is compared through the existence of particular field components, as shown in Tab.5.4. As presented in [7], deep slot IDG has HE_{01} as the dominant mode, and the E_y component exist only in the vicinity of the metal edge discontinuities. Therefore, such an IDG structure is amenable for LSE analysis. On other hand shallow slot IDG has EH_{11} as the fundamental mode and the LSM polarization is applicable on this type of structure. Since shallow IDG shows a very narrow monomode range of operation, LSE analysis should be performed in order to characterize HE_{mn} higher order modes of the shallow IDG structure.

The designation for normal degenerate modes of coupled IDGs differs from that of single IDG nomenclature only in appearance of e and o prefixes. These indicate the symmetry of the Hertzian potential in the x direction.

5.4 Convergence Test

The convergence of the applied numerical method is dependent on the choice of basis function. In order to make the basis function fit unknown field better, and consequently improve convergence, the scale parameter y_o was introduced. This factor is a function of frequency, guide cross-section geometry and type of polarization.

The convergence behavior of the adopted numerical approach is shown in Tab.5.5 for several frequencies in the monomode operating range of a single, deep slot IDG line. Comparing with measured values, this test shows that an accuracy of 0.5% is achieved in the calculation of propagation constant using only five basis functions as an expansion set. Such a degree of accuracy does probably exceed the precision to which the permittivity of the IDG filling is known, and so might be thought of as being excessive.

The convergence test for shallow single IDG is depicted in Tab.5.6. The achieved accuracy for LSM_{11} modes using an expansion set consists from five basis function is better than 0.3%.

The properties of coupled IDGs rely on the relatively small difference between the phase constants of the even and odd modes, and five or six basis functions were used as the expansion set in order to achieve desired accuracy and stability.

The discretized impedance operator matrix for coupled lines is not so well balanced as it is case for single IDG. Consequently, convergence is not so steady and oscillatory behavior is noticed. Also convergence stability is noticed to be better for the analysis of coupled IDGs under LSM polarization than for the LSE case. As evaluation of matrix elements include such complex numerical task as estimation of principal value of an integral over a semi-infinite range, the produced numerical integration error together with wavy feature of integrand function make convergence slower and with oscillatory behavior. Also convergence behavior is different for even and odd modes of the same polarization. For instance, even mode under LSE converges slower than the odd mode. This is due to presence of the magnetic wall which makes the elements of the matrix very badly balanced, and greater integration error and instability are introduced. An identical statement is valid for odd modes under LSM polarization.

freq GHz	7	8	9	10	11	12	13
N=3	162.319	193.489	224.563	255.413	285.766	316.061	346.345
N=4	163.544	195.432	227.649	259.871	291.907	323.643	355.129
N=5	163.505	195.860	228.282	260.761	293.185	325.409	357.149
Meas.	160.056	198.088	230.297	262.138	293.914	325.806	357.388

Table 5.5: Convergence test for the LSE_{01} mode propagation constant in a deep slot IDG, and comparison with measured data. The IDG is filled with PTFE and has 10.16 × 15.24mm for the slot dimensions.

freq GHz	8	9	10	11	12	13	14
LSM_{11} mode							
N=3		203.130	240.570	276.533	311.477	345.679	379.313
N=4		203.947	240.565	276.532	311.477	345.676	379.309
N=5		203.128	240.566	276.532	311.473	345.680	379.309
LSE_{01} mode							
N=3	170.603	198.841	236.789	253.048	288.263	320.435	353.305
N=4	170.942	198.465	228.708	260.044	291.538	324.549	352.363
N=5	170.919	199.182	229.694	262.240	289.864	324.552	357.612

Table 5.6: Convergence test for the propagation constants of LSM_{11} and LSE_{01} modes in a shallow slot IDG, and comparison with measured data. The IDG is filled with PTFE and has 22.86 × 10.16mm for the slot dimensions.

5.5 Approximate Calculation of β for Single IDG

A useful approximate procedure is established in order to simplify solutions for phase constant of single IDG. The modes of a single IDG were designated to the LSM_{mn} or LSE_{mn}. Which mode is dominant depends on the geometry of slot used and the operating frequency. The indices mn stands for the order of the functional dependence of a particular mode. If $m\pi/a$ is assumed to be the x directed wave number, and the phase constant in y direction (q_n) is assigned to be the phase constant of a grounded dielectric slab having the same thickness as the dielectric IDG filling, then the propagating constant is calculated simply by

$$\beta = \sqrt{\epsilon_r k_0^2 - \left(\frac{m\pi}{a}\right)^2 - q_n^2} \tag{5.1}$$

Solutions obtained from this equation on deep and shallow IDG geometries over the X band frequency range are presented in Tab.5.7. The difference between the values for β gained by solving full dispersion equation (4.6) and those obtained by approximation (5.1) is negligible for all practical applications. The error is something bigger for frequencies close to cut-off and decrease steadily as frequency is increased. This is believed to be due tighter energy confinement within the dielectric at higher frequencies, where the approximation becomes more accurate.

In order to endorse the above statement, the shallow IDG structure is analysed over Qu frequency band. Two modes, LSM_{11} and LSE_{01} are supported by shallow structure of cross section having 8×3mm and filled with PTFE. The phase constants obtained through approximate and full calculations procedure are represented in Tab.5.8. This data is shown graphically in Fig.5.1.

As the agreement between computed and approximate values is apparent and more than satisfactory, this leads us to the conclusion that the phase constant can be calculated quite accurately through use of approximate equation. If the validity of approximate solution needs to be checked or accuracy enhanced, then a search routine utilizing full numerical procedure is applied in neighborhood of the approximate solution.

freq GHz	7	8	9	10	11	12	13	14
k_0	147.196	168.244	189.252	210.280	231.308	252.336	273.364	
LSE_{01} Modes of Deep Slot IDG								
q_1	135.102	143.174	149.487	154.581	158.791	162.336	165.386	
β_{app}	163.750	195.902	228.367	260.916	293.381	325.711	357.885	
β_{com}	163.728	194.918	227.217	260.387	292.849	325.236	357.388	
LSM_{11} Modes of Shallow Slot IDG								
q_1	109.524	115.311	119.793	123.345	126.222	128.600	130.594	132.301
β_{app}			203.417	240.810	276.741	311.663	345.847	379.465
β_{com}			203.128	240.566	276.532	311.473	345.680	379.309
LSE_{01} Modes of Shallow Slot IDG								
q_1	152.950	172.076	186.463	197.806	207.054	214.762	221.309	226.951
β_{app}		171.033	199.322	229.882	261.564	293.799	326.276	358.831
β_{com}		170.919	199.288	230.038	261.403	293.580	326.023	357.612

Table 5.7: Tabular comparison between data obtained through application of approximate equation (5.1) and that calculated by dispersion equation (4.6). The considered guides have $10.16 \times 15.24mm$ and $22.86 \times 10.16mm$ for deep and shallow slot dimensions,respectively. Dielectric filing is assumed to be PTFE.

freq GHz	25	27	29	30	31	33	35
k_0	525.701	567.757	609.813	630.841	651.869	693.926	735.982
LSM_{11} Modes of Shallow Slot IDG							
q_1	375.792	386.969	396.577	400.903	404.934	412.239	418.675
β_{app}	640.075	703.877	767.749	799.669	831.574	895.308	958.910
β_{com}	641.376	703.324	765.627	796.863	828.158	890.816	953.530
LSE_{01} Modes of Shallow Slot IDG							
q_1	538.169	574.901	605.896	619.726	632.582	655.837	676.339
β_{app}	526.227	574.901	628.671	657.083	686.260	740.338	808.076
β_{com}	526.227	574.665	628.425	656.708	685.783	740.700	807.505

Table 5.8: Tabular comparison between approximate and computed data for phase constant of shallow IDG structure over Qu frequency band. The dimensions of guide cross-section are 8.0×3.0mm and dielectric inset is made from PTFE.

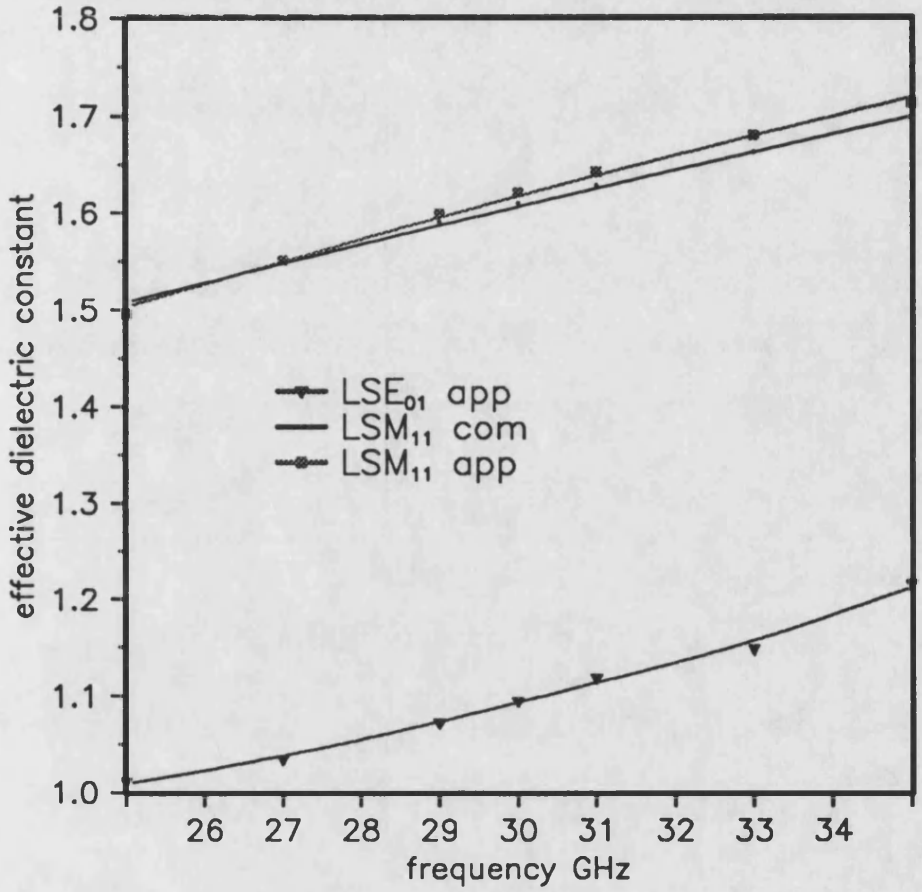

Figure 5.1: Approximate and computed curves for effective dielectric constant of shallow guide, having slot dimensions 8.0×3.0mm. Dielectric filling is PTFE.

5.6 Field Component Patterns

Having solved the dispersion equation (4.6), the amplitude coefficients of the unknown field are obtained by substitution of these solutions into (4.31). The x dependence of the field in region II is modeled by a transmission line having k_x propagation constant with excitation at both ends as is shown in Fig.4.4. Expressions for the H_y and E_z field components in each region are given in chapter 4, and other components , if needed, can be evaluated from the wave equation. The overall field pattern is reached by merging three independent patterns, each corresponding to a different region. Numerical difficulties occur when the field pattern is calculated for modes of the LSE_{on} type. For these modes the propagation constant in x direction is equal to zero, and expressions given by (4.36) should be reformulated for LSE_{on} modes. The proper limit as $k_x \to 0$ must be taken giving:

$$\begin{aligned} H_y(x) &= H_{y1} \lim_{k_x \to 0} \frac{\sin k_x(a-x)}{\sin k_x a} + H_{y2} \lim_{k_x \to 0} \frac{\sin k_x x}{\sin k_x a} \\ &= H_{y1} \frac{a-x}{a} + H_{y2} \frac{x}{a} \end{aligned} \tag{5.2}$$

Field plots in the air region over the single IDG structure are shown in Figs.5.2-5.4. The amplitude coefficients at the two discontinuity planes for both the unknown H_y field in the case of a coupled deep slot IDGs, and for the E_y field in the case of a shallow IDG coupled structure, are presented in Tab.5.9.

The electric field E_z of the LSE_{01} mode for deep and shallow IDG geometries is very low in magnitude, usually three orders smaller than magnitude of H_y. Due this, the contribution of continuous mode to the field magnitude becomes significant and it gives a raise to wavy field pattern. On contrary, the amplitudes of discrete components for LSM_{11} are significantly larger than amplitude of continuous wave and field pattern does not show wavy tendency. The pattern of y directed fields includes spikes close at the 90^o metal corner edges, due to the singularity of these fields at these points.

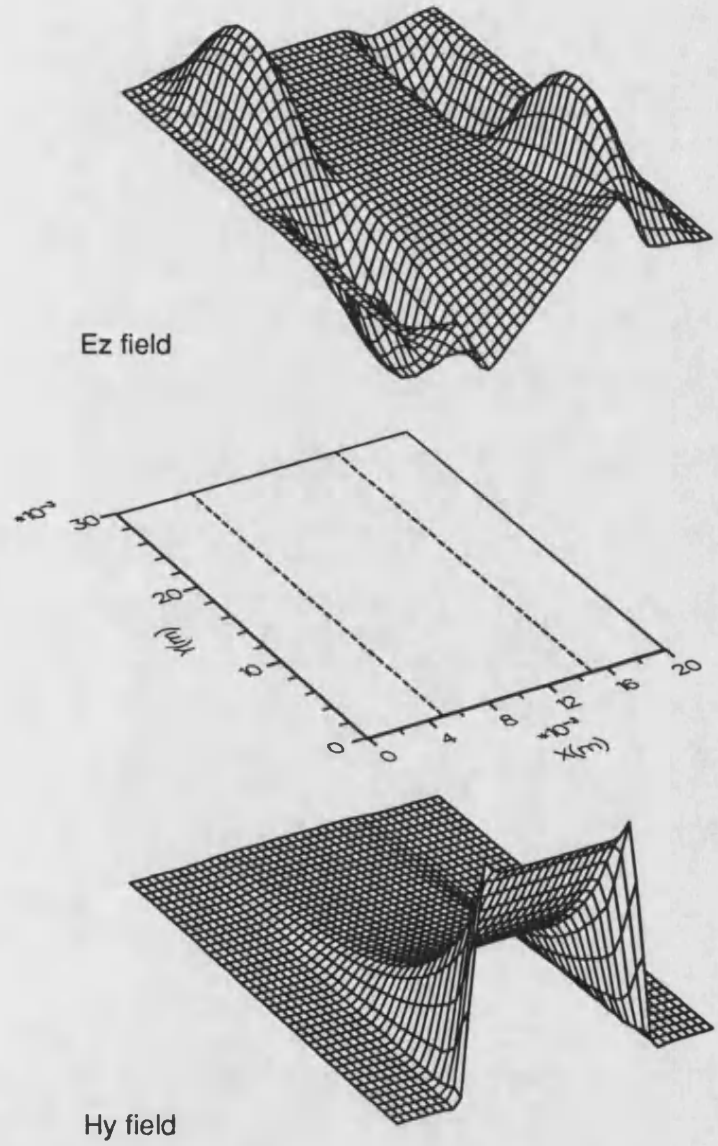

Figure 5.2: Two field components of LSE_{01} mode in air region over deep slot IDG. Slot dimensions are 10.16×15.24 and dielectric inset is made from PTFE. Working frequency is 10GHz. The dashed lines in 2D projection stand for discontinuity planes as shown in Fig. 3.1.

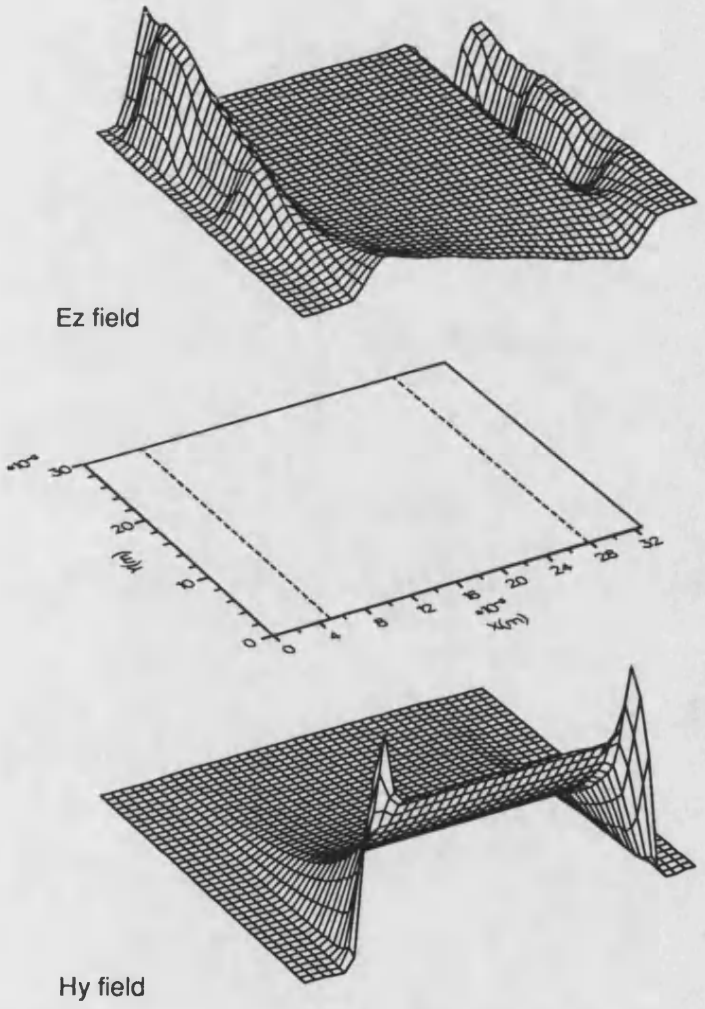

Figure 5.3: Two field components of LSE_{01} mode in air region over shallow slot IDG. Slot dimensions are $22.86 \times 10.16mm$ and dielectric inset is made from PTFE. Working frequency is 12GHz. The dashed lines in 2D projection stand for discontinuity planes as shown in Fig. 3.1.

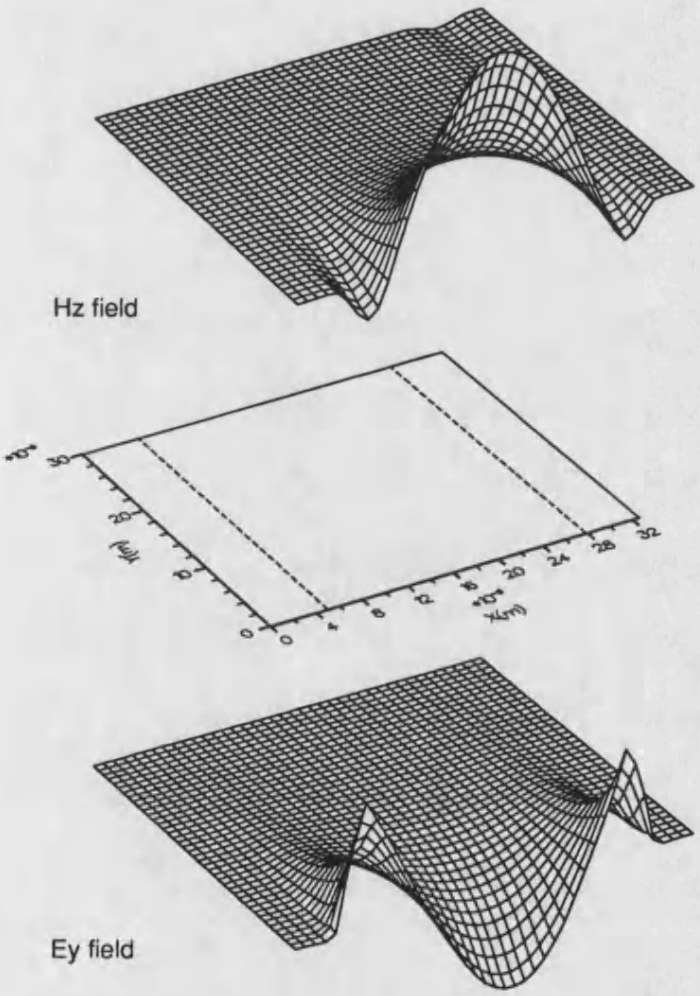

Figure 5.4: Two field components of LSM_{11} mode in air region over deep slot IDG. Slot dimensions are 22.86×10.16 and dielectric inset is made from PTFE. Working frequency is 12GHz. The dashed lines in 2D projection stand for discontinuity planes as shown in Fig. 3.1.

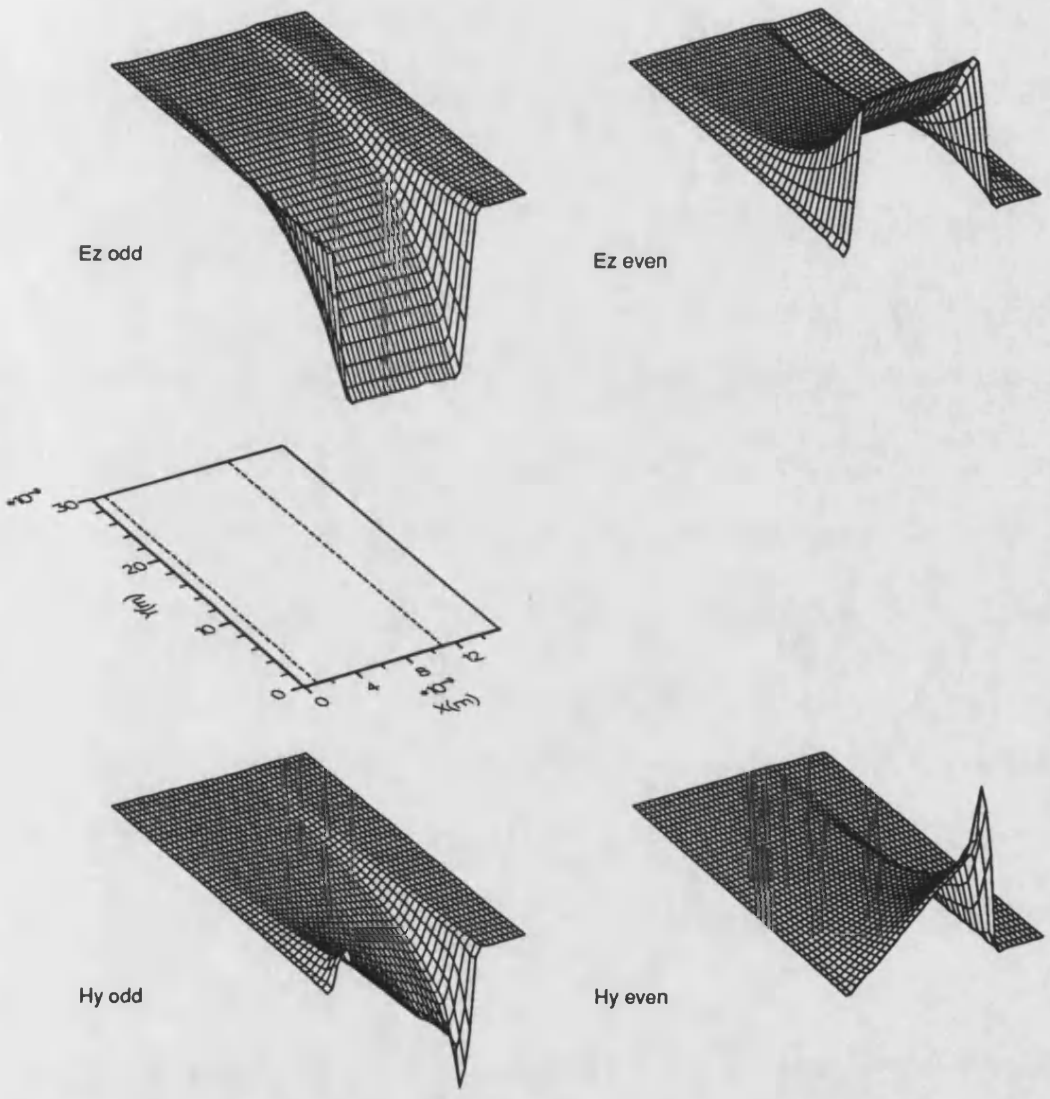

Figure 5.5: Two field components of even and odd symmetry for LSE_{01} mode in air region over deep slot coupled IDGs. Slot dimensions are $10.16 \times 15.24mm$ and dielectric inset is made from PTFE. Guides are separated by $2mm$. Working frequency is 10GHz. The dashed lines in 2D projection stand for discontinuity planes as shown in Fig. 3.1.

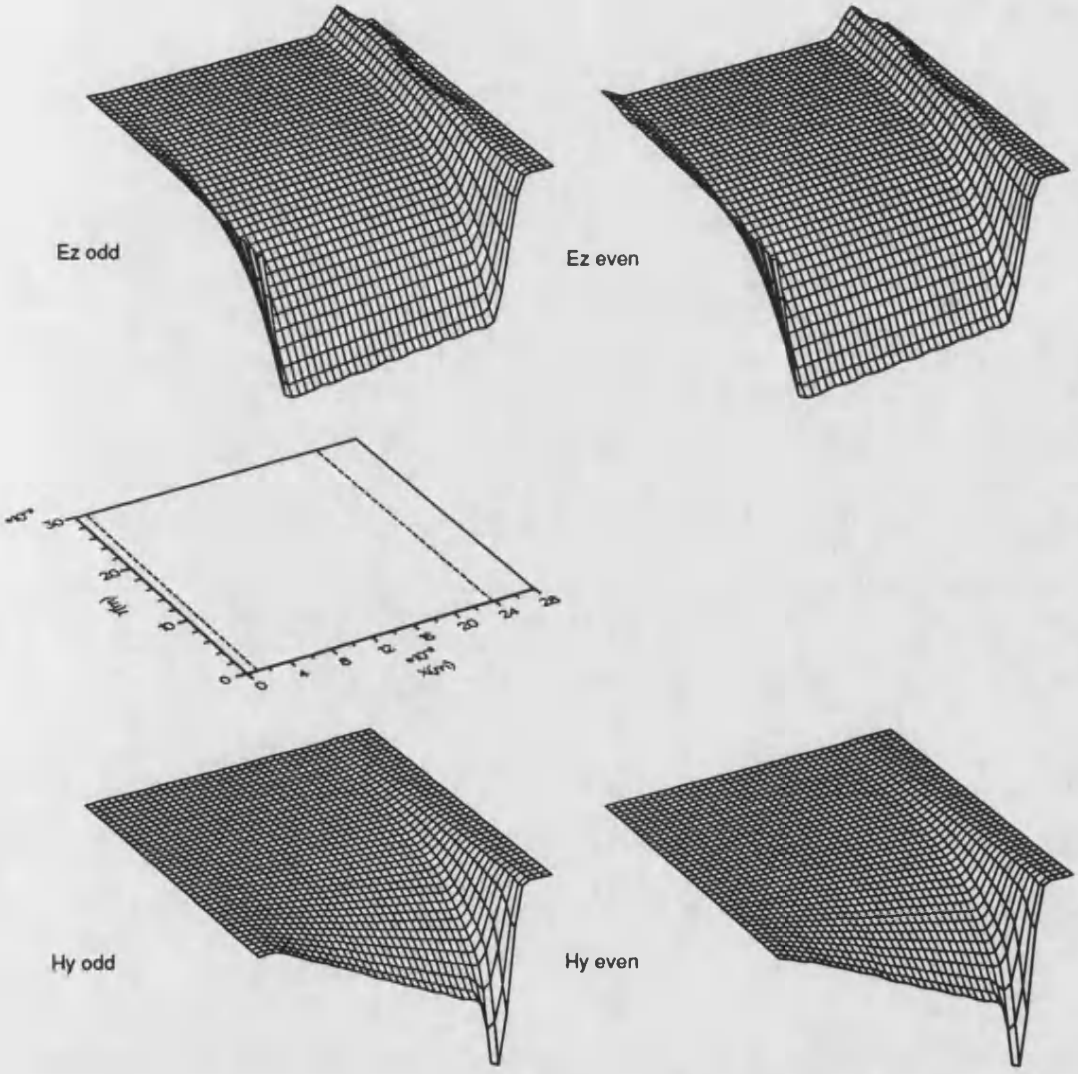

Figure 5.6: Two field components of even and odd symmetry for LSE_{01} mode in air region over shallow slot coupled IDGs. Slot dimensions are $22.86 \times 10.16mm$ and dielectric inset is made from PTFE. Guides are separated by $2mm$. Working frequency is 12GHz. The dashed lines in 2D projection stand for discontinuity planes as shown in Fig. 3.1.

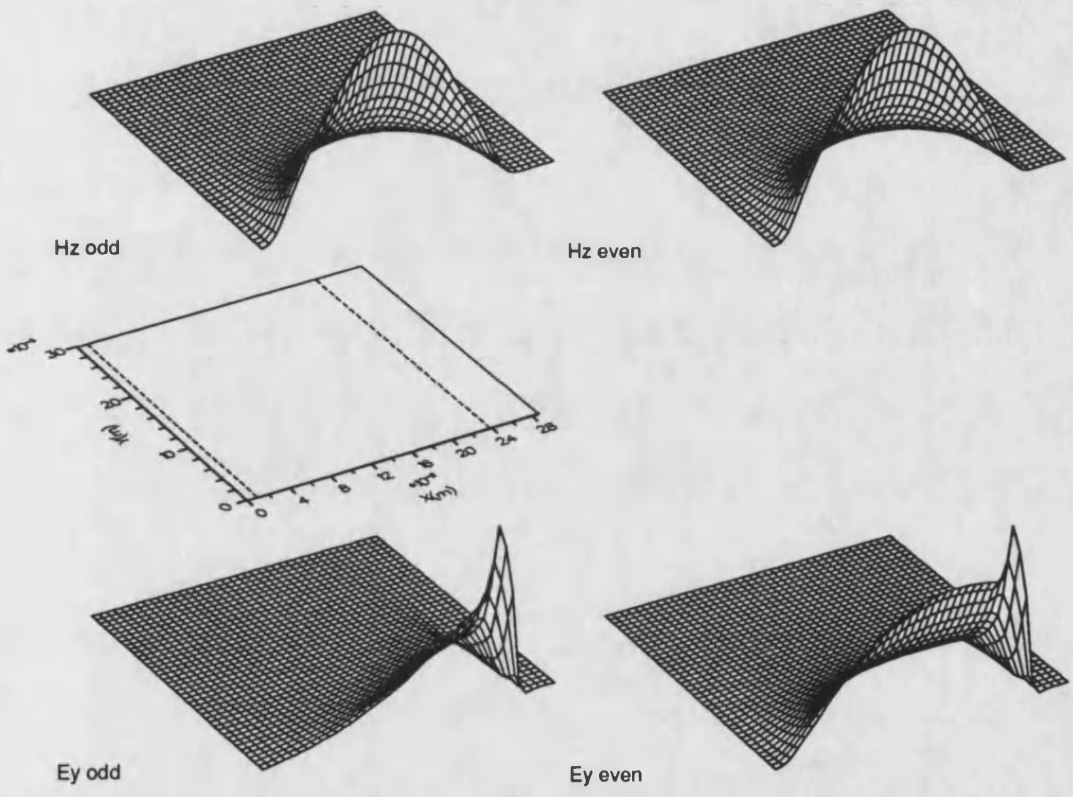

Figure 5.7: Two field components of even and odd symmetry for LSM_{11} mode in air region over shallow slot coupled IDGs. Slot dimensions are $22.86 \times 10.16mm$ and dielectric inset is made from PTFE. Guides are separated by $2mm$. Working frequency is 12GHz. The dashed lines in 2D projection stand for discontinuity planes as shown in Fig. 3.1.

LSE_{01} mode of deep IDG						
odd	X_1	$0.0, -j.13079$	$0.0, -j.96772$	$0.0, -j2.3556$	$0.0, -j2.5522$	$0.0, -j1.0467$
	X_2	$0.0, +j.23885$	$0.0, +j2.7978$	$0.0, +j8.1495$	$0.0, +j11.347$	$0.0, +j6.4532$
even	X_1	$0.0, +j.01732$	$0.0, -j.85008$	$0.0, -j2.7812$	$0.0, -j4.0276$	$0.0, -j1.9709$
	X_2	$0.0, -j.05175$	$0.0, -j18.129$	$0.0, -j65.539$	$0.0, -j105.97$	$0.0, -j67.064$
LSE_{01} mode of shallow IDG						
odd	X_1	$0.0, -j.90726$	$0.0, -j4.5258$	$0.0, -j7.6048$	$0.0, -j4.8248$	$0.0, -j.48541$
	X_2	$0.0, +j17.746$	$0.0, +j104.47$	$0.0, +j223.38$	$0.0, +j228.09$	$0.0, +j93.020$
even	X_1	$0.0, +j1.9487$	$0.0, +j5.5833$	$0.0, +j11.425$	$0.0, +j7.4193$	$0.0, +j2.7445$
	X_2	$0.0, +j147.82$	$0.0, +j899.14$	$0.0, -j1959.5$	$0.0, -j2034.6$	$0.0, -j842.22$
LSM_{11} mode of shallow IDG						
odd	X_1	$0.0, -j.10940$	$0.0, -j.77810$	$0.0, -j2.3513$	$0.0, -j3.5215$	$0.0, -j2.2034$
	X_2	$0.0, -j30.260$	$0.0, -j181.42$	$0.0, -j438.01$	$0.0, -j544.98$	$0.0, -j265.83$
even	X_1	$0.0, +j.37816$	$0.0, +j2.3546$	$0.0, +j5.1446$	$0.0, +j6.0474$	$0.0, +j2.6927$
	X_2	$0.0, -j31.157$	$0.0, -j186.71$	$0.0, -j450.68$	$0.0, -j560.60$	$0.0, -j273.35$

Table 5.9: Amplitude coefficients on two interface planes for LSE_{01} mode in deep and shallow IDG geometry and for LSM_{11} mode of shallow guide. The IDG is filled with PTFE and 10.16 × 15.24mm are dimensions of a deep slot while 22.86 × 10.16mm are dimensions for a shallow slot.

5.7 Single IDG Characterization

As was previously mentioned, the same dispersion equation derived for purpose of analysing the coupled symmetric IDG can be used for single IDG characterization by a simple modification. All that is necessary is to replace the integral impedance/admittance operator representing region I by an operator relating the transverse field components in region III. However, the behavior of the single IDG was investigated before [7], and those results will be compared with data obtained through the approach presented in this thesis.

Two basic slot configurations were considered, deep and shallow slot IDGs. While deep slot mode properties were well known, the modes of shallow slot IDG had received less attention and have been investigated here. The shallow slot IDG is very easily overmoded, and this is endorsed by numerical computation and measured data. Both types of analysis, concerning models for LSE and LSM polarization, were employed in order to detect and characterize all possible modes of the shallow IDG geometry.

5.7.1 Deep Slot IDG

By deep slot IDG we understand such geometry where the height is greater than the slot width. The basic mode of such guide is assigned to the LSE_{01} and the guide exhibits monomode behavior over a considerable frequency range. The IDG having slot dimensions $10.16 \times 15.24mm$ and filled with PTFE possess a wider monomode bandwidth range than X band metal-waveguide. The dispersion characteristic of such a guide is presented in Fig.5.8 along with experimentally obtained data. The method used for phase constant measurement will be described in section 9 of this chapter.

The two data sets are in good agreement. For frequencies close to cut-off the greater difference between two data sets is caused by using a five field LSE polarization rather than a full six components hybrid description. On the same figure numerical data obtained as a result of the application of hybrid modes [7] is also presented. Very small differences between our set and that obtained for hybrid modes shows excellent compatibility between HE_{mn} and LSE_{mn} modes for this geometry.

The field pattern of the H_y and E_z components in air region over completely filled deep slot IDG is presented in Fig.5.2. As was shown in [7], the E_z component is very weak and exists only in the vicinity of metal edges. The continuous field component is of same magnitude as discrete field component and wavy field pattern is obtained for z directed electric field component of deep slotted IDG. The magnitude of discrete H_y field is two orders bigger than that of continuous wave, and due this the field is steady and has no wavy pattern. Two spikes which can be noticed close to the metal edges are caused by field singularity at these points.

5.7.2 Shallow Slot IDG

By shallow IDG geometry is called that one, where width of the slot is greater than its height. The investigated shallow IDG had slot dimensions $22.86 \times 10.16mm$ that were chosen for the sake of compatibility with X-band rectangular metal waveguide, from which the IDG can be efficiently feed by the use of a dielectric taper within a metal waveguide transition section.

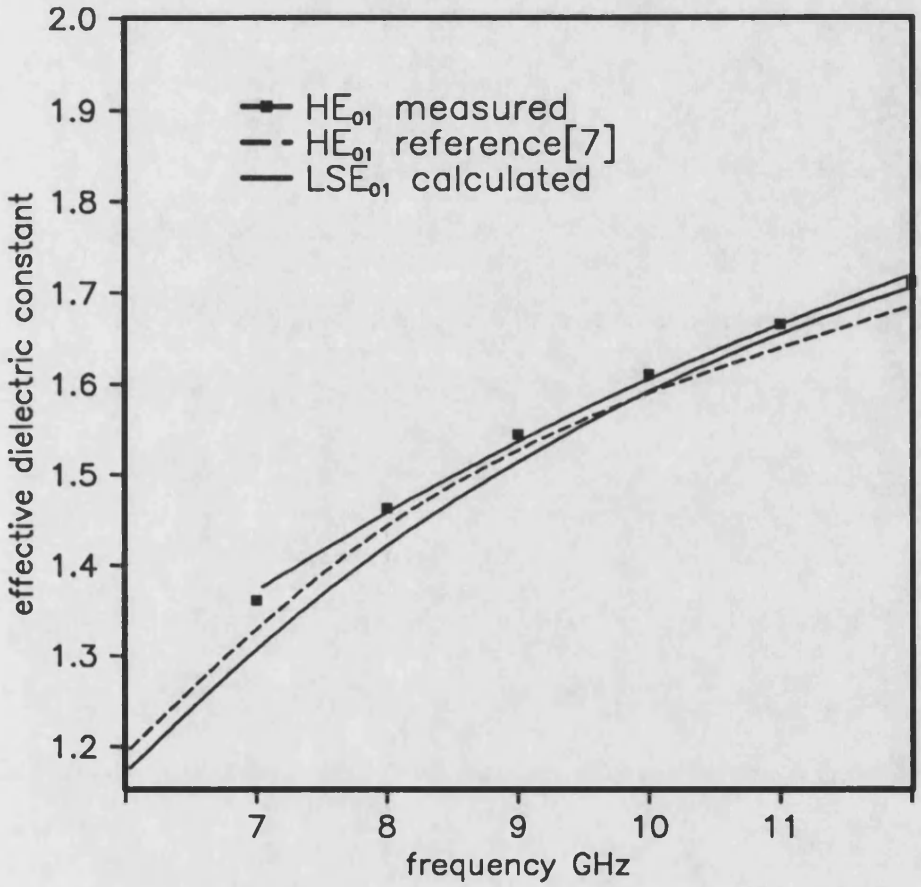

Figure 5.8: Calculated and measured dispersion characteristics of LSE_{01} mode in deep slot IDG. Slot dimensions are $10.16 \times 15.24mm$ and dielectric inset is made from PTFE.

The dielectric filling was made from PTFE, having $\epsilon = 2.08$ for dielectric constant.
The numerical data for this guide were collected over the $7-14GHz$ frequency range and compared with experimentally obtained data for the frequencies between 8 and $12GHz$. Three types of modes show up, and are assigned to LSE_{01}, LSM_{11} and LSE_{11} which are listed in order of appearance. The dispersion characteristics for these three modes are depicted in Fig.5.9. The results obtained from phase constant measurements are also presented on the same figure, and show good agreement with numerically predicted data. In order to avoid overmoding and make practical use of the shallow IDG, the slot dimensions should be chosen in such way as to promote monomode operation in the structure. Monomode operation requires that the width/height ratio of the shallow slot should be quite high, when the LSM_{11} would emerge as the fundamental mode and monomode operation is achieved over a moderate frequency rangy [8].

5.8 Coupled IDG Characterization

The aim of this thesis was to investigate coupling between two IDGs and this section is the core of that investigation. The presented results are gained through extensive numerical computation and compared with data obtained by measurements.
Both types of coupled IDGs, deep and shallow slot geometry, were treated numerically but empirical results only are available for deep IDG configuration. The phase constants of all modes were measured by the use of a resonant section technique. Different orientation of the magnetic probes in that technique allow us to pick up resonant frequencies for modes of both symmetries simultaneously from a single measurement, and reduce errors in data reading.

5.8.1 Coupling Between Deep Identical IDGs

Analysis is performed on symmetrically coupled deep slot IDGs, having dimensions $10.16 \times 15.24mm$. Dielectric filling was made from PTFE. The numerical results are presented in terms of effective dielectric constants for even and odd modes and a curves representing these

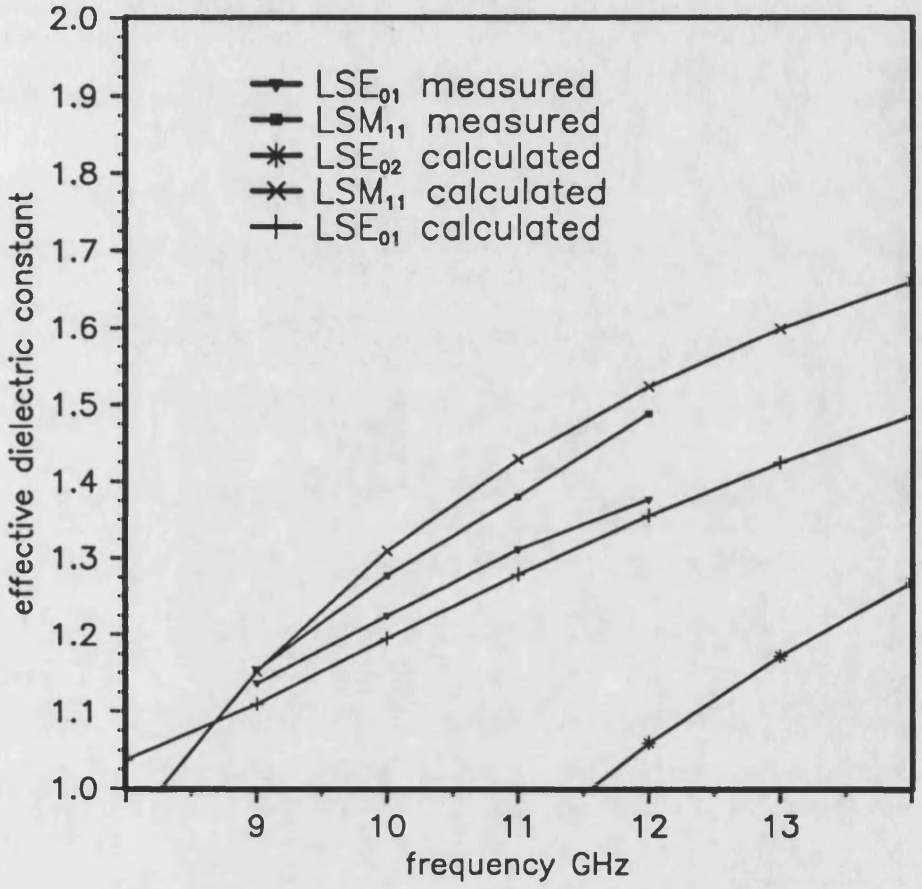

Figure 5.9: Calculated and measured dispersion characteristic for LSE_{01} and LSM_{11} modes, supported by shallow IDG structure. Slot dimensions are $22.86 \times 10.16mm$ and dielectric inset is made from PTFE.

data along with measured points for a separation of $d = 0.47mm$ between the guides are shown in Fig.5.10. The same sets of data but for a separation of $d = 1.7mm$ is presented in tabular form in Tab.5.10. From both figure and table presentations it is apparent that the phase constants of even and odd modes tend to have much more similar values for higher working frequencies. Such behavior consequently means that coupling gets weaker as the working frequency is increasing. Knowing that more energy is confined inside dielectric as frequency is increased, explains the above stated frequency characteristic of coupled deep slot IDG.

In order to investigate the influence of dielectric permittivity on coupling characteristic, deep slot IDG configuration having $\epsilon_r = 10.8$ for a ceramic filling was analysed. To be able to compare results for different guide filling, the considered guides should support the same mode and have equal monomode bandwidth. This requirements are met when the dimensions of slot filled with dielectric of higher permittivity are scaled down. It has been found that $3.24 \times 4.86mm$ filed with $\epsilon_r = 10.8$ supports the same mode and have roughly the same monomode bandwidth as IDG having $10.16 \times 15.24mm$ for slot and $\epsilon_r = 2.08$. The dispersion characteristic for this guide is presented in terms of effective dielectric constant for even and odd modes in Fig.5.11.

It was noticed from the measurements that the IDG coupler gives a very low level of return loss and that the isolation was excellent. For this reasons the return and isolation power loss were neglected. Under such assumption the (2.13) can be understood in the sense of scattering parameters, $S_{12}\&S_{13}$, for the case when the unit incident wave is applied on one of the symmetrically coupled IDG ports:

$$|S_{13}| = 10 \times \log\left(\sin^2\left(\frac{\beta_{even} - \beta_{odd}}{2} \times L\right)\right) \tag{5.3}$$

The Fig.5.12 shows the coupling per coupled guide wavelength against guide separation plotted for two guides with different slot dimensions and filling permittivity, but both with the same monomode frequency range. Clearly the higher permittivity filling acts to concentrate

freq	β_e^c	β_e^m	β_o^c	β_o^m
8	197.489	198.140	202.860	203.107
9	228.563	229.973	233.421	234.282
10	260.413	260.902	264.761	265.424
11	292.766	292.233	296.185	296.165
12	324.061	323.782	326.409	326.638

Table 5.10: Computed and measured values for β of deep slot coupled IDGs. Slot dimensions are $10.16 \times 15.24mm$, filled with PTFE and separated by $s = 1.7mm$

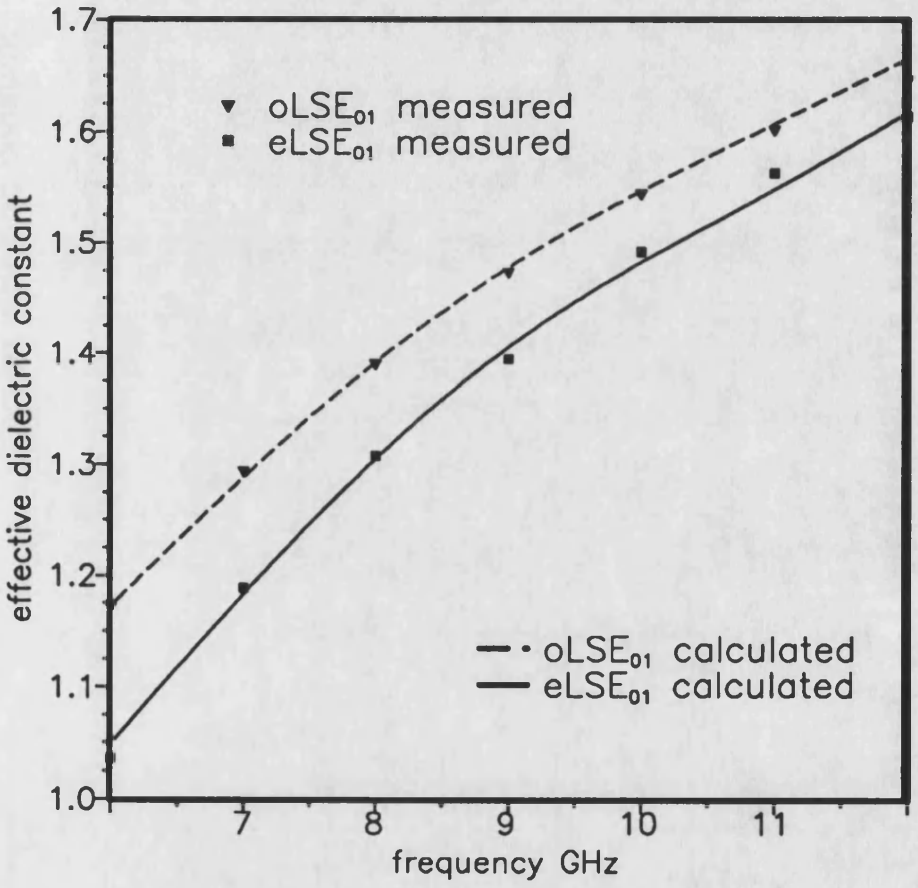

Figure 5.10: Calculated and measured dispersion characteristic for LSE_{01} mode of even and odd symmetry supported by deep slot symmetrically coupled IDGs. Slot dimensions are $10.16 \times 15.24mm$ and dielectric inserts are made from PTFE. Separation between lines is $d = 0.5mm$

.

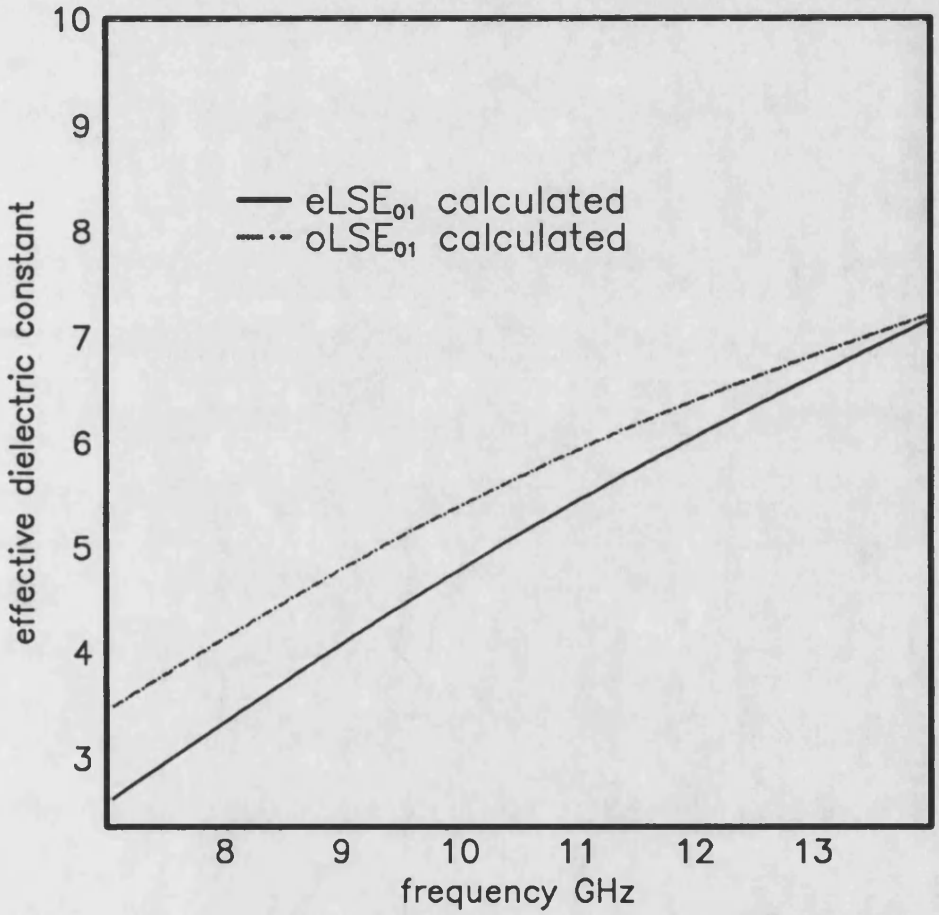

Figure 5.11: Dispersion characteristic for even and odd symmetry of LSE_{01} mode supported by deep slot coupled IDGs. Slot dimensions are $3.24 \times 4.86mm$ and dielectric inserts have $\epsilon = 10.8$ for dielectric permittivity. Separation between lines is $0.1mm$.

the field within the slot and hence reduce the coupling effect. The guide wavelength in the high permittivity case is almost half that of the PTFE filled case, so when considering equal physical separation the difference in coupling is even more pronounced. Consequently, in applications where coupling is to be avoided, smaller IDGs filled with a high permittivity material should be used. Such an application might be the implementation of parallel sets of radiating dipoles in a two dimensional array antenna. The reduction in guide size facilitates the avoidance of grating lobes, while the coupling could be reduced to negligible level, greatly simplifying analysis and design.

5.8.2 Coupling Characteristics for Shallow Slot IDGs

As previously stated, shallow IDG structure does not appear to have wide monomode operation range and because that, coupling characteristics for fundamental mode of LSE and LSM polarization have been investigated. The dimensions of the shallow slot used in numerical computation are $22.86 \times 10.16mm$, and these dimensions were chosen for compatibility with metal rectangular X band waveguide which was used for the purpose of IDG excitation. The IDG structure of these dimensions is capable of supporting LSE_{01} and LSM_{11} modes over the X band frequency range. The dispersion characteristic of normal modes for the coupled shallow IDG structure is presented in Fig.5.13, for a separation of $0.5mm$ between guides. The coupling is much greater for the LSM_{11} mode than for the LSE_{01} mode of the same IDG structure. The coupling characteristic versus shallow guide separation is presented in Fig.5.14. Comparing this characteristic with the relevant characteristic of deep IDGs, Fig.5.12, we notice that for small separations coupling is much stronger between the shallow slots, while for separations of $0.08\, d/\lambda_g$ and greater, the coupling factors are quite similar.

5.9 Phase Constant Measurements

For the sake of accurate assessment, a comparison between computed and measured data is needed. The measurements were carried out at the X band frequency range, $8 - 12.4GHz$,

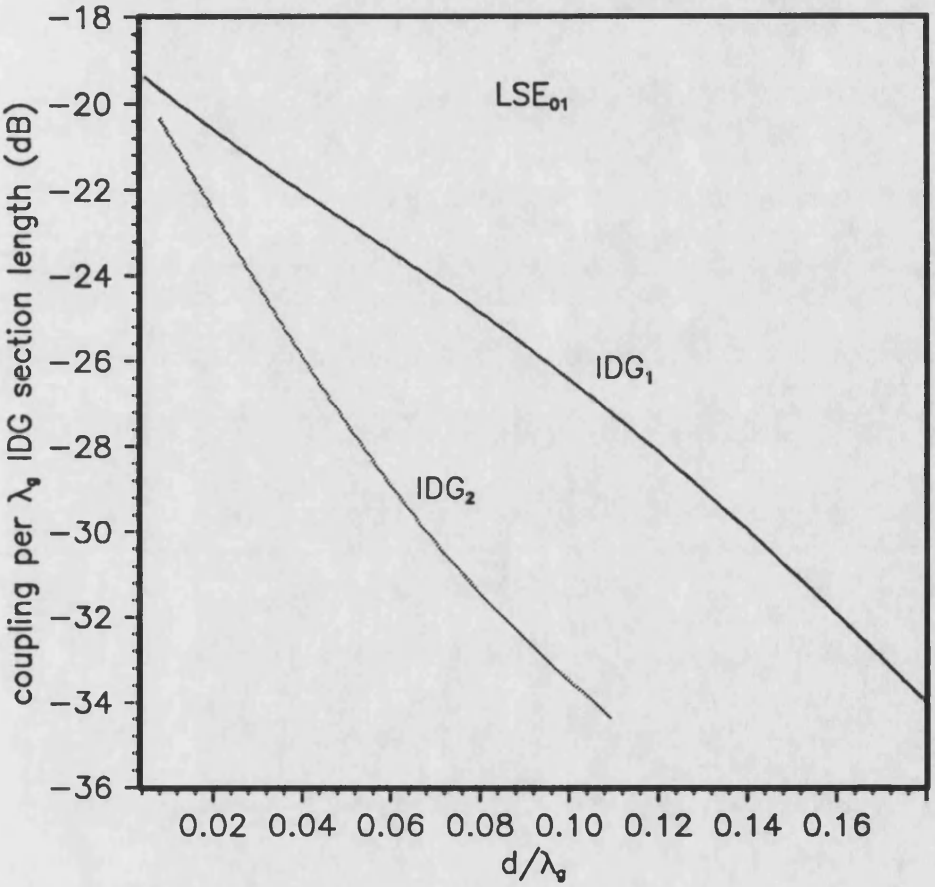

Figure 5.12: Coupling characteristic for LSE_{01} mode versus guide separation between deep IDGs. IDG1 has dielectric inset made from PTFE and is set to fill $10.16 \times 15.24mm$ slot completely. IDG2 slot $3.24 \times 4.86mm$ is full-filled with ceramic dielectric inset having $\epsilon_r = 10.8$ for dielectric permittivity. Working frequency is 9.0 GHz.

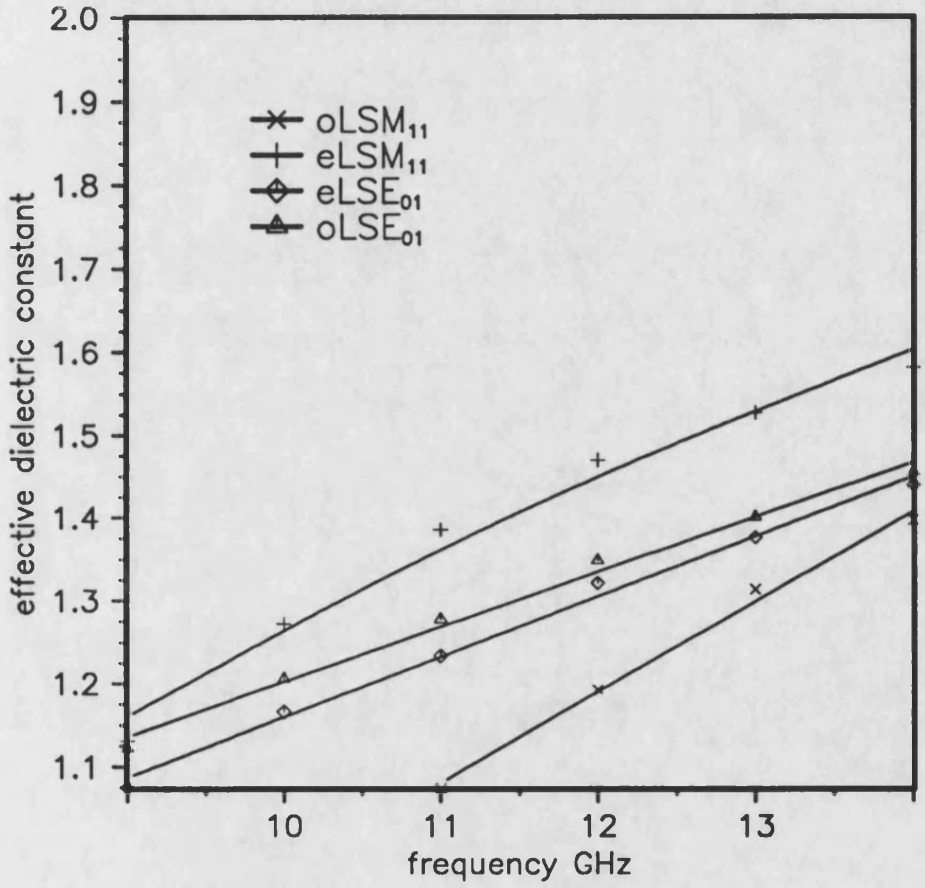

Figure 5.13: Dispersion characteristic for LSE_{01} and LSM_{11} modes of even and odd symmetry supported by shallow slot coupled IDGs. Slot dimensions are $22.86 \times 10.16mm$ and dielectric inset is made from PTFE.

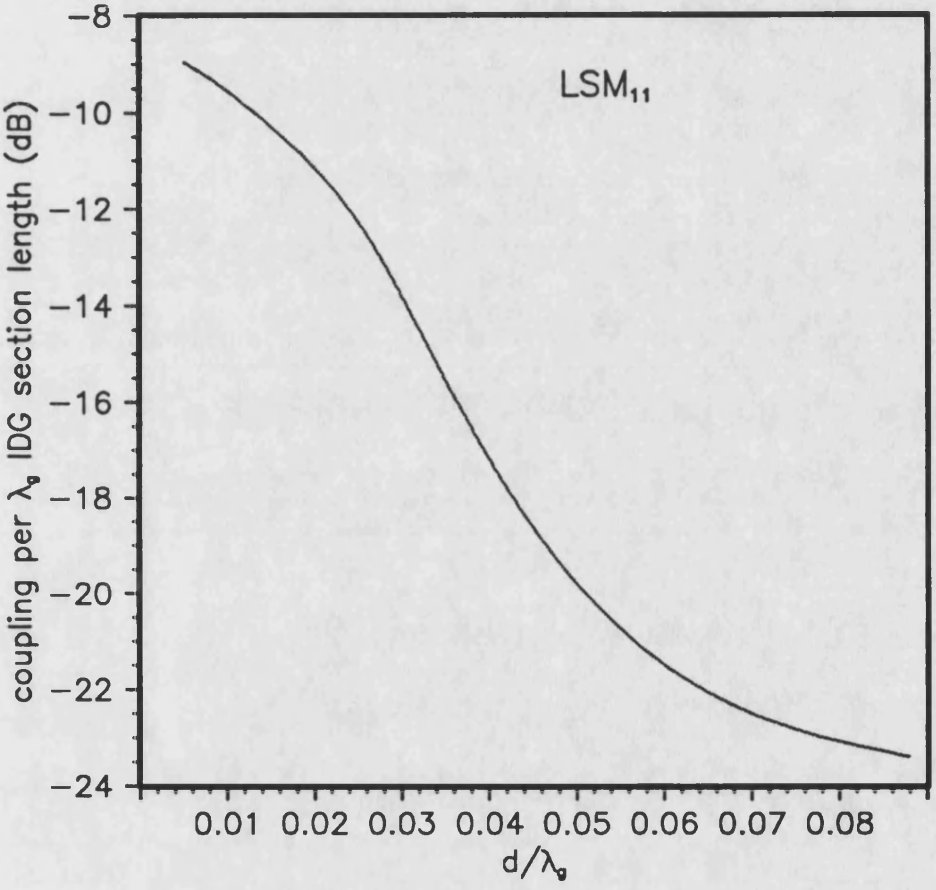

Figure 5.14: Coupling characteristic for LSM_{11} mode of shallow IDG structure versus guide separation. Slot dimensions are $22.86 \times 10.16mm$ and dielectric inset is made from PTFE. Working frequency is 11.0 GHz.

due to availability of equipment and measuring system. The measurement of the single IDG line has been already described [7], and here we pay attention only to the phase constant measurements of coupled IDG lines.

The initial test piece was made from aluminum into which deep slots had been machined. A separation wall between two slots was made to be removable, and this enabled measurements for various spacings between the lines. In order to facilitate the transition from rectangular waveguide to IDG, the slots were kept at the standard rectangular waveguide width, $10.16mm$ for the X band. A drawing of the test jig used is given in Fig.5.15. The dielectric inserts were machined from PTFE and had cross section of 10.16×15.24.

The dispersion characteristic of the normal, even and odd modes of the coupled IDGs were measured by using the resonant section technique. Metal plates are fixed at both ends of a section of line forming short circuit loads. Magnetic probes are positioned symmetrically above the IDG lines through holes drilled in the shorting plates. In order to determine accurate values for phase constant, the coupling between the probes and the IDG structure should be low so that the end plates act as short circuit loads. This is achieved by controlling the distance between the probes and top surface of the IDG line. Such a geometry will thus support only those waves which can meet the requirement that the electric field is zero at each end of the resonant structure. The power transmission through the structure shows resonant maxima when the intermediate line length is an integral number of half wavelengths, so phase constants are determined at discrete frequencies. Mathematically the above statement can be expressed as:

$$\frac{n\lambda_g}{2} = L \tag{5.4}$$

where λ_g = wavelength of the bounded wave

n = integer

L = length of resonant section.

In addition, the orientation of the magnetic loop probes facilitates relatively independent excitation of modes with even and odd symmetries about the probe position. The swept

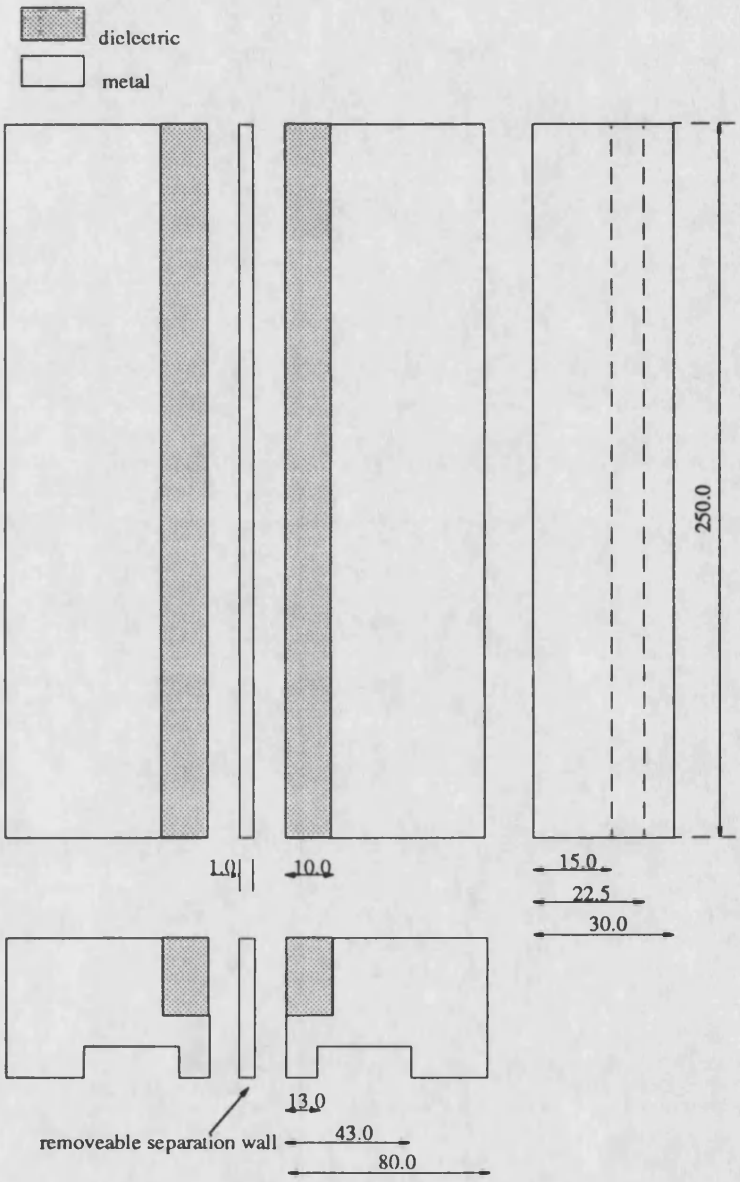

Figure 5.15: The X band test jig used for the purpose of deep slot IDG coupling characterization.

frequency transmission response of a $L = 250mm$ long coupled section of deep slot IDGs excited by weak coupling of odd symmetry is shown in Fig.5.16. When the orientation of the two probes are altered, the resonant peaks for normal modes of both symmetry appears at the same time, which is shown in Fig.5.17. The readings for resonant frequencies for guided modes of both symmetry can be taken from single measurements. Various errors associated with measuring process are of the same magnitude for either symmetry mode, and thus the relative error relevant to the calculation of coupling coefficient will be low.

The center frequency of each peak determines the wavelength of the guided wave. Also, the order of a resonant frequency associated with integer n in (5.4) had to be evaluated by tuning the source to a resonant frequency and measuring the guide wavelength with a field probe.

Tab.5.11 gives the measured dispersion results in the terms of effective dielectric constant for even and odd modes. The concerned coupling section was $L = 250mm$ having $10.16 \times 15.24mm$ for slot dimensions and dielectric inserts were made from PTFE.

5.10 Transition Section

A transition section is needed for the purpose of connection of any practical IDG circuit into a rectangular waveguide system. The fundamental mode in deep slot IDG, LSE_{01}, has been shown [7] to have a field distribution very similar to that of the TE_{10} mode of rectangular metal waveguide. So the main requirement is an impedance matching between the two types of guide. The impedance matching is utilized by the means of dielectric taper placed inside the metal waveguide, rising from zero height to the height of the IDG. Although, it was seen that such taper provides broadband matching, the transition is not optimized in any way. The power loss is present in all of the IDG measurements and as guide loss of IDG is calculated to be low [7], the extra loss is associated with radiation and mode conversion losses. The loss becomes more considerable at the higher frequencies and examination of transitions used to launch the LSE_{01} mode is needed in order to obtain explanation for such

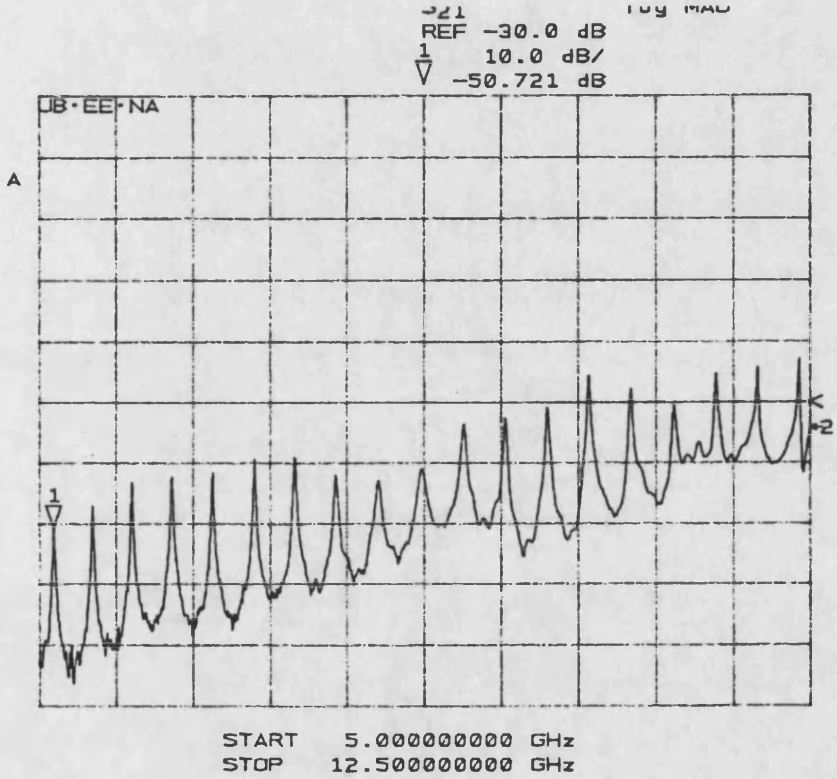

Figure 5.16: The measured insertion loss of a resonant section of the coupled IDGs. The magnetic probes were set to emphasize LSE_{01} mode of odd symmetry. The resonant section was $L = 250mm$ long and slot dimensions were $10.16 \times 15.24mm$. Dielectric inserts were made from PTFE while guide separation was $0.47mm$.

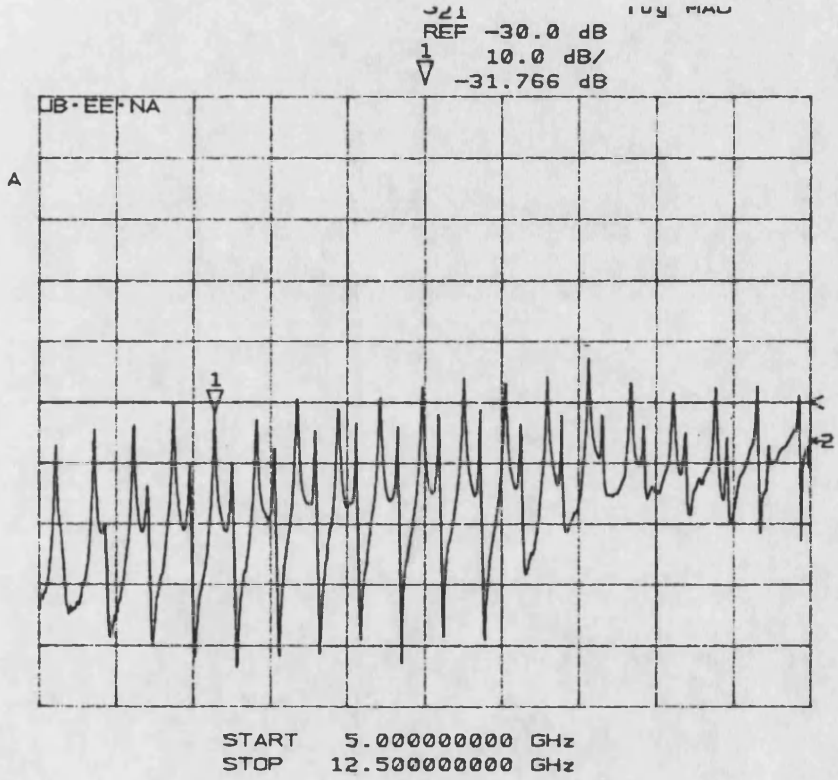

Figure 5.17: The measured insertion loss of a resonant section of the coupled deep slot IDG structure. The magnetic probes were set to excite LSE_{01} mode of odd and even symmetry simultaneously. The resonant section was $L = 250mm$ long and slot dimensions were $10.16 \times 15.24mm$. Dielectric inserts were made from PTFE while guide separation was $0.47mm$.

β_{res}	f_{odd}	$K_{0\,odd}$	$\epsilon_{eff\,odd}$	f_{evn}	$K_{0\,evn}$	$\epsilon_{eff\,evn}$
113.097	5.169	108.204	1.0925	5.216	109.188	1.0729
125.664	5.544	116.054	1.1725	5.637	118.001	1.1341
138.230	5.928	124.092	1.2408	6.059	126.835	1.1878
150.796	6.312	132.131	1.3025	6.472	135.480	1.2389
163.363	6.706	140.378	1.3543	6.875	143.916	1.2885
175.929	7.119	149.024	1.3937	7.297	152.750	1.3265
188.495	7.512	157.251	1.4369	7.690	160.977	1.3711
201.062	7.916	165.708	1.4722	8.094	169.434	1.4082
213.628	8.328	174.332	1.5016	8.497	177.870	1.4425
226.195	8.731	182.768	1.5317	8.891	186.118	1.4470
238.761	9.134	191.205	1.5593	9.294	194.554	1.5061
251.327	9.537	199.641	1.5848	9.687	202.781	1.5361
263.894	9.950	208.286	1.6052	10.091	211.238	1.5607
276.460	10.353	216.722	1.6273	10.484	219.465	1.5868
289.026	10.765	225.347	1.6450	10.887	227.901	1.6084
301.593	11.168	233.783	1.6642	11.290	236.337	1.6285
314.159	11.581	242.428	1.6793	11.694	244.794	1.6470
326.725	11.984	250.865	1.6962	12.097	253.230	1.6647

Table 5.11: Measured values for phase constants of LSE_{01} mode of even and odd symmetry in deep slot ($10.16 \times 15.24mm$) IDG geometry with PTFE dielectric filling, $\epsilon_r = 2.08$. Guide separation is $s = 0.25mm$.

behavior. The transitions were investigated in terms of power loss. The two transitions were connected back to back and the S parameters were measured using the HP8510 Network Analyzer. The deviation of measured S parameters from the unitary principle

$$|S_{11}|^2 + |S_{12}|^2 = 1 \tag{5.5}$$

gives a measure of the loss inside the transition.

From Fig.5.18, which shows the loss for transition sections where the dielectric taper rises to the height of the metal guide, it is noticeable that the loss is considerable for frequencies above 11 GHz. Such behavior can be explained by the fact that dielectric filling reduces the cut-off frequency of the TE_{20} mode, which starts to propagate at about 11GHz.

By lowering down the height of dielectric filling, the slope angle of taper is decreasing but loss caused by energy transformation to local modes is still considerable, Fig.5.19. To avoid this difficulties the height of metal waveguide should be tapered down as the dielectric taper rises up and the cross-section of such launcher is depicted in Fig.5.20. By lowering down the height of launcher we try to increase the cut-off frequency of the TE_{20} mode in the dielectric filed guide.

A theoretical analysis to find an optimum shape of the launcher and the dielectric taper inside, can be done by converting Maxwell's equations for this structure into generalized telegraphist's equations. By this conversion, wave propagation in the transition is represented in terms of local normal modes for any cross-section within the transition. The coupling between these local modes is introduced by the change of the cross-section with axial distance. For a particular mode to be launched efficiently, the transition must be gradual and coupling between local modes must be small. The telegraphist's equation are then nearly independent from each other and may be solved by iteration [9].

The performance of launcher proposed in Fig.5.20 can be degraded by three different effects:

- reflection
- mode conversion

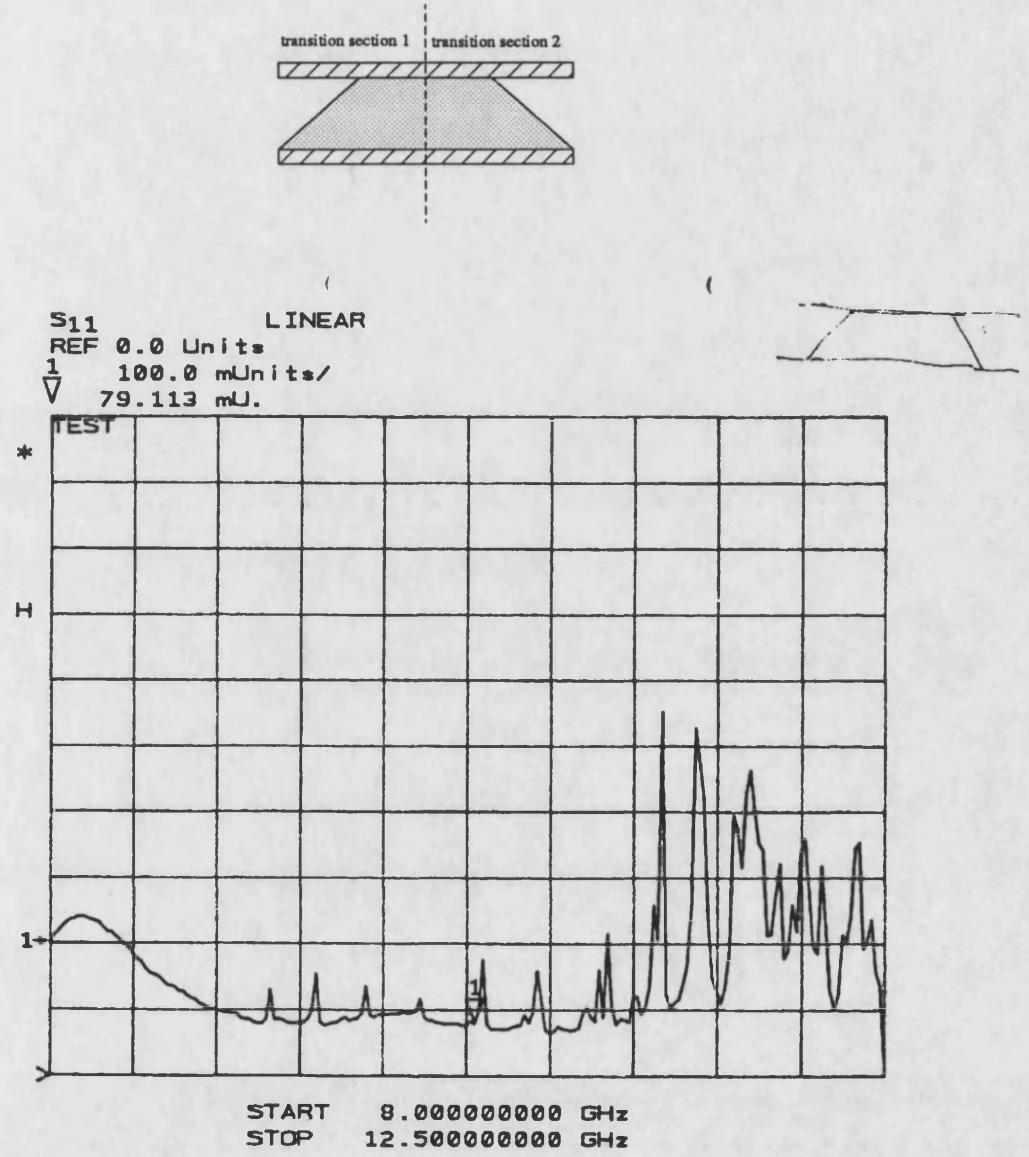

Figure 5.18: Transmission loss of two metal waveguide-to-IDG transition sections connected back to back. The height of dielectric taper located inside transition is raised to the full height of metal guide. The dimensions of metal waveguide are 10.16 × 22.86mm while permittivity of inserted dielectric taper is ϵ=2.08

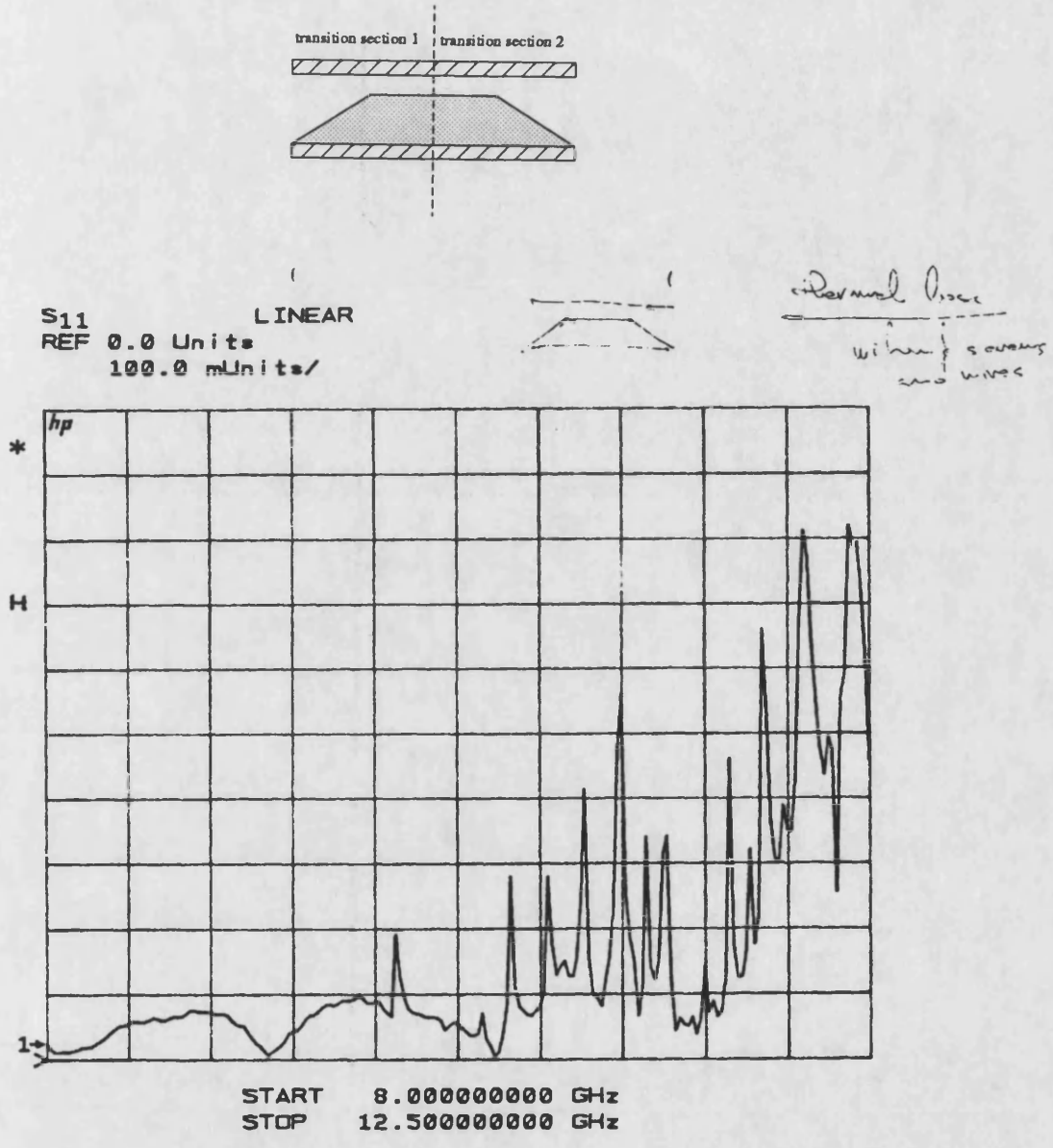

Figure 5.19: Transmission loss of two metal waveguide-to-IDG transition sections connected back to back. The height of dielectric taper located inside transition is raised to the height of 15.24mm. The dimensions of metal waveguide are 10.16 $\times$ 22.86mm while permittivity of inserted dielectric taper is ϵ=2.08

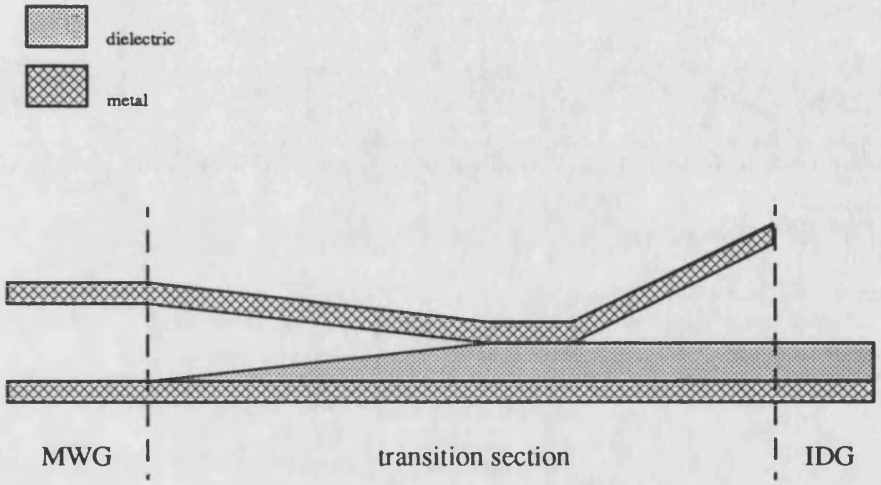

Figure 5.20: The proposed transition section for metal waveguide to IDG connection. The aim of dielectric taper inside transition is to match impedances while tapering of top metal wall should preserve monomode operation of transition section. Flaring section on the output of the transition plays role in reducing radiation loss.

- radiation

For reflections to be small, the tapers should be sufficiently gradual. Mode conversion to local normal modes can be kept low by making flare angles small. Radiation loss is controlled by the length of the horn aperture.

5.11 Conclusion

This chapter was concerned with the solutions of the coupled IDG dispersion equation for various modes of single and coupled lines under LSE and LSM polarization.
First of all, scale coefficients making the basis set better fit the unknown field had to be evaluated in the order to improve convergence of numerical approach used.
The solutions for the phase constant β opened up the possibility of calculating field amplitudes and plotting field patterns in the air region over single and coupled IDGs.
The mode type classification in terms of two polarizations is described. Also it is found that LSE_{mn} mode assignation quite clearly corresponds to the HE_{mn} hybrid field notation. On other hand LSM_{mn} is related to the EH_{mn} modes.
The procedure for approximate calculation of single IDG phase constant is presented and shows excellent agreement with measured data and data obtained through application of full hybrid mode analysis [7].
The phase constants for both type of IDG, deep and shallow slot IDG, have been calculated for LSE and LSM types of polarisation by approach developed in this thesis. These data are in good correlation with previously reported data [7], too.
The results for coupled IDG sections are presented for both types of IDG configuration as well as for different modes of propagation. These results were also compared with measured data and shows rather excellent agreement.
The transition section used to match rectangular metal waveguide to IDG is analysed in term of power loss and a new launcher structure for the improved performance is proposed.

References

[1] M. J. Box

A comparison of several current optimization methods and the use of transformations in constrained problems

Computer Journal (9) 1966, pp.67-77

[2] B. Friedman

Lectures on Applications-oriented Mathematics

Holden-Day, Inc.,San Francisco 1969 ch.5

[3] P. J. Davies and P. Rabinowitz

Methods of Numerical Integration

Academic Press, New York 1975,

[4] C. de Boor

CADRE: An algorithm for numerical quadrature

Mathematical Software, Academic Press, New York 1971, ch.7

[5] G. & M. Forsythe and B. Cleve

Computer Solution of Linear Algebraic Systems

Prentice Hall inc., Englewood Cliffs, New Jersey 1967

[6] R. P. Brent

An algorithm with guaranteed convergence for a finding zero of a function

The Computer Journal, 14(4) 1971 pp.422-425

[7] T. Rozzi and S. J. Hedges
Rigorous Analysis and Network Modeling of the Inset Dielectric Guide
IEEE Trans. Microwave Theory and Tech. vol.MTT-35 Sep.1987,pp.823-833

[8] T. Rozzi, S. R. Pennock and N. Izzat
Bandwidth Control in Multilayer Inset Dielectric Guide
20th European Microwave Conference, Budapest Sept. 1990, paperP.1.19

[9] W. Schlosser and H.-G. Unger
Partially Filled Waveguides and Surface Waveguides of Rectangular Cross-Section
1966 Advances in Microwaves, vol.1 pp.319-387

Chapter 6

Multihole IDG Coupler

Having characterized coupled IDG, the design of a directional coupler in IDG comes naturally as the next step. In common with all dielectric guides IDG possesses coupling characteristic which is frequency dependent. However, for most applications flat coupling is desired and an additional coupling mechanism is sought in order to make overall coupling flat over a certain frequency range.

One method of doing this, which is very simple to include, is to superimpose a multihole array drilled in the metal separation wall between the two IDGs. The coupling characteristics of two employed mechanisms are different in nature, intrinsic IDG coupling is continuous while coupling through holes is discrete. The distributed coupling is a common feature for both mechanisms, and by choosing right parameters of distributed coupling, balance between two mechanisms can be achieved. This approach of flattening coupling response, opens new avenues in the design of IDG devices and subsystems.

6.1 Multihole Coupler Theory

Among the earliest types of directional coupler were those coupling two identical waveguides by means of one or more apertures in the common wall. Bethe's theoretical work on small hole coupling [1] provides a good base for multiaperture waveguide directional coupler design.

The basic assumption there is that the radius of the hole must be considerably smaller than the wavelength in the waveguide.

The field coupled through an aperture in a guide wall, whose linear dimensions are small compared to the wavelength and which is far away from any discontinuity, is that radiated by an electric and magnetic charge and current distributions set up at the aperture by the exciting field.

It has already been noted that the field components of the fundamental deep slot IDG mode, HE_{01}, are very similar to those of TE_{10} mode metal waveguide [2]. This similarity between field distributions of HE_{01} mode of IDG and TE_{01} mode of rectangular metal waveguide filled with the same dielectric as the IDG is specially emphasized in the region close to the groove bottom.

So, we can use the multihole coupling theory developed for metal guides adjusted to include parameters and features of the IDG transmission media. The forward coupled wave, $\mathcal{A}$, and backward coupled wave ,$\mathcal{B}$, are determined by the waveguide fields at the center of the hole: E_x, H_y, H_z; the magnetic polarizability of the aperture: M_y, M_z; and the electric polarizability normal to the hole: P.

$$\begin{aligned} \mathcal{A} &= \jmath\frac{2\pi}{ah\lambda_g}\left[+M_yH_{1y}H_{2y} + M_zH_{1z}H_{2z} - PE_{1x}E_{2x}\right] \\ \mathcal{B} &= \jmath\frac{2\pi}{ah\lambda_g}\left[-M_yH_{1y}H_{2y} + M_zH_{1z}H_{2z} - PE_{1x}E_{2x}\right] \end{aligned} \tag{6.1}$$

For the case of two identical guides, $H_{1y} = H_{2y}$ and etc., the field components in a metal rectangular waveguide with unit excitation are given as:

$$\begin{aligned} H_y &= -\sin\left(\frac{\pi y}{h}\right) \\ H_z &= \jmath\frac{1}{\sqrt{\epsilon_r}}\frac{\lambda_g}{2h}\cos\left(\frac{\pi y}{h}\right) \\ E_x &= \frac{\lambda_g}{\lambda}\sin\left(\frac{\pi y}{h}\right) \end{aligned} \tag{6.2}$$

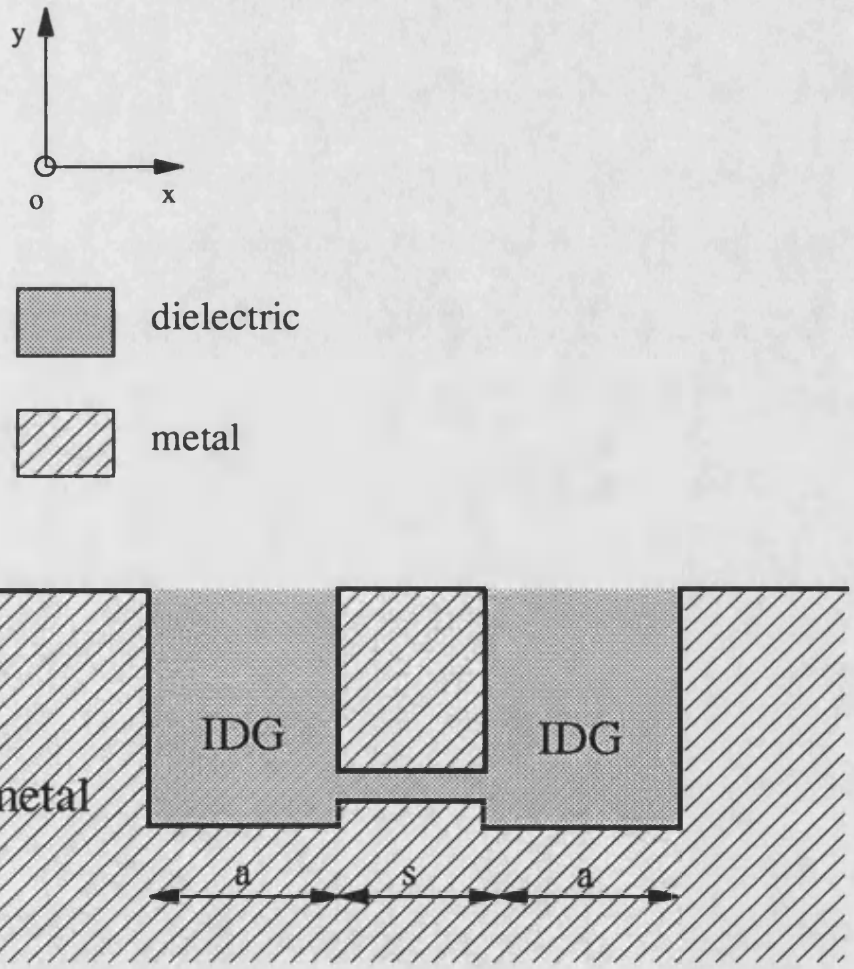

Figure 6.1: Symmetric coupled IDG cross-section additionally coupled by the means of holes drilled through separation wall

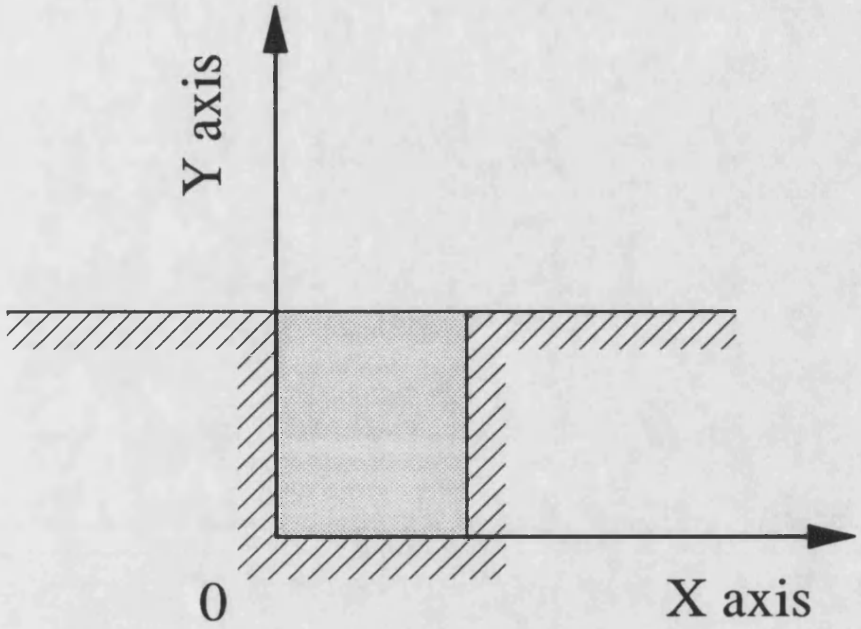

Figure 6.2: Reference coordinate system used in the process of coupling evaluation between two adjacent IDGs additionally coupled by array of holes.

where λ_g - wavelength of guided wave

λ - wavelength in unbounded media

The reference coordinate system used in the expressions for field components and later calculation of magnitude of coupled waves is shown in Fig.6.2.

The same expressions (6.2) are used to describe field in deep slot IDG near the groove floor, but using the wavelength and propagation constants relevant for the HE_{01} IDG mode.

6.1.1 Hole in narrow wall

When a hole is placed in the narrow wall, the case corresponds to the coupling of shallow slot IDGs by means of an additional aperture in the separation wall. The expressions for forward

and backward coupling (6.1) get reduced to:

$$\mathcal{A} = \mathcal{B} = \frac{j\lambda_g M_z}{2\epsilon_r a^3 h} \tag{6.3}$$

due to fact that y=0. Since the magnetic polarizability M_z is frequency independent, the magnitude of forward and backward wave is directly proportional to λ_g. Then, the hole coupling has the same frequency dependence as the inherent IDG coupling. This conclusion is only valid for HE_{mn} modes of a shallow guide. However shallow structures of certain height/width ratios favor EH_{11} mode and the coupling between two adjacent IDGs supporting this type of field distribution can be balanced by the use of an arrays of holes again. If slot depth is too small to accommodate holes of a specific size, then the transverse slot can be used as directive aperture [4]. Also, the use of elliptic holes as the aperture can be considered in this application.

6.1.2 Hole in broad wall

The case of coupling deep IDGs by holes drilled in separation wall between the guides is equivalent to the metal waveguide coupling by use of a hole in the broad wall. In contrast to the case of a hole in narrow wall, the expressions for field components possess one degree of freedom more, because $y \neq 0$. By substituting (6.2) into (6.1) the amplitudes for forward and backward coupled waves are found as:

$$\begin{aligned}
\mathcal{A} &= \frac{j2\pi}{ah\lambda_g}\left\{\left[M_y - \left(\frac{\lambda_g}{\lambda}\right)^2 P\right]\sin^2\left(\frac{\pi y}{h}\right) + M_z\left(\frac{\lambda_g}{2\epsilon_r h}\right)^2\cos^2\left(\frac{\pi x}{h}\right)\right\} \\
\mathcal{B} &= \frac{j2\pi}{ah\lambda_g}\left\{\left[M_y + \left(\frac{\lambda_g}{\lambda}\right)^2 P\right]\sin^2\left(\frac{\pi y}{h}\right) - M_z\left(\frac{\lambda_g}{2\epsilon_r h}\right)^2\cos^2\left(\frac{\pi x}{h}\right)\right\}
\end{aligned} \tag{6.4}$$

For the case where a circular hole of radius d_i is used as an aperture, the polarizabilities are given by

$$M_y = M_z = \frac{d^3}{6} = \frac{2P}{\epsilon_r} \tag{6.5}$$

Moreover, when holes are placed at points with coordinate $(0, h/4)$ and the LSE_{01} mode is considered, the expressions (6.4) reduce to the form

$$\begin{aligned} \mathcal{A} &= \frac{\jmath\pi d^3}{24h^2a}\left[\frac{2h}{\lambda_g}+\frac{\lambda_g}{2h}\right] \\ \mathcal{B} &= \frac{\jmath\pi d^3}{24h^2a}\left[\frac{6h}{\lambda_g}-\frac{\lambda_g}{2h}\right] \end{aligned} \tag{6.6}$$

The frequency dependence is apparent, and for $\lambda_g \leq 2h$, the first term in square brackets determines that the amplitude of the forward coupled wave increases with frequency. This kind of behavior is just right for the application considered here where the compensation of the inherent IDG coupling characteristic is needed.

6.2 Equivalent Network of an Aperture

Consider two identical waveguides which are coupled by means of an aperture in the common wall. As stated earlier, the analysis of a four port network associated with coupled symmetric lines can be performed in terms of even and odd excitation modes. This approach reduces the analysis of four-port network to one of two, two-port networks. So, the problem of coupling through an aperture can be alternatively considered as an obstacle placed in the middle of the transmission line section.

The equivalent network for an obstacle in a closed waveguide can be represented in terms of reactive lumped elements whose values are related to the geometry of the obstacle. There are different ways to find values of these lumped elements and two different approaches were utilized by Markuwitz [5] and Oliner [6] in the early days of aperture coupler development. For the case of symmetrical and lossless obstacles only two different parameters are needed for its correct circuit representation, Fig.6.3. Strictly speaking, the equivalent network is valid only for monomode operation, and if multimode operation is considered different element values should be determined for each possible mode of propagation.

The reflection and transmission coefficients of the two port network in Fig.6.3 are calculated

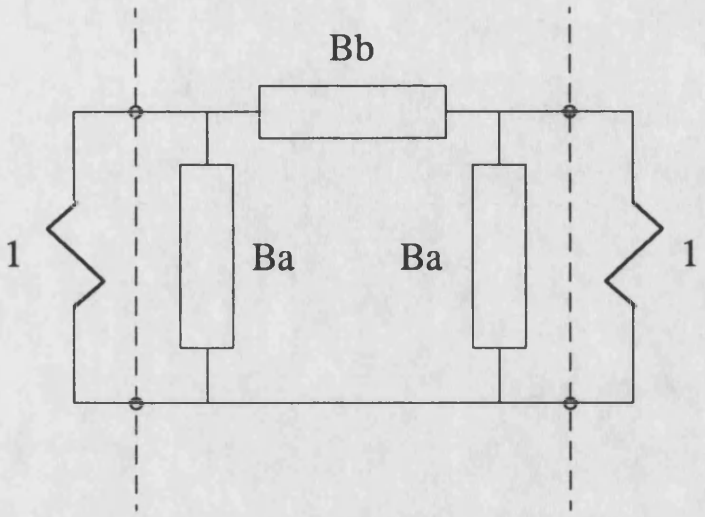

Figure 6.3: Two port equivalent network modeling an obstacle

as

$$\begin{aligned} \Gamma &= \frac{\jmath/B_b - \jmath(2B_a + B_a^2/B_b)}{\Sigma} \\ T &= \frac{2}{\Sigma} \end{aligned} \tag{6.7}$$

with $$\Sigma = 2(1 + B_a/B_b + \jmath(2B_a - 1/B_b + B_a^2/B_b)$$

As elements B_a and B_b are proportional to the third order of obstacle dimensions, all higher orders of B_a and B_b will be neglected and (6.7) gets a very simply form

$$\begin{aligned} \Gamma &= -\jmath(B_a + \frac{1}{2B_b}) \\ \mathrm{T} &= 1 - \jmath(B_a - \frac{1}{2B_b}) \end{aligned} \tag{6.8}$$

A four port network suitable for modelling coupling through an aperture in a common wall of the coupled guide structure is depicted in Fig.6.4.

This model comprises two back to back connected II networks bridged across by an additional

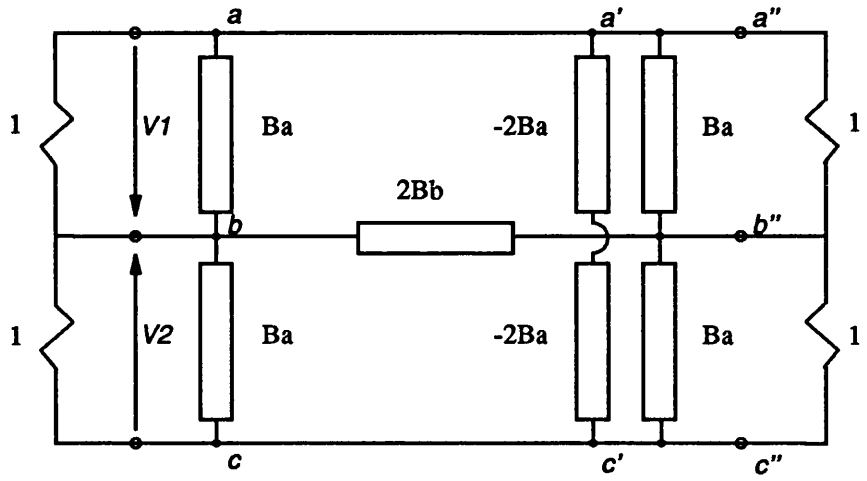

Figure 6.4: A four port network modeling two guides coupled by means of an aperture placed in the common wall.

element $-B_a$. Now we analyse this four port network under even and odd type of polarization. For the even mode $V_1 = V_2$ and points a' and c' are at the same potential, and consequently shunt element can be omitted because no current flows through it. In that case the equivalent network for an aperture in the common wall of two coupled guides is reduced to the Π network previously seen in Fig.6.3.

For odd mode excitation $V_1 = -V_2$, points b and b'' are on same potential, therefore no currents flows through series admittance which can then be eliminated. As the total shunt admittance at each of the two identical two port networks is $B_a - 2B_a + B_a = 0$, straight connection is obtained for the equivalent model of an aperture under odd excitation. This means that the discontinuity caused by the placement of an aperture in a common wall is not seen by odd mode excitation.

6.2.1 Elements of equivalent network

The elements of the aperture equivalent network can be expressed in terms of field parameters and aperture dimensions. The next two identities are taken from [7]

$$\begin{aligned} -e_x - h_y + h_z &= \mp\jmath(B_a + \frac{1}{2B_b}) \\ -e_x + h_y + h_z &= \mp\jmath(B_a - \frac{1}{2B_b}) \end{aligned} \tag{6.9}$$

yielding

$$\begin{aligned} \jmath B_a &= h_z - e_x \\ \jmath\frac{1}{B_b} &= 2h_y \end{aligned} \tag{6.10}$$

where e_x, h_y and h_z are given by:

$$\begin{aligned} e_y &= \frac{\jmath\beta}{ah} P \left(\frac{k_0}{\beta}\right)^2 \sin^2 qy \\ h_x &= \frac{\jmath\beta}{ah} M_x \sin^2 qy \\ h_z &= \frac{\jmath\beta}{ah} M_z \left(\frac{\pi}{a\beta}\right)^2 \cos^2 qy \end{aligned} \tag{6.11}$$

The above equations determine the equivalent network of an aperture. The elements also depend on the shape and size of the aperture. For different shapes, different formulas for magnetic polarizability should be applied. Here, we limit ourself to circular aperture only and electric and magnetic polarizabilities are given by (6.5).

6.2.2 Correction for wall thickness and large aperture

The previously defined network that models a hole as an obstacle has limited validity because it was derived under the constraints:

- hole diameters are small compared with wavelength

- holes are not close to each other
- wall thickness is negligible

The procedure for the correction of Bethe's equation due to finite wall thickness and large aperture dimensions was established by Cohn [8]. The influence of the perturbing structures is difficult to include into the model, but this influence is estimated to be usually small for most cases of practical interest, and will be omitted from consideration.

Here, we model the influence of the finite wall thickness by a means of susceptance $B_{c,e}$ for even symmetry excitation and reactance $X_{c,o}$ for excitation of odd symmetry. The model in Fig. 6.4 transforms itself into suitable forms capable of incorporating the correction susceptance and reactance,Fig. 6.5.

The hole is understood as a circular waveguide having its length equal to the thickness of the metal wall separating the two IDG insets. The circular guide mode whose field distribution most matches that in the IDG at most, is found to be TM_{01}. For the excitation of even symmetry a magnetic wall is placed between the guides in such way that it cuts the circular guide into two halves. Then, the correction susceptance is modeled as point driving impedance of short circuited $s/2$ long circular guide section.

On the other hand, correction reactance for odd symmetry is modeled as the driving point impedance of the same circular guide section terminated with a metal wall at the other end.

$$B_{c,e} = -\jmath\frac{d}{h}\frac{\epsilon_r K_0^2}{\sqrt{\frac{4w_{01}}{d^2} - \epsilon_r K_0^2}\sqrt{\epsilon_r K_0^2 - q^2}} \tanh\left(\sqrt{\frac{4w_{01}}{d^2} - \epsilon_r K_0^2}\frac{s}{2}\right) \tag{6.12}$$

$$X_{c,o} = +\jmath\frac{d}{h}\frac{\sqrt{\frac{4w_{01}}{d^2} - \epsilon_r K_0^2}\sqrt{\epsilon_r K_0^2 - q^2}}{\epsilon_r K_0^2} \tanh\left(\sqrt{\frac{4w_{01}}{d^2} - \epsilon_r K_0^2}\frac{s}{2}\right) \tag{6.13}$$

Both correction elements comprise d/h ratio which represents transformer coefficient used in order to maintain continuity of dc voltage at the discontinuity interface between the inset and circular guides [9]. Other parameters are listed as:

w_{01} - first root of the Bessel's function of the 0 order

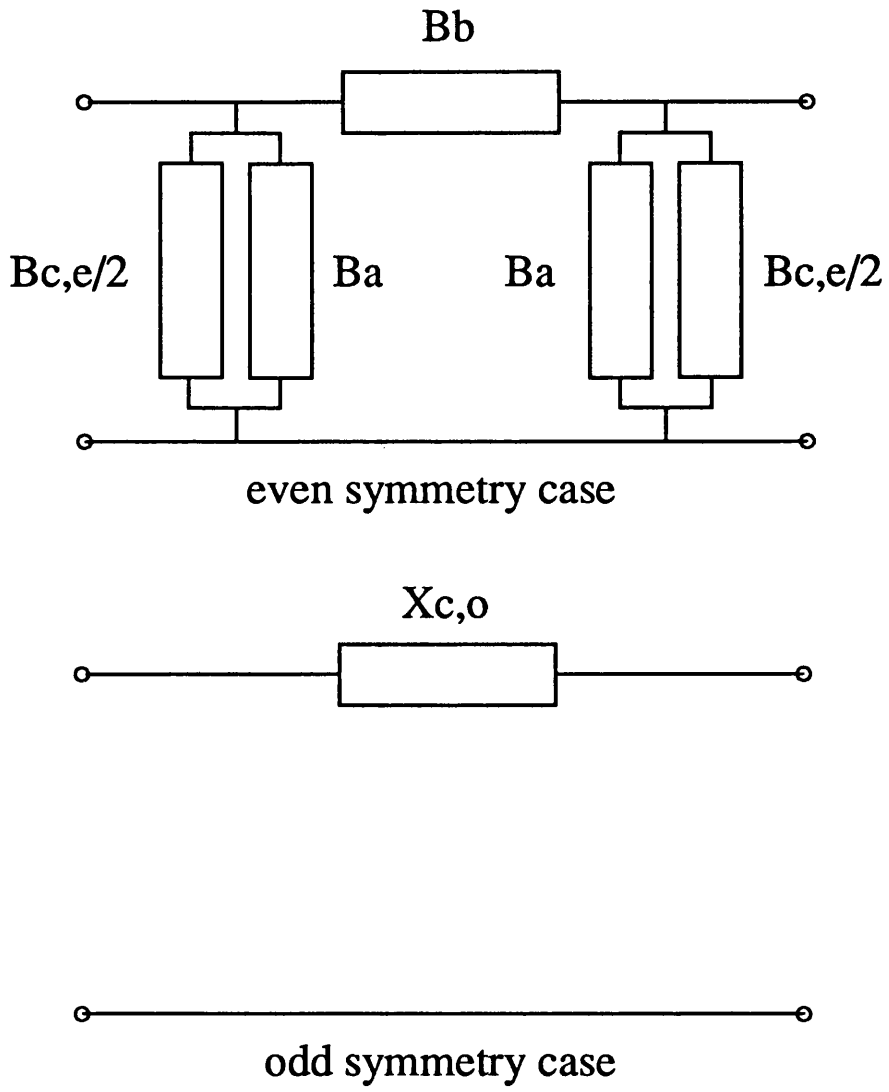

Figure 6.5: Circuits that model an aperture under even and odd excitation symmetry and capable to include correction for wall thickness.

q - phase constant in y direction for grounded dielectric guide of thickness h under LSE polarization

d - hole diameter

s - wall thickness

When the wall thickness is set to zero the correction admittance for odd symmetry excitation tends to infinity, i.e. short circuit connection, while admittance for even symmetry becomes zero, i.e. open connection. Hence there is no influence on coupler response, as expected. When large holes are to be considered, the magnetic and electric polarizability can not be considered as frequently independent any more. Instead, the resonant frequency of the aperture should be taken into consideration, and the polarizabilities get modified forms:

$$\frac{M_x}{1-f^2/f_c^2} = \frac{M_z}{1-f^2/f_c^2} = \frac{2}{\epsilon_r}\frac{P}{1-f^2/f_c^2} \tag{6.14}$$

The f_c represents the cut-off frequency of the circular guide having a diameter d. For the TM_{01} mode this cut-off frequency is given as

$$\begin{aligned} f_{c01} &= \frac{1}{2\pi}\frac{1}{\sqrt{\epsilon\mu}}\frac{w_{01}}{d} \\ &= \frac{1}{2\pi}\frac{1}{\sqrt{\epsilon\mu}}\frac{4.91}{d} \end{aligned} \tag{6.15}$$

This type of correction has been seen to give results in a good agreement with experimentally obtained data for case of the metal waveguide couplers [8].

6.3 Coupling of Multihole Arrays

IDG coupled lines favor forward coupling while making backward coupling weak. The hole arrays in the separation wall should also favor such coupling and balance the frequency dependance of the IDG coupled lines. An n-hole directional coupler is shown in Fig.6.6,

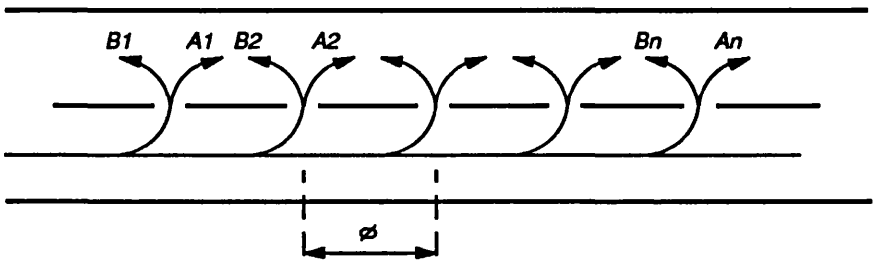

Figure 6.6: Schematic representation of a multi-hole directional coupler.

where the holes are separated by distance d such that

$$d = \frac{\lambda_g}{4} \tag{6.16}$$

at the center frequency.

If the voltage coupling coefficient at hole k is $\mathcal{A}_k$ in forward direction and $\mathcal{B}_k$ in backward direction, then the total unwanted reverse wave coupling becomes

$$\begin{aligned} B_d &= \mathcal{B}_1 + \mathcal{B}_2 e^{-j2\phi} + \mathcal{B}_3 e^{-j4\phi} + \ldots + \mathcal{B}_n e^{-j2(n-1)\phi} \\ &= \sum_{k=1}^{n} \mathcal{B}_k e^{-j2(k-1)\phi} \end{aligned} \tag{6.17}$$

The coupled wave in forward direction is

$$\begin{aligned} A_d &= (\mathcal{A}_1 + \mathcal{A}_2 + \ldots + \mathcal{A}_n)\, e^{-j(n-1)\phi} \\ &= \sum_{k=1}^{n} \mathcal{A}_k e^{j(n-1)\phi} \end{aligned} \tag{6.18}$$

In order to achieve good directivity, some kind of coupling distribution has to be used. Usually a Chebishev's or binomial distribution is adopted as the desired response function for distributed coupling.

For many practical applications very tight couplers are required, and often a single array has

holes of very large diameter, or the array is to long. It is possible to overcome this problem by using superimposed set of arrays. A simple linear relationship determines overall coupling, but this linear relationship breaks down for strong coupling. The fact that overall coupling can never exceed unit value should also be borne in mind during supperpositioning of arrays. Also, it is very interesting that the maximum value of the backward wave of superimposed arrays will never exceed that of a single array, or in other words, the isolation of superimposed arrays is better or equal to that of single array.

6.4 Synthesis and Design Procedure

Two different procedures for multihole IDG coupler synthesis, based on two distinctive analysis approaches, were considered:

- *Discrete* hole coupling and *continuous*, wave coupling are treated independently. Overall coupling is obtained by simple summation of couplings obtained by employing these two coupling mechanisms.
- A continuous coupling and discrete coupling are considered in their interaction. The holes are modeled as an obstacle by use of lumped circuit representation and this model is placed between transmission line sections having the same parameters as the IDG line. Then, by utilizing ordinary circuit analysis of such a combined lumped-distributed network under even and odd mode symmetries, the coupling characteristic is easily obtained.

6.4.1 Coupling mechanisms considered as independent

The theory of coupling through holes were described in the previous section. To find total coupling due to the existence of hole arrays in the mid-wall, the expression (6.18) is used. As the fields of the HE_{01} mode in IDG are very similar to the TE_{01} mode of a closed metal rectangular waveguide, expressions for forward and backward coupling of single hole are valid, subject to the use of the relevant propagation parameters that describe IDG guiding

properties.

The continuous wave coupling is calculated under the assumption that coupler is ideally matched:

$$C_{wave} = \sin^2\left(\frac{\beta_e - \beta_o}{2} \times L\right) \tag{6.19}$$

Then the total coupling is simply found as

$$C_t(fr, a, h, s, d_i, y, n) = C_{hole} + C_{wave} \tag{6.20}$$

where

fr - working frequency

a,h dimensions of IDG cross-section

s - separation between IDGs

d_i - hole diameters

y - height of hole placement

n - number of holes

The initial values for hole diameters are determined from the requirement that the isolation and coupling response of a multi-hole coupler have certain levels and correspond to the Chebyshev equi-ripple function.

6.4.2 Coupling mechanisms considered as interactive

This approach considers that two employed coupling mechanisms to be mutually interacting. The discrete hole coupling is modeled by an equivalent lumped element network as depicted in Fig.6.3. Such lumped networks are then placed between sections of transmission lines having same propagation properties as the IDG. This analysis is performed for odd and even symmetries, and since the hole circuit model is different for these excitations, two distinctive lumped-distributed two-port networks are formed as depicted in Fig.6.7.

The elements of the equivalent circuit are determined by use of (6.10), and the values of these elements are function of hole diameter, height of hole placement, working frequency and the parameters characterizing propagation properties of the coupled IDG section.

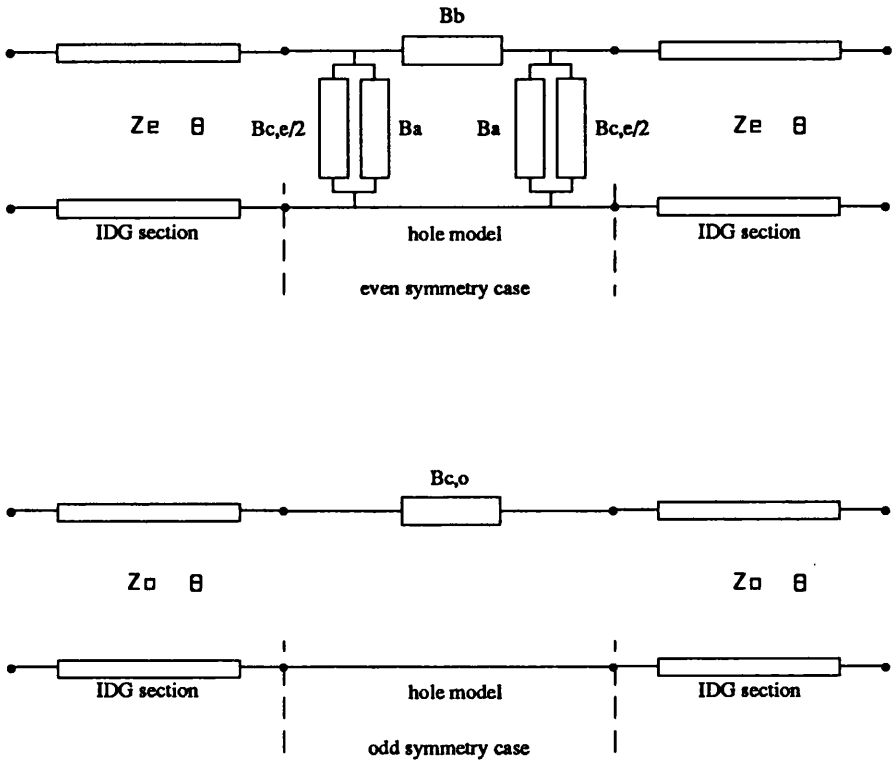

Figure 6.7: The combined lumped-distributed circuit representation for coupled IDG section of 2θ in length additionally coupled by hole drilled in the mid-wall and placed at the middle of a section.

Ordinary network analysis in terms of chain matrix is applied in order to get the overall response of the circuits. By using (A.2) the reflection and transmission coefficients are determined for even and odd mode of operation. Combining these two solutions according to (A.4) the coupler characteristics are easily obtainable. This approach is amenable to strong and weak coupling characterization and takes into account the correction for the finite wall thickness.

6.4.3 Error function formulation

The optimization procedure used to finalise the design requires formulation of an error function, which represents the measure of agreement between calculated and desired response. The error function that leads to maximum obtainable flat coupling of analysed structure is formulated as

$$f_{error} = \sum_{j=1}^{m} \sum_{k=j+1}^{m} |C_t(f_j) - C_t(f_k)|^2 \tag{6.21}$$

where C_t stands for overall coupling at certain point of frequency and m is total number of such points over specified frequency range.

If a certain level of coupling is requested, lets say C_r, then the error function was defined as

$$f_{error} = \sum_{j=1}^{m} |C_t(f_j) - C_r|^2 \tag{6.22}$$

Usually, beside coupling level, coupler parameters such as return loss and reverse coupling are also of interest. Then, for each of these parameters an error function is formulated in either of the ways described above, and the total error function is reached through their combination.

$$f_{error} = W_1 \cdot f_{1error} + W_2 \cdot f_{2error} + \ldots + W_n \cdot f_{nerror} \tag{6.23}$$

The weight coefficients W_i are associated with each error function, and by choosing weights, particular features of the coupler response can be favored during the optimization procedure.

6.5 Initial Hole Diameters Calculation

The coupled wave of a multihole array is determined by (6.18), where the amplitude of the forward coupled wave is calculated as the sum of the wave magnitudes coupled by each hole. There are, of course, an infinite number of ways of arranging the magnitudes of these coupling coefficients, $\mathcal{A}_i$.

The problem of designing a broad band coupler consists of obtaining a desired level of coupling while, also keeping the level of backward coupling under a certain value. When (6.17) is equated to $\varepsilon C_{n-1}(x)$ then this type of solution automatically insures that $|B_d| \leq \varepsilon$ over the specified band. The notification $C_n(x)$ stands for Chebyshev polynomial of order n defined as:

$$C_n(x) = \cos(n \cos^{-1} x) \tag{6.24}$$

The procedure for determining the initial hole diameters is essentially the same as procedure for finding impedance steps in a multi-section transformer design. This procedure involves several steps which are:

- First, the type of distribution is selected. Here, we bound ourself to the use of Chebyshev distribution only.
- Second, the level of discrete coupling is expressed as functions of $\mathcal{A}_1$ only, and after the number of holes n has been chosen, the level of reverse coupling is tested by determining whether or not it exceeds minimal prescribed values ε. If it exceeds, the procedure should be repeated for a larger number of holes.
- Finally, when two previous steps are satisfactorily completed the hole dimensions are obtained interactively from (6.4) or from empirical formulas and graphs [10].

6.6 Examples and Experimental Results

This section is devoted to the example design of two couplers of different coupling levels. The first example addresses the design of a $-3dB$ coupler while second concerns a $-10dB$ coupler design. The synthesis procedure involves the use of an analysis and optimization process. Both types of analysis described earlier, one treating the coupling mechanisms as independent the other treating them as interactive, have been utilized for the purpose of the coupler synthesis. When the error function is formulated according to (6.21) the maximal possible level of flat coupling is achieved for the chosen IDG length, and the coupler cross-section.

Finally, the experimental results gathered from measurements of two realized couplers are compared to the coupler responses obtained through simulation programs.

6.6.1 -3 dB coupler design

It was shown that two IDG placed along side each other form a forward coupler having frequency dependent coupling response but with very good isolation property. Such a longitudinally coupled IDG structure with additional hole arrays drilled in the mid-wall separating the two guides will be used for the $-3dB$ coupler design.

The prerequisite for IDG coupler design is to have values for the propagation constants of even and odd modes that determine the wave coupling characteristic. These parameters can be gathered after applying the analysis developed and described in Chapter 3, and obtained values for two different separation between deep slot IDGs are presented in Tab.6.1.

The example task chosen here is to design a $-3dB$ coupler having flat coupling response over the $8 - 12GHz$ frequency range. The inherent coupling of pure coupled IDG is frequency dependent due to the increased power confinement within the dielectric at higher operating frequency. An additional coupling mechanism is sought in order to balance the intrinsic IDG coupler characteristic, and as previously described, good solution appears to be obtainable using hole arrays.

freq (GHz)	7.0	8.0	9.0	10.0	11.0	12.0
$s = 0.5mm$						
β_{even}	166.647	197.595	228.395	260.395	291.198	322.886
β_{odd}	172.831	204.502	235.714	266.734	297.393	327.930
$s = 1.0mm$						
β_{even}	167.088	198.151	230.240	260.947	292.528	323.704
β_{odd}	172.288	203.633	234.568	265.442	296.330	327.232

Table 6.1: The normal mode phase constants of the coupled IDGs for two different spacing between lines. The IDG is filled with PTFE and have $10.16 \times 15.24mm$ for slot dimensions.

As the measured reverse coupling of pure coupled IDG lines are of the order of $-20dB$, five holes in a single array appears to be sufficient to keep the total reverse coupling of the same order at least. Then expressions for the forward and backward coupled waves become

$$\begin{aligned} A_d &= 2\mathcal{A}_1 + 2\mathcal{A}_2 + \mathcal{A}_3 \\ B_d &= 2\mathcal{B}_1 \cos(4\phi) + 2\mathcal{B}_2 \cos(2\phi) + \mathcal{B}_3 \end{aligned} \tag{6.25}$$

In order to keep the hole diameters small and realizable, the level for wave coupling of a single array is chosen to be $-28dB$. A this level of coupling is also of the same order as wave coupling of an IDG section having length equal to that of the single array. This is very important in the sense that an easy balance between the two mechanisms can be obtained only if they have a similar level of coupling. Then we can write

$$A_d = \frac{1}{antilog 20/28} = 0.04 \tag{6.26}$$

We adopt that bandwidth ratio $p = 2.0$ and substitute $\cos\phi = x\cos\phi_1$ with $\phi_1 = 180^o/(p+1) = 60^o$, so that $\cos\phi = 0.5$. Also, if we assume for the moment that the magnitudes of the forward and backward waves coupled through a single hole are the same, $\mathcal{A}_i = \mathcal{B}_i = \Gamma_i$, then

$$\begin{aligned} B_d &= 2\Gamma_1(8x^4\cos\phi_1 - 8x^2\cos^2\phi_1 + 1) + 2\Gamma_2(2x^2\cos^2\phi_1 - 1) + \Gamma_3 \\ &= \varepsilon C_4(x) = (8x^4 - 8x2 + 1)\varepsilon \end{aligned} \tag{6.27}$$

A_1	0.0032	d_1	2.43275
A_2	0.0098	d_2	3.50864
A_3	0.0135	d_3	3.90157

Table 6.2: The magnitudes of the forward coupled wave and corresponding diameter values for the case when five hole array is used to achieve power coupling of -14dB. Guide dimensions are 10.16 × 15.24mm, dielectric inset is made from PTFE and guides are detached by $s = 0.47mm$.

From the above equality we find

$$\begin{aligned} \Gamma_1 &= 8\varepsilon \\ \Gamma_2 &= 24\varepsilon \\ \Gamma_3 &= 33\varepsilon \end{aligned}$$

and forward coupling is then

$$A_d = 2\Gamma_1 + 2\Gamma_2 + \Gamma_3 = 97\varepsilon$$

giving

$$\varepsilon = \frac{0.04}{97}$$

Directivity is obtained as

$$D = 20log\frac{A_d}{B_d} = 39dB$$

If better directivity required additional holes in the array should be introduced. The coupling coefficients and corresponding diameters of holes are represented in tabular form Tab.6.2 In order to achieve coupling level of $-3dB$, ten superimposed arrays are combined as shown in Fig.6.8. The full length of such a superimposed array is $L = 240mm$ and the response of discrete hole and continuous wave coupling over the considered frequency range is depicted in Fig.6.9. The opposite frequency dependence of the two employed coupling mechanisms and their tendency to balance each other is clearly apparent.

Now we come to the point, from where the synthesis can be taken along two different paths. The difference occurs in the way in which the total coupling is calculated. The first path as-

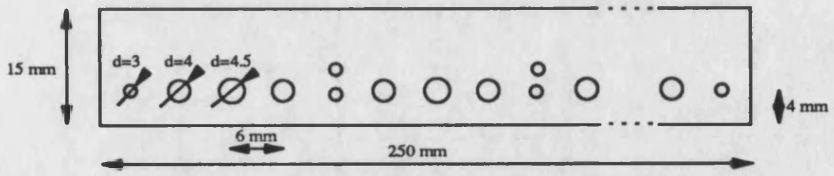

Figure 6.8: Superimposed hole arrays

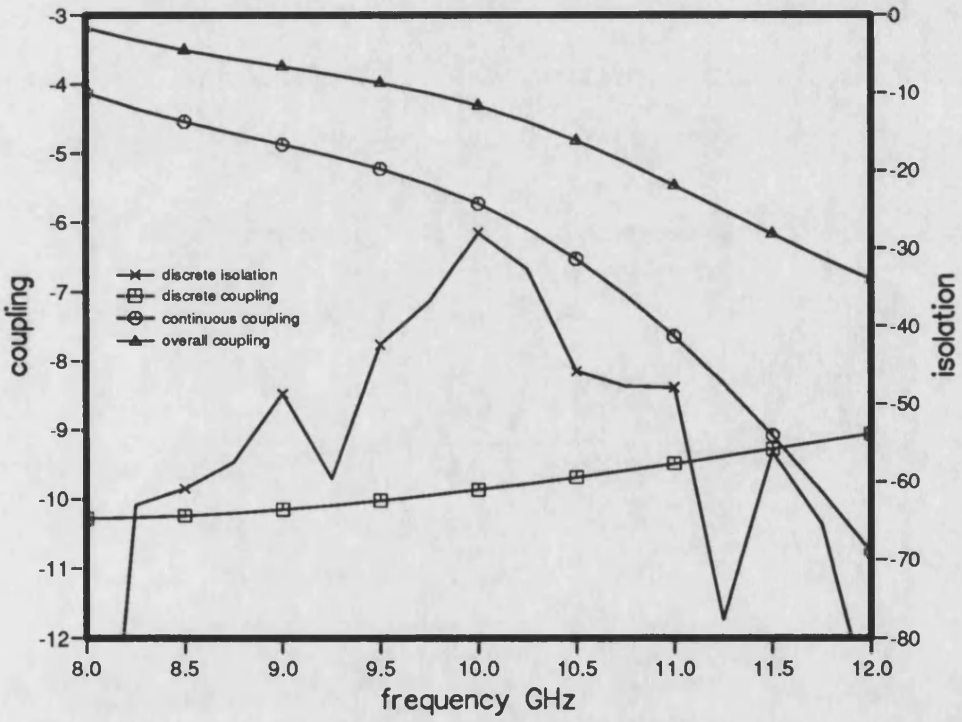

Figure 6.9: Response of multi-hole IDG coupler before optimization. Overall coupling is obtained as sum of discrete and continuous couplings which are regarded as independent. Guide dimensions are $10.16 \times 15.24mm$ and are separated by $s = 0.47mm$. Teen superimposed hole arrays were used each array comprises five holes with diameters listed in Tab.6.2 . The all holes are placed at height of 4mm from slot floor.

	Method I	Method II
d_1	1.76690	2.31713
d_2	3.93511	4.41310
d_3	5.03693	3.00810
y_1	7.68143	6.67634
y_2	7.60907	3.88266
y_3	7.64104	2.70211

Table 6.3: The optimal values for hole diameters and heights of their placement. The considered guides are of deep slot configuration having 10.16×15.24mm for slot dimensions and filled with PTFE. Guides are separated by s=0.47mm.

sumes that two mechanisms are independent, and overall coupling is simple sum of couplings obtained by each simple mechanism. This method from now on will be denoted as Method I. Method II is that where the coupling mechanisms are treated as interacting, and elements of circuit analysis, as described in section 6.4, is employed in order to find the overall coupling characteristics.

After applying an optimization process in order to minimize the error function, the optimal coupling characteristic is presented in Fig.6.10. The analysis used to supply feed-back information to the optimization routine is performed in the manner described for Method I.

On the other hand, when the same definition of error function is used, but coupler responses are supplied by Method II, the optimal response is shown in Fig.6.11. The optimal hole diameters for both procedures are represented in tabular form, Tab.6.3.

6.6.2 -10dB coupler design

The design of a $-10dB$ coupler utilizes the same procedure as described in the last section. Again, we use a five hole array, but as the required overall coupling level is much lower this time, only three or four superimposed arrays are needed. It also means that length of the coupled IDG section involved in coupler design is considerably shorter than that length used in the $-3dB$ case.

Following same steps as in the last design example, but now using a wider separation between

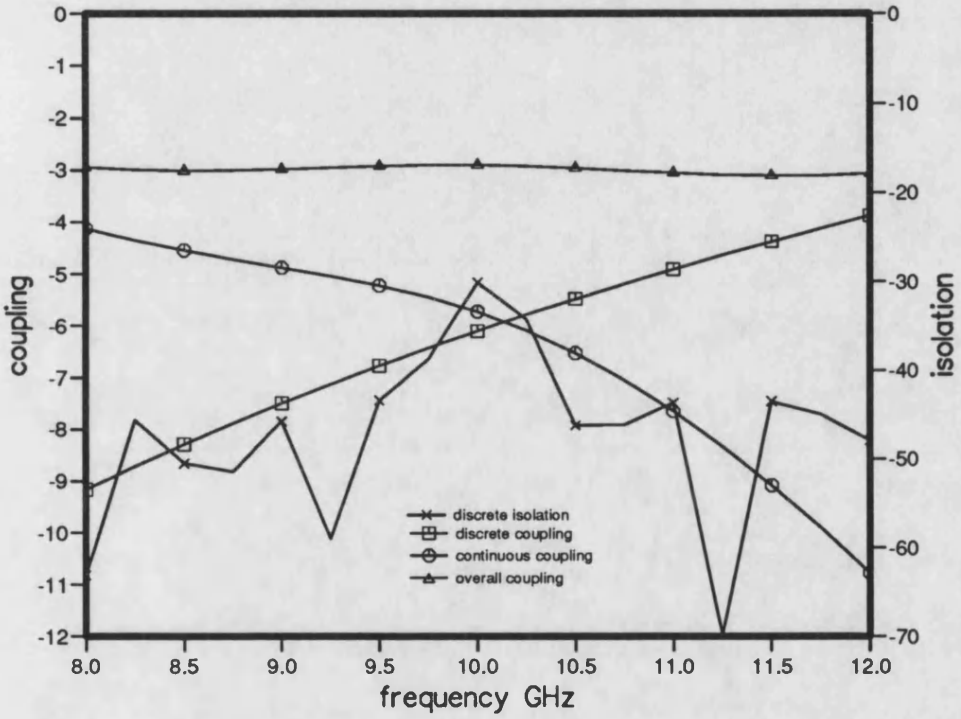

Figure 6.10: The response of multihole IDG coupler optimized to the coupling level 0f -3dB. The goal is achieved by using analysis Method I to supply necessary feed-back information for optimization routine. The hole diameters and heights of their placement are given in Tab.6.3 . The used IDG section is L=240mm in length and has 10.16×15.24mm for dimensions of guide cross-section. The guides are separated by s=0.47mm.

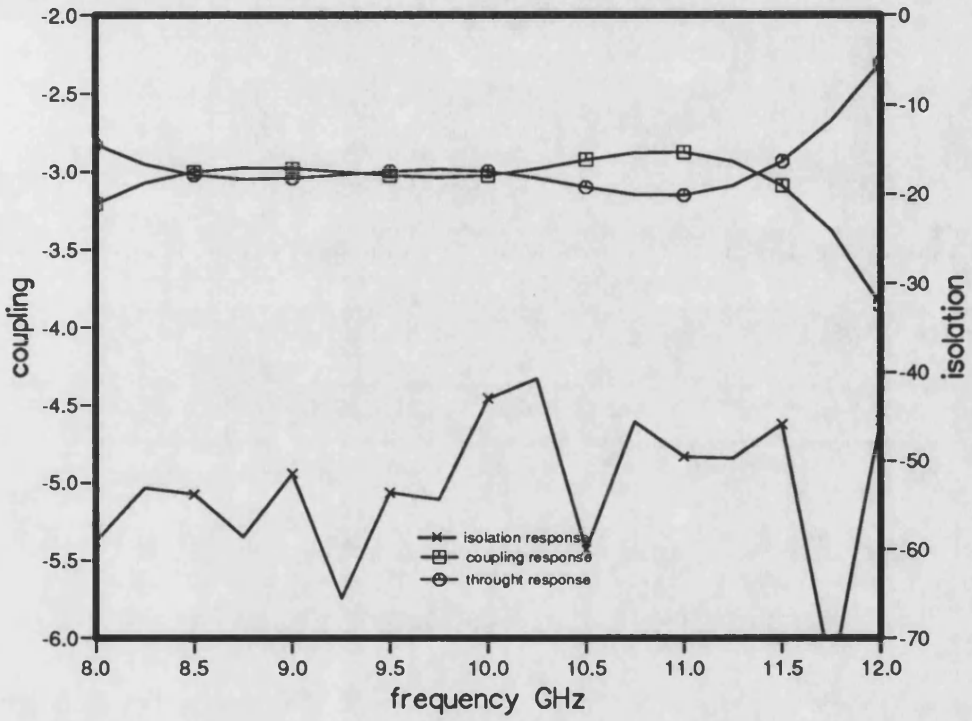

Figure 6.11: The response of multihole IDG coupler optimized to the coupling level 0f -3dB. The used analysis Method II consider the coupling mechanisms in their interaction. The hole diameters and heights of their placement are given in Tab.6.3 . The used IDG section is L=240mm in length and has 10.16×15.24mm for dimensions of guide cross-section. The guides are separated by s=0.47mm and dielectric inset is made from PTFE.

$\mathcal{A}_1$	0.0046	d_1	2.72959
$\mathcal{A}_2$	0.0139	d_2	3.93675
$\mathcal{A}_3$	0.0191	d_3	4.37763

Table 6.4: The magnitudes of forward coupled waves and initial hole diameters that achieve -15dB coupling level per single array. Holes are assumed to be placed at 4mm height from slot floor. The considered guide has deep slot configuration with 10.16×15.24mm for cross-section dimensions and slot is filled with PTFE dielectric material. The separation between guides is s=1.0mm.

	Method I	Method II
d_1	5.31984	4.84944
d_2	4.43402	4.63282
d_3	5.27188	5.46638
y_1	3.63544	5.28320
y_2	5.20572	7.83996
y_3	4.07262	4.05697

Table 6.5: The optimal values for hole diameters and their placement heights obtained by two different analysis approaches. Method I considers the used coupling mechanisms as independent while Method II takes into account interactive nature of coupling mechanisms. The involved IDG section, L=96mm long, comprises two symmetric IDGs detached by s=1.0mm and having 10.16×15.24mm for the cross-section. Dielectric filling is assumed to be made from PTFE.

the two IDGs, the magnitudes of forward coupled waves and corresponding diameters are calculated and given in Tab.6.4.

The responses of discrete hole coupling and continuous wave coupling before optimization are shown in Fig. 6.12. The overall coupling response after applying two types of synthesis procedures are depicted in Fig. 6.13 and Fig. 6.14. The overall coupling in Fig. 6.13 is obtained through optimization procedure which utilize analysis Method I in order to evaluate the error function required by the optimization procedures.

On other hand, when Method II of analysis is used to provide necessary inputs for calculation of the error function, the overall coupling is depicted in Fig.6.14.

The optimal values for hole diameters and height of hole placements, gained through both types of approaches are given in tabular form in Tab. 6.5.

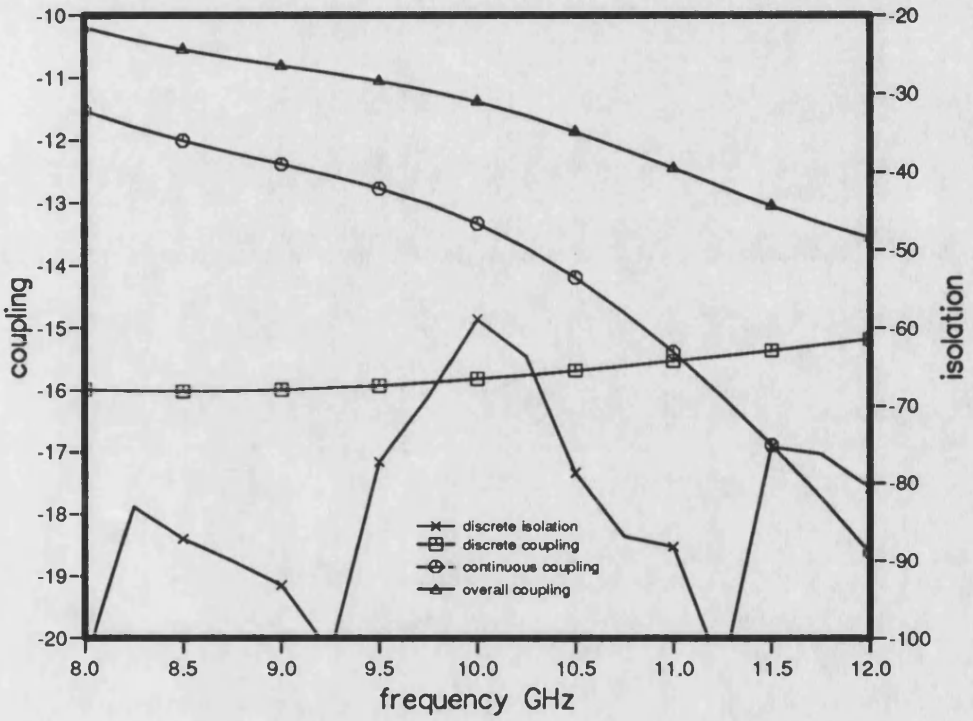

Figure 6.12: The responses of multi-hole IDG coupler initially calculated to have coupling level of -10dB. The hole diameters are listed in Tab. 6.4 . All holes are placed on same height of 4mm. The involved IDG section, L=96mm long, comprises two symmetric IDGs detached by s=1.0mm and having 10.16×15.24mm for the cross-section. Dielectric filling is assumed to be made from PTFE.

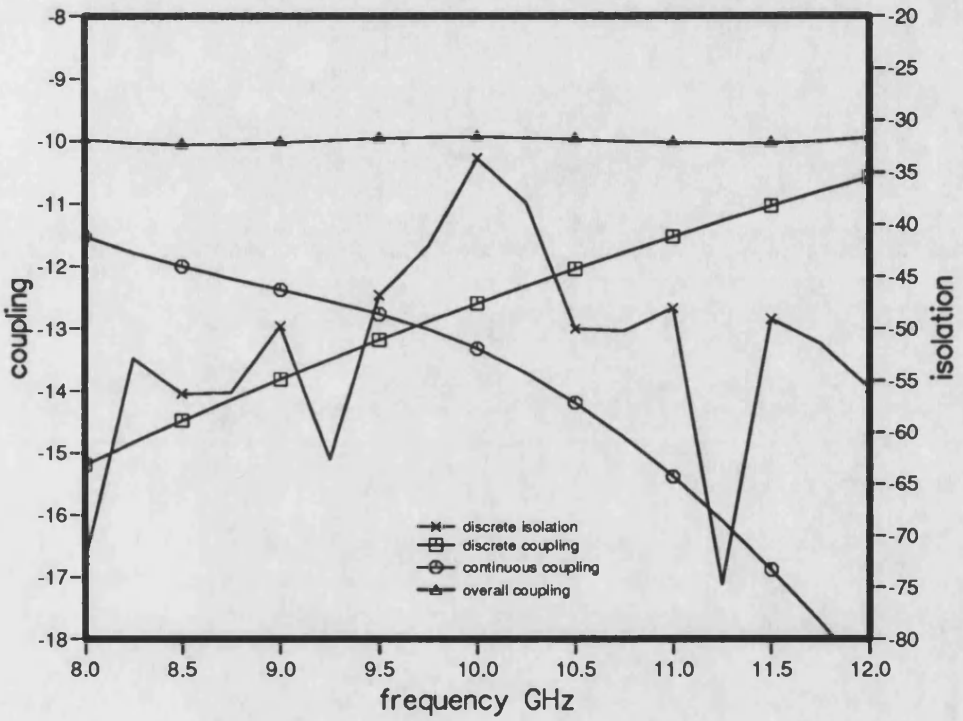

Figure 6.13: The optimal response for -10dB coupler when coupling mechanisms are treated as independent. The optimal values for hole diameters and their placement heights are given in Tab. 6.5 . The involved IDG section, L=96mm long, comprises two symmetric IDGs detached by s=1.0mm and having 10.16×15.24mm for the cross-section. Dielectric filling is assumed to be made from PTFE.

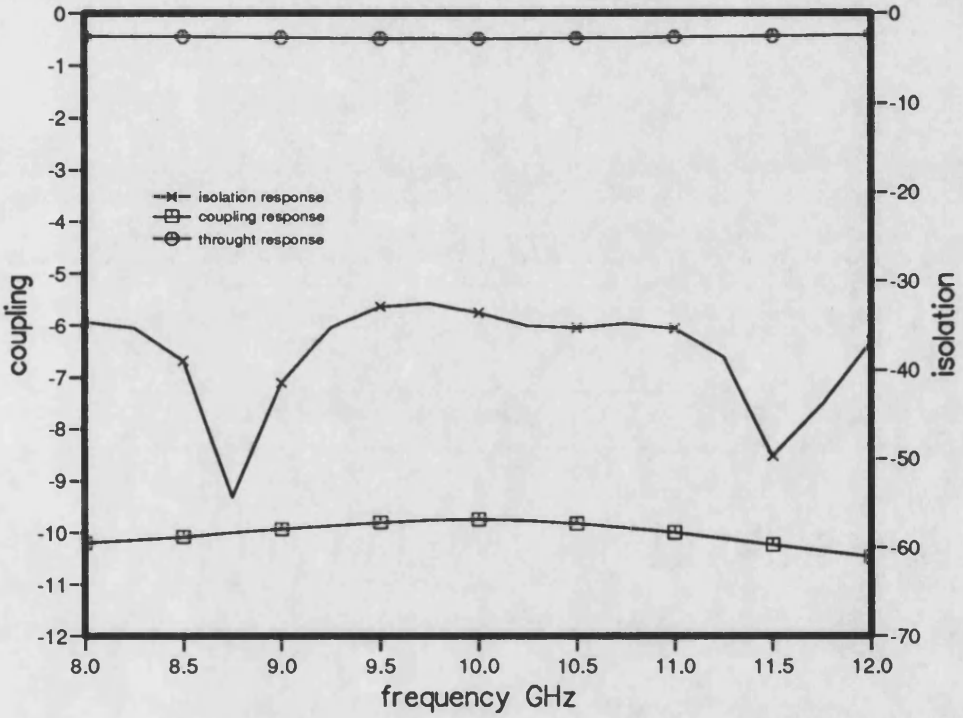

Figure 6.14: The optimal response for -10dB coupler when coupling mechanisms are treated as interactive. The optimal values for hole diameters and their placement heights are given in Tab. 6.5 . The involved IDG section, L=96mm long, comprises two symmetric IDGs detached by s=1.0mm and having 10.16×15.24mm for the cross-section. Dielectric filling is assumed to be made from PTFE.

6.6.3 Coupler with maximal obtainable flat coupling

We have defined an error function (6.21) whose minimization leads to hole diameters solutions which give maximal obtainable flat coupling for certain length of IDG section over a prescribed frequency range. This kind of information can be used for the purpose of IDG length and guide spacing assessment when certain level of coupling is required. The curves representing maximally obtainable coupling for two different spacings and for several coupling lengths are plotted and shown in Fig. 6.15 and Fig. 6.16. Only Method II, capable of taking into account interactive behavior of wave and hole coupling, was used in this analysis. Optimal values for hole diameters and heights of holes placement are presented in Tab.6.6.

In order to illustrate influence of wall thickness on the coupler response, two curve sets with and without correction for wall thickness are plotted in Fig.6.17 for three different spacings between the guides.

6.6.4 Experimental results

For the reason of practical realization restrictions imposed on us by the availability of material and tools, optimal values for hole diameters and heights of hole placement are not practically implemented. Instead, both realized couplers use deep slot IDG structure and PTFE as filing material, and the holes were uniformly placed at a height of 4.0mm. The $-3dB$ coupler uses guides with 0.47mm separation, while 1.0mm separation was used for the $-10dB$ coupler. As expected, more dramatic worsening in coupler responses comes with thicker separation wall. The comparison between coupling response obtained through analysis procedures and experiments are depicted in Fig. 6.18 for the $-3dB$ coupler and in Fig. 6.19 for the $-10dB$ coupler.

From both figures it is obvious that the analysis method where the coupling mechanisms are treated as interacting better fit the measured coupler response. Also, we noticed that the approach where coupling is calculated simply as sum of couplings of two independent mechanisms becomes less accurate for higher coupling levels. Hence we conclude that linear superposition of coupled power is more inaccurate at higher levels of coupling.

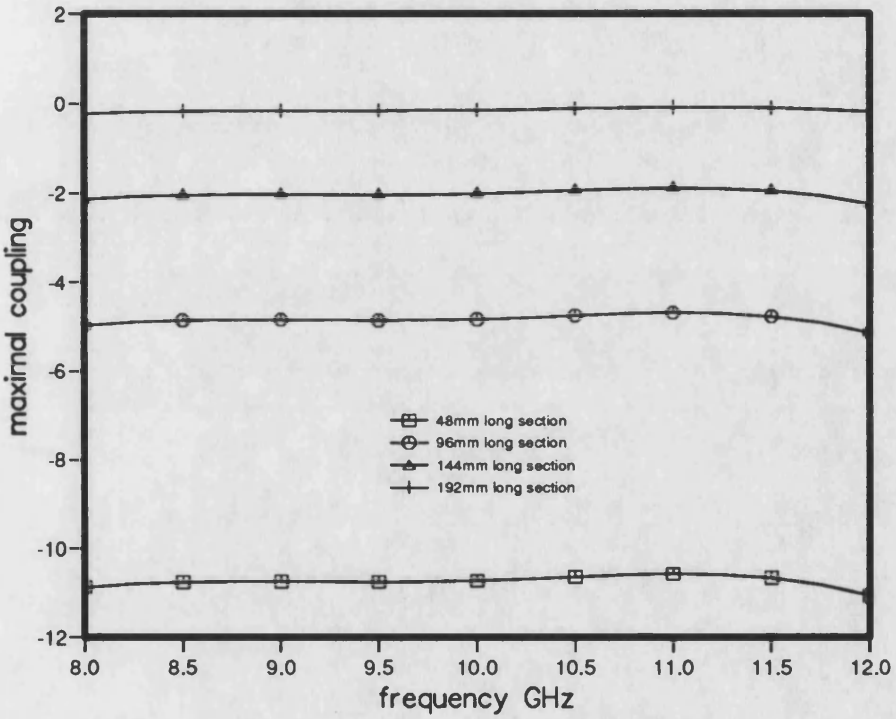

Figure 6.15: The maximal obtainable flat coupling for various lengths of IDG coupled section. The involved IDG sections, comprises two symmetric IDGs detached by s=0.47mm and having 10.16×15.24mm for the cross-section. Dielectric filling is assumed to be made from PTFE.

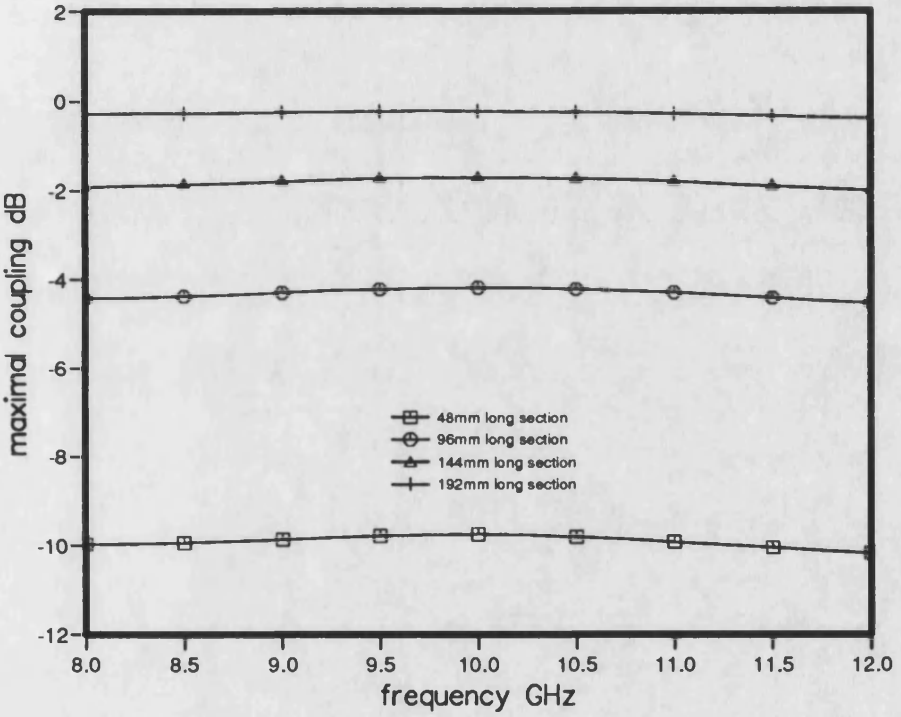

Figure 6.16: The maximal obtainable flat coupling for various lengths of IDG coupled section. The involved IDG sections, comprises two symmetric IDGs detached by s=1.0mm and having 10.16×15.24mm for the cross-section. Dielectric filling is assumed to be made from PTFE.

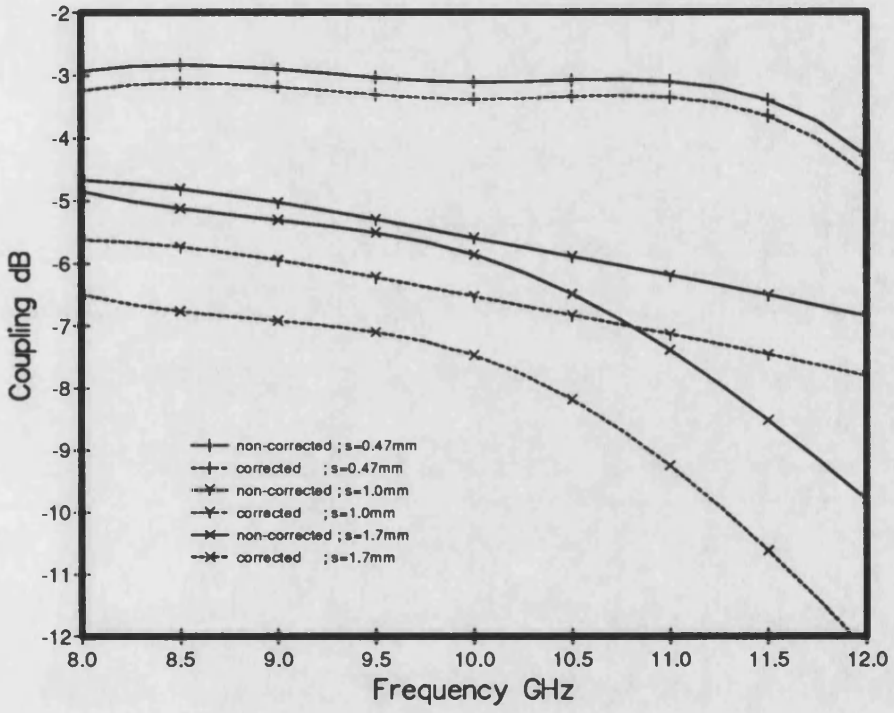

Figure 6.17: The two curve sets for the coupling characteristic of multi-hole IDG coupler. The sets are plotted for three different separation between guides. First curve in each set is calculated when no correction for wall-thickness is taken into account, second is the corrected coupling response. The involved IDG section, L=240mm long, comprises two symmetric IDGs detached by s=1.0mm and having 10.16×15.24mm for the cross-section. Dielectric filling is assumed to be made from PTFE. Teen superimposed arrays are employed, each consists from five holes whose diameters are listed as: $d_1 = 1.0mm$, $d_2 = 3.0mm$ and $d_3 = 4.0mm$. All holes placed at height of 4.0mm from the groove floor.

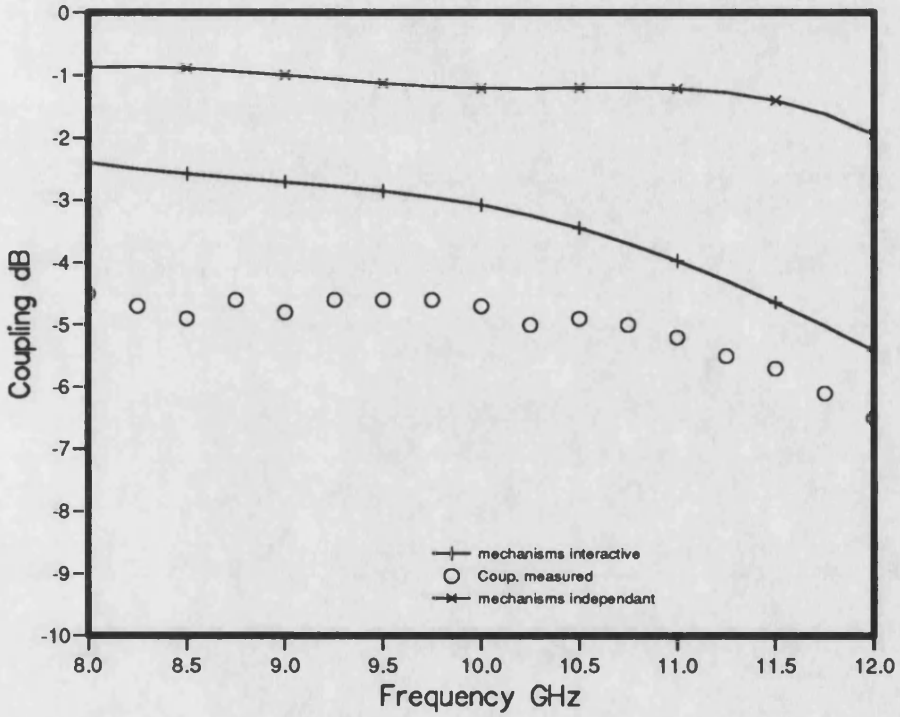

Figure 6.18: The comparison between measured and predicated level of coupling for -3dB coupler. The involved IDG section, L=240mm long, comprises two symmetric IDGs detached by s=0.47mm and having 10.16×15.24mm for the cross-section. Dielectric filling is assumed to be made from PTFE. Teen superimposed arrays are employed, each consists from five holes whose diameters are listed as: $d_1 = 3.0mm$, $d_2 = 4.0mm$ and $d_3 = 4.5mm$. All holes placed at height of 4.0mm from the groove floor.

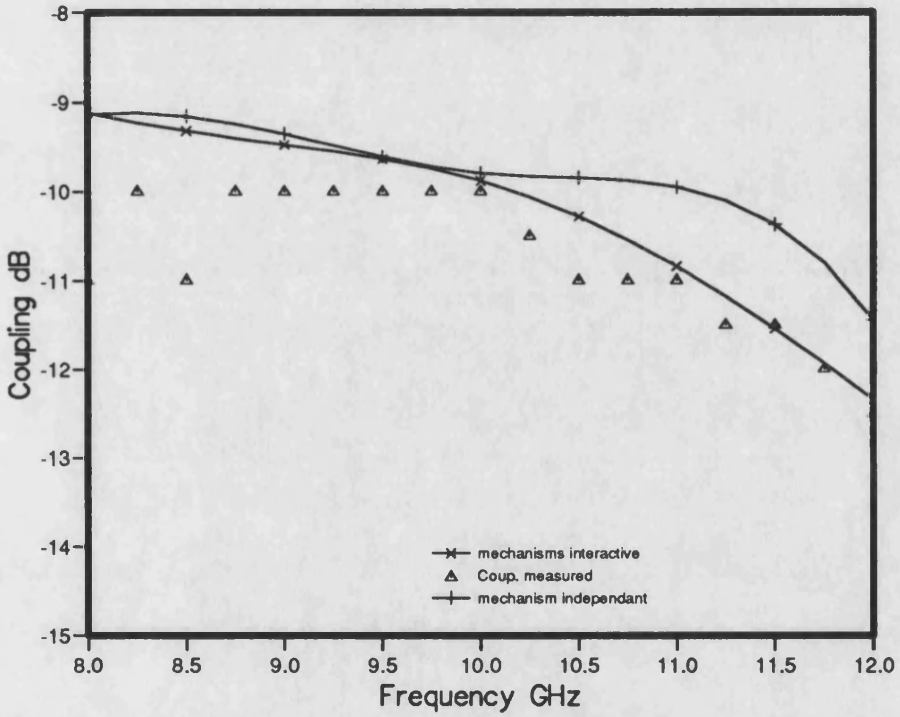

Figure 6.19: The comparison between measured and predicated level of coupling for -10dB coupler. The involved IDG section, L=96mm long, comprises two symmetric IDGs detached by s=0.47mm and having 10.16×15.24mm for the cross-section. Dielectric filling is assumed to be made from PTFE. Teen superimposed arrays are employed, each consists from five holes whose diameters are listed as: $d_1 = 1.0mm$, $d_2 = 3.0mm$ and $d_3 = 4.0mm$. All holes placed at height of 4.0mm from the groove floor.

The measured responses for coupled and through ports of $-3dB$ coupler are shown in Fig.6.20 while return loss and isolation characteristics of the same coupler are represented in Fig.6.21. The coupling and isolation characteristics of $-10dB$ coupler are depicted in Fig.6.22.
From the measurements it is apparent that coupling response shows flat characteristic over vide frequency range. The power levels on output of the coupled and through ports are not of predicated value. The power loss which occurs is believed to be mainly due to radiation loss from the transition apertures.
The measured return loss characteristic is very similar to that of a single line and level of the returned power is about $-20dB$. The value of the return loss is directly determined by the ability of transition section to effectively matches metal guide to the IDG.
In a symmetric coupler case, which were only considered here, the imperfect matching implies imperfect isolation, and vice versa. Because that, the measured isolation of realized couplers has the similar power level as the return-loss characteristic. In order to measure the predicated isolation level of $-40dB$, the much better matching of coupler ports was needed. Moreover, a separator between two coupled IDGs is relatively thin and consequently transition apertures lie very close each other, giving direct path to mask coupled line isolation. The finite reflection from a taper and backward coupling action also mask isolation, Fig. 6.23, and gives wavy pattern to the measured isolation curve.

6.7 Conclusion

In this chapter a procedure for IDG multi-hole coupler design is presented. It was shown that by utilizing additional coupling through holes drilled in the mid-wall of IDG coupled section, a broad-band flat coupling characteristic can be achieved.
Two types of analysis were performed

- first, coupling over air region and through holes were treated independently
- second, two mechanisms were understood to be in interaction

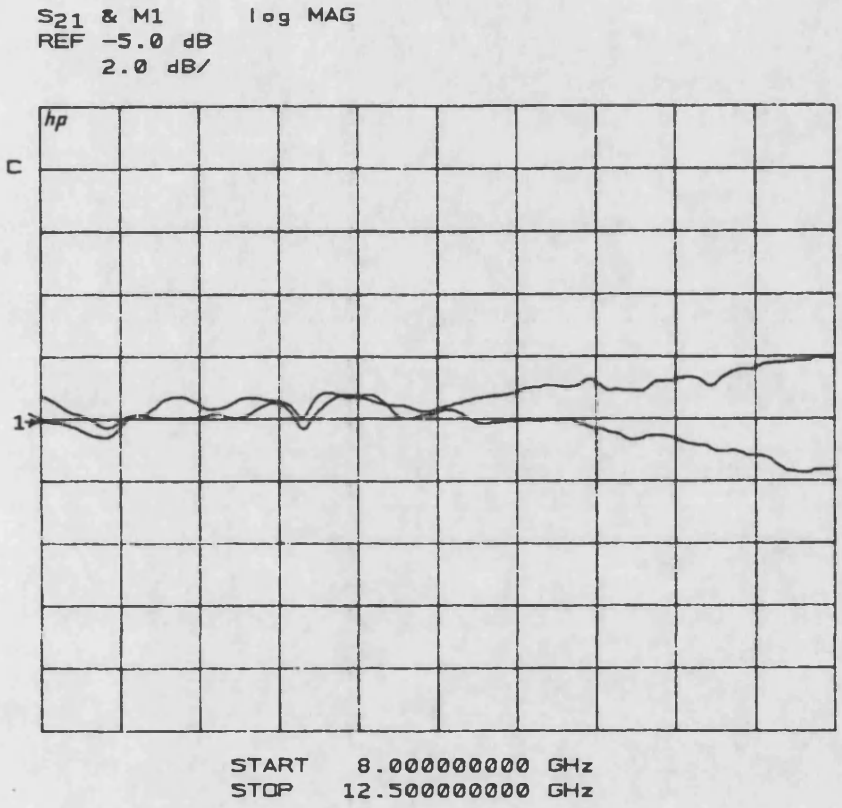

Figure 6.20: The responses of the coupled and through ports of -3dB coupler. The involved IDG section, L=240mm long, comprises two symmetric IDGs detached by s=0.47mm and having 10.16×15.24mm for the cross-section dimensions. Dielectric filling is assumed to be made from PTFE. Teen superimposed arrays are employed, each consists from five holes whose diameters are listed as: $d_1 = 3.0mm$, $d_2 = 4.0mm$ and $d_3 = 4.5mm$. All holes placed at height of 4.0mm from the groove floor.

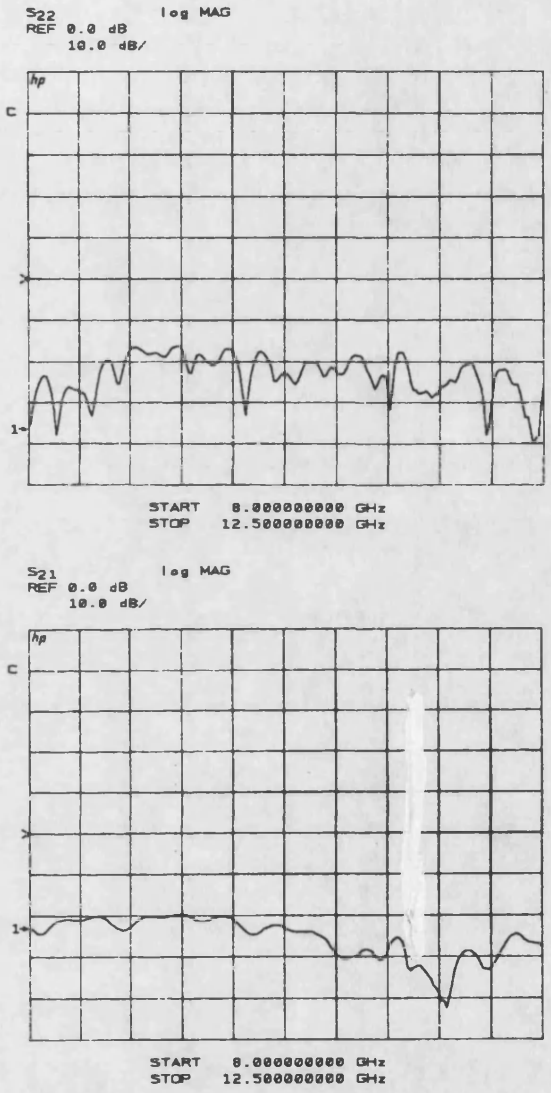

Figure 6.21: Isolation and return loss characteristics of -3dB coupler. The involved IDG section, L=240mm long, comprises two symmetric IDGs detached by s=0.47mm and having 10.16×15.24mm for the cross-section dimensions. Dielectric filling is assumed to be made from PTFE. Teen superimposed arrays are employed, each consists from five holes whose diameters are listed as: $d_1 = 3.0mm$, $d_2 = 4.0mm$ and $d_3 = 4.5mm$. All holes placed at height of 4.0mm from the groove floor.

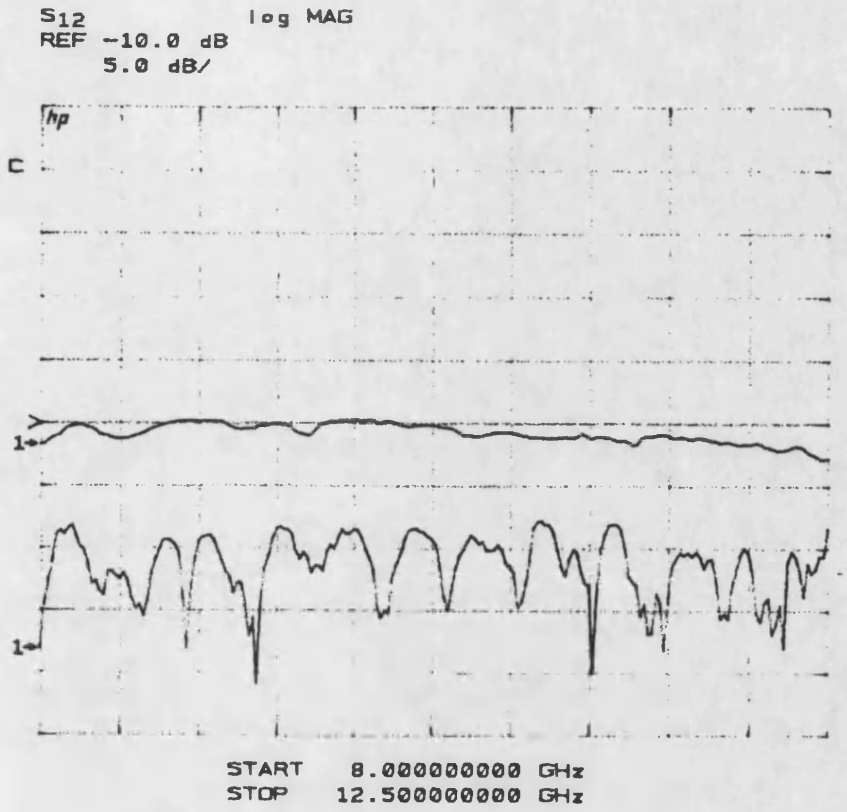

Figure 6.22: The measured coupling and isolation characteristic for -10dB coupler. The involved IDG section, L=96mm long, comprises two symmetric IDGs detached by s=0.47mm and having 10.16×15.24mm for the cross-section. Dielectric filling is assumed to be made from PTFE. Teen superimposed arrays are employed, each consists from five holes whose diameters are listed as: $d_1 = 1.0mm$, $d_2 = 3.0mm$ and $d_3 = 4.0mm$. All holes placed at height of 4.0mm from the groove floor.

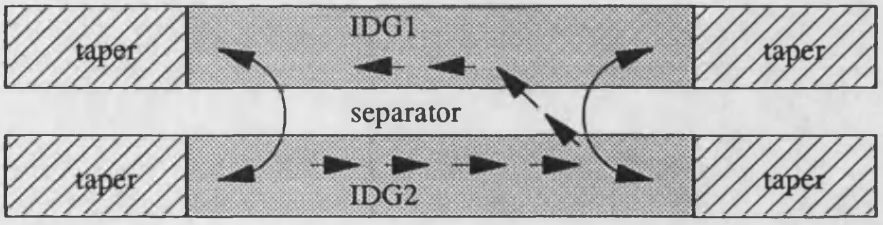

Figure 6.23: The direct transition aperture coupling and backward coupling of reflected wave act to mask isolation of IDG coupler.

Also, the finite thickness of separation wall between guides was modeled by reactive elements incorporated into a lumped circuit model of an obstacle. This approach represents a novel technique of modeling the influence of finite wall thickness on coupler responses. Synthesis procedures are based on two analysis methods developed and utilize an optimization procedure in order to find optimal parameters for multi-hole IDG coupler design. The Chebyshev equi-ripple function is used to model the pass-band forward coupling response, and from such a model initial values for hole diameters are determined.

Generally speaking, better agreement between measured and predicated data is achieved by using analysis method where continuous wave and discrete hole coupling were understood to be interacting, but the simple approach of treating the coupling mechanisms as independent gives quite satisfactory results for low levels of coupling and can be used for the sake of simplicity.

Very good IDG coupler characteristics are measured for the two test pieces, the $-3dB$ and $-10dB$ couplers. The measurements of coupler characteristics were affected by the lack of good metal guide to IDG transition.

l	d_1	d_2	d_3	y_1	y_2	y_3
$s = 0.5mm$						
48.00	4.61446	4.67998	2.50017	7.62317	7.62317	7.60744
96.00	3.04706	4.81487	5.49990	7.61336	7.61990	7.62045
144.00	3.97375	4.83215	4.58179	7.56949	7.59387	7.58770
192.00	3.93345	5.29104	5.37419	7.78076	7.77294	7.70905
$s = 1.0mm$						
48.00	5.04009	5.49406	5.14020	7.27110	6.65462	5.95434
96.00	5.15455	5.45012	5.49763	5.57602	7.90615	7.83968
144.00	5.05164	5.39529	5.49988	6.69046	7.34388	5.10130
192.00	4.85658	5.49944	5.29823	7.40534	7.45968	6.01353
240.00	4.86660	5.49999	5.05323	6.65151	6.96570	6.09249

Table 6.6: Optimal values for hole diameters and and heights of their placement giving maximally obtainable level of flat coupling for different lengths of coupled section. The IDG is filled with PTFE and have $10.16 \times 15.24mm$ for slot dimensions.

References

[1] H. A. Bethe

Theory of diffraction by small holes

1944 Phys. Rev. vol.66 pp.163-182

[2] T. Rozzi and S. J. Hedges

Rigorous Analysis and Network Modeling of the Inset Dielectric Guide

IEEE Trans. Microwave Theory and Tech. vol.MTT-35 Sep.1987,pp.823-833

[3] S. R. Pennock, D. Boscovic and T. Rozzi

Broadband Inset Dielectric Guide Coupler

21st EuMWC Stutgart, September 1991, paper C8.3

[4] H. J. Riblet and T. S. Saad

A new type of waveguide directional coupler

Proc. IRE 36, 1948 pp.61-64

[5] N. Markuwitz

waveguide Handbook

McGraw-Hill, New York, 1951 ch.3

[6] A. Oliner

Equivalent circuits for small symmetrical longitudinal apertures and obstacles

I. R. E. Trans.,MTT-8,1960, p.72-77

[7] T. Rozzi

Topics in the synthesis of microwave directional couplers and low-pass filters

PhD thesis, University of Leeds, May 1968

[8] S. B. Cohn

Microwave coupling by large apertures

Proc. IRE 40, 1952 pp.697-699

[9] T. Rozzi and M. Mongiardo

E-Plane Steps in Rectangular Waveguide

IEEE Trans. Microwave Theory and Tech. vol.MTT-39 Aug.1991, pp.1279-1288

[10] E. S. Hensperger *The design of multi-hole coupling arrays* The Microwave Journal, Vol.2, No.8, pp. 38-42, August 1959